METAMAGNETISM IN LOW DIMENSIONS

Dissertation for the Degree of Ph. D.
MICHIGAN STATE UNIVERSITY
PAUL R. NEWMAN
1975

This is to certify that the

thesis entitled

METAMAGNETISM IN
LOW DIMENSIONS

presented by

Paul R. Newman

has been accepted towards fulfillment
of the requirements for

Ph.D. degree in Physics

J A Cowen

Major professor

Date July 25, 1975

O-7639

ABSTRACT

METAMAGNETISM IN LOW DIMENSIONS

By

Paul R. Newman

Magnetic systems in real crystals exhibit low dimensional behavior over a limited temperature range. At sufficiently low temperatures a weaker interaction causes the system to order in three dimensions. The low dimensional character often manifests itself in the nature of a field induced magnetic phase transition.

Magnetic phase transitions in applied field are analyzed by treating specific orientations of sublattices as linear combinations of classical spin polarization vectors. The stationary energy configurations are found by differentiating the energy of a zero temperature Hamiltonian. The behavior of these stationary states in applied field, as shown in "Polarization Energy Diagrams", determines the nature of the magnetic phase transition. A special class of transitions is defined as "metamagnetic." The conditions which produce a metamagnetic transition are discussed. Anisotropy is shown to play a crucial role in such transitions.

Paul R. Newman

Two experimental investigations of low dimensional systems are presented. In the first instance measurements of: crystal lattice parameters, the space group, the susceptibility as a function of applied field, the bulk magnetization in applied field as a function of temperature, NMR, and ESR are reported for manganese bromide trimethyl amine dihydrate. Although the unit cell is monoclinic with the space group $P2_1/m$, the exact crystal structure is at present unknown. A partial crystal structure for manganese bromide trimethyl amine dihydrate is derived from the experimental evidence and shown to be related to a similar compound: cobalt chloride trimethyl amine. The magnetically ordered state (T_N=1.58K) is characterized as a four sublattice canted antiferromagnet with the magnetic space group $P_{2s}2_1/m$. A magnetic phase transition which is observed below T_N with the external field along the b axis is asserted to be metamagnetic.

The second experimental investigation was concerned with the copper complex of the amino acid L-Isoleucine. Magnetic susceptibility in zero and applied field as well as ESR are reported. The orientation of the principal axes of the derived g-tensors are discussed in terms of the 4mm symmetry of the five fold local coordination of the $3d^9$ copper ion. The magnetic susceptibility

indicates a transition to a three dimensionally ordered state at 0.117K. In the temperature region from 4.2K to 0.5K the magnetic behavior is best described as due to a two dimensional Heisenberg ferromagnetic interaction with $J_F/k=0.12K$.

METAMAGNETISM IN LOW DIMENSIONS

By

Paul R. Newman

A DISSERTATION

Submitted to
Michigan State University
in partial fulfillment of the requirements
for the degree of

DOCTOR OF PHILOSOPHY

Department of Physics

1975

DEDICATION

To my wife Shari and my daughter Allison who suffered my long days and longer nights.

To the Greek shepherd Magnes, who started it all.

ACKNOWLEDGMENTS

I would like to express my deepest gratitude to my mentor, Dr. J. A. Cowen for his patience and guidance during my doctoral studies. My special thanks is also extended to Dr. R. D. Spence for his aid in the collection of experimental data and his guidance and understanding. I am indebted to my cohorts Dr. C. S. Stirrat and Dr. J. L. Imes for their assistance in gathering data and a willingness to listen. I would like to thank Dr. W. Pratt, Jr., for the use of his He^3-He^4 dilution refrigerator. I would like to acknowledge many fruitful discussions with Dr. T. A. Kaplan and Dr. S. D. Mahanti. Finally, I wish to thank the entire staff of the Physics department including the machine and electronic shops, the secretaries, and the administration for making life bearable.

TABLE OF CONTENTS

LIST OF TABLES

LIST OF FIGURES

INTRODUCTION

Magnetism which results from exchange or super-exchange is in general a very complex three-dimensional many-body problem. However, in some magnetic insulators, the crystal contains low dimensional structures which may be described as "sheets" or chains." These structures, which arise from the physical arrangement of chemical bonds between atoms, frequently result in electron interactions which reflect the low dimensional nature of the bonds.

Experimentally, one often finds that at sufficiently low temperatures, the low dimensional magnetic systems undergo a transition to a three dimensionally ordered state due to weak interactions between adjacent "sheets" or "chains." In the ordered state, the stronger low dimensional character manifests itself in the nature of magnetic-field-induced phase transitions. In this work we use a "spin polarization model" to describe the behavior of a magnetic system which undergoes a phase transition in applied field, and specify one particular class of such transitions as "metamagnetic."

The three dimensionally ordered magnetic state frequently reflects the symmetry of the crystal lattice. The concept of the magnetic space group and symmetry operations which pertain to axial vectors in a lattice are discussed. These theoretical concepts are then applied to two experimental investigations.

The first system, the copper (II) complex of the amino acid, L-Isoleucine, was interesting for several reasons. The crystal structure of this system is characterized by chemical bonds which extend only in one plane. In addition, the local coordination of the copper ion is five-fold square pyramidal. Low temperature and ultralow temperature measurements of the magnetic susceptibility in zero and applied fields are reported and discussed in terms of a model Hamiltonian. The magnetism of the $3d^9$ copper in the square pyramidal crystal field is investigated using electron spin resonance and discussed using the Van Vleck point charge model for crystal field interactions.

The second system, manganese bromide trimethyl amine dihydrate, has the disadvantage that the exact crystal structure is at present unknown. X-ray diffractometry and optical goniometry are used to derive the crystallographic point and space groups. Nuclear magnetic resonance measurements in the three dimensionally ordered state are combined with other magnetic studies to suggest a crystal

structure and a magnetic space group. Finally a transition which is observed in applied field is discussed and asserted to be metamagnetic.

CHAPTER 1

THEORY

I. Low Dimensions: An Historic Overview

The existence of long range order as a result of superexchange, depends not only on the nature of the exchange but on the dimensionality of the interaction as well. Long range order is defined as the existence of a nonzero value for the magnitude of the spin-spin correlation function:

$$W \equiv \langle \vec{S}_i \cdot \vec{S}_{i+\Delta} \rangle \tag{1}$$

in the limit "Δ", the separation between spins goes to infinity. While no rigorous proof exists, it is generally accepted that this implies:

$$\lim_{\Delta \to \infty} |\langle \vec{S}_i \cdot \vec{S}_{i+\Delta} \rangle| = |\langle S_i \rangle|^2 \tag{2}$$

(The brackets denote the thermal average.)

A nonzero value for the spin-spin correlation implies a nonzero value for $\langle \vec{S}_i \rangle^2$ and therefore for $\langle \vec{S}_i \rangle$. Since the magnetic moment is proportional to $\langle \vec{S}_i \rangle$, a system possessing a nonzero spin-spin correlation will also possess a spontaneous sublattice magnetization. Exchange arising from the overlap of electronic wave functions in low dimensions may result in a magnetic spin system which is characterized by the absence of long range order at any finite temperature.

For example, a magnetic spin system which interacts through an Ising exchange:

$$H = -\frac{1}{2}\sum_{i\neq j} J_{ij}\, S_{iz}\, S_{jz} \qquad (3)$$

in one dimension has been shown[1] not to exhibit long range order at any temperature above absolute zero. The two dimensional Ising model was first shown to possess a spontaneous magnetization by Onsager who presented his solution as a remark during the discussion following the presentation of a paper by Tisza[2] in 1942. Several years later, Onsager presented his formula for the spontaneous magnetization of the two dimensional Ising model. Onsager published only the results of his calculation[3], leaving the derivation to remain a mystery. Four years later, in 1952, C. N. Yang[4] finally deciphered the puzzle and presented his rather long and complex derivation of Onsager's results.

The three dimensional Ising model was investigated by R. B. Griffiths in 1967[5]. His solution established the existence of long range order for this model.

In 1966, Mermin and Wagner proved[6] that a system which interacts through a one or two dimensional Heisenberg exchange:

$$H = -\frac{1}{2}\sum_{i\neq j} J_{ij}\, \vec{S}_i \cdot \vec{S}_j \qquad (4)$$

cannot possess a spontaneous magnetization at a finite

temperature. Stanley and Kaplan showed[7] that the absence of spontaneous magnetization as in the two dimensional Heisenberg model does not preclude existence of a magnetic phase transition characterized by a singularity in the susceptibility. Mermin and Wagner[8] also showed that the x-y model:

$$H = -\frac{1}{2}\sum_{i\neq j} J_{ij}\,(S_{ix}\,S_{jx} + S_{iy}\,S_{jy}) \qquad (5)$$

in one or two dimensions does not produce long range order.

II. Low Dimension and Metamagnetism

In real crystals, the effects of low dimensional correlations are usually seen in a limited temperature range. As the temperature is decreased, the thermal fluctuations become small enough so that some weaker interaction produces three dimensional ordering. The low dimensional character can still manifest itself in the behavior of the magnetically ordered spin system in applied field. For example a system which has a strong two dimensional Heisenberg ferromagnetic exchange may be considered as consisting of layers of ferromagnetic spins. If in addition, a three dimensional ordered state is produced by an antiferromagnetic coupling between the layers, a magnetic field applied in the appropriate direction may produce a magnetic phase transition which consists of reversing

alternate sheets to produce a ferromagnet. Such a transition is said to be "metamagnetic." We shall take as our definition of metamagnetism the following: In the presence of an applied field, a ferrimagnetic or antiferromagnetic system may undergo a phase transition characterized by an abrupt increase in magnetization. If the spin system consists of M sublattices and the transition involves a reorientation of N ($N < M$) of them, the transition is metamagnetic. The requirement that the magnetic spin system possess more than one sublattice precludes the existence of a metamagnetic transition in a ferromagnet. In the next section we consider the detailed conditions which result in metamagnetism.

III. Spin Polarization Energy

A rather elegant pedagogical technique for examining the behavior of a spin system has been communicated to me by Prof. R. D. Spence.[9] At zero temperature, a spin sublattice may be decomposed into basis states which represent the components of sublattices as polarization "states." For example a two sublattice system will have the spin polarization basis states:

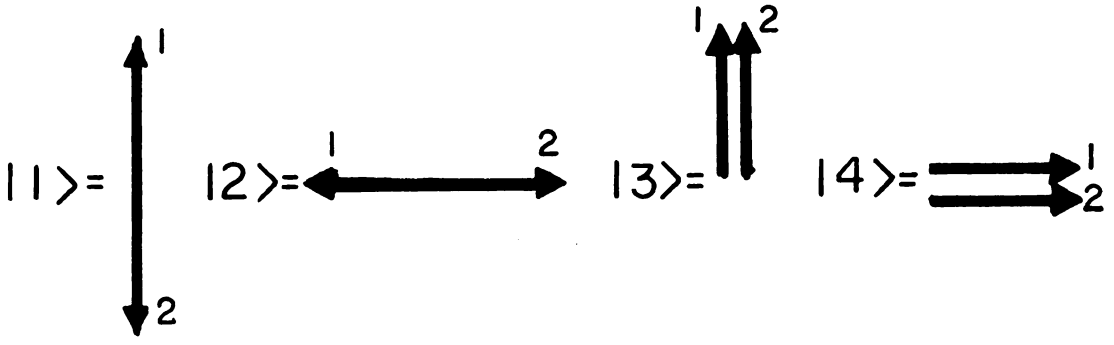

In these diagrams, each arrow or "spin" actually represents an entire sublattice. By using linear combinations of these basis states, we can form the sublattice configurations:

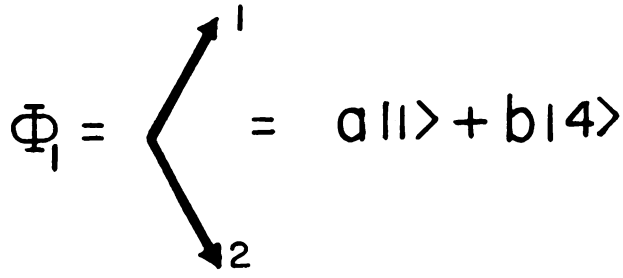

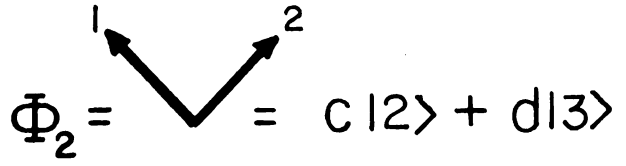

The coefficients depend on the details of the interactions (exchange, anisotropy, etc.) and are subject to the normalization:

$$a^2 + b^2 = 1 \tag{7}$$

The behavior of the magnetic system can be found by calculating the relative energy of each polarization. As this is a zero temperature model,the ground state completely characterizes the magnetic behavior. Let us consider, as an example, a simple two sublattice spin system in the presence of an isotropic antiferromagnetic exchange:

$$H = -J\vec{S}_1 \cdot \vec{S}_2 \tag{8}$$

where the S's represent sublattices and J represents the antiferromagnetic exchange between these sublattices. Then referring to the definitions of the polarization states (Fig. 1) we find the energies for the various states are:

$$E_1^\circ=+J \quad E_2^\circ=+J \quad E_3^\circ=-J \quad E_4^\circ=-J \tag{9}$$

where E_1° denotes the energy of the spin polarization state $|1\rangle$ in the absence of an applied magnetic field. The resulting "polarization energy diagram" or PED is shown:

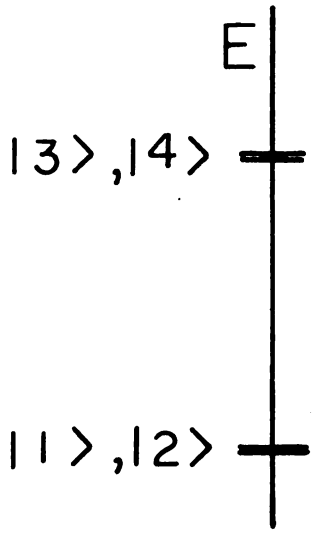

The presence of a field applied along the $\hat{z}$ axis of the state $|1\rangle$ will produce a state of mixed polarization:

$$\phi_2 = a(H)|2\rangle + b(H)|3\rangle = \vee \qquad (10)$$

where, as we have indicated, the coefficients are functions of the applied field. Because of the applied field, the sublattice Hamiltonian now has an additional term:

$$H = -J\vec{S}_1 \cdot \vec{S}_2 - \vec{H} \cdot \vec{M}$$

$$= -J\vec{S}_1 \cdot \vec{S}_2 - \vec{H} \cdot \Gamma(\vec{S}_1 + \vec{S}_2) \qquad (11)$$

where $\Gamma \equiv Ng\mu_B$

N = number of spins in sublattice

g = spectroscopic splitting factor

μ_B = Bohr magneton

The energy of the mixed state ϕ_1 in the presence of a field applied along the $\hat{z}$ axis is given by:

$$E = a^2 J_2^\circ + b^2 J_3^\circ + ab(J_{23}^\circ + J_{32}^{\circ\circ}) - 2\Gamma Hb \qquad (12)$$

where J_2° is the exchange energy between sublattice 1 and 2 when both sublattices are in the state $|2\rangle$. J_{23}° is the exchange calculated with sublattice 1 polarized as in the state $|2\rangle$ and sublattice 2 polarized as in the state $|3\rangle$. Since the polarization states $|2\rangle$ and $|3\rangle$ are orthogonal, J_{23}° and J_{32}° are both zero. Substituting from the normalization equation we find:

$$E(H) = (1-b^2)\, J_2^\circ + b^2 J_3^\circ - 2\Gamma HB \qquad (13)$$

The local minimum for this state is given by:

$$\frac{\partial E}{\partial H} = 0 = -2bJ_2^\circ + 2bJ_3^\circ - 2\Gamma H \qquad (14)$$

$$b = \frac{\Gamma H}{J_3^\circ - J_2^\circ} \qquad a = \left[1 - \left(\frac{\Gamma H}{J_3^\circ - J_2^\circ}\right)^2\right]^{1/2}$$

The energy in a field applied along $\hat{z}$ is:

$$E_{\phi_2}(H) = \left[1 - \left(\frac{\Gamma H}{J_3^\circ - J_2^\circ}\right)^2\right] J_2^\circ + \left(\frac{\Gamma H}{J_3^\circ - J_2^\circ}\right)^2 J_3^\circ - 2\Gamma H \frac{\Gamma H}{J_3^\circ - J_2^\circ}$$

$$= J_2^\circ \frac{\Gamma^2 H^2 [(J_3^\circ - J_2^\circ) - 2(J_3^\circ - J_2^\circ)]}{(J_3^\circ - J_2^\circ)^2}$$

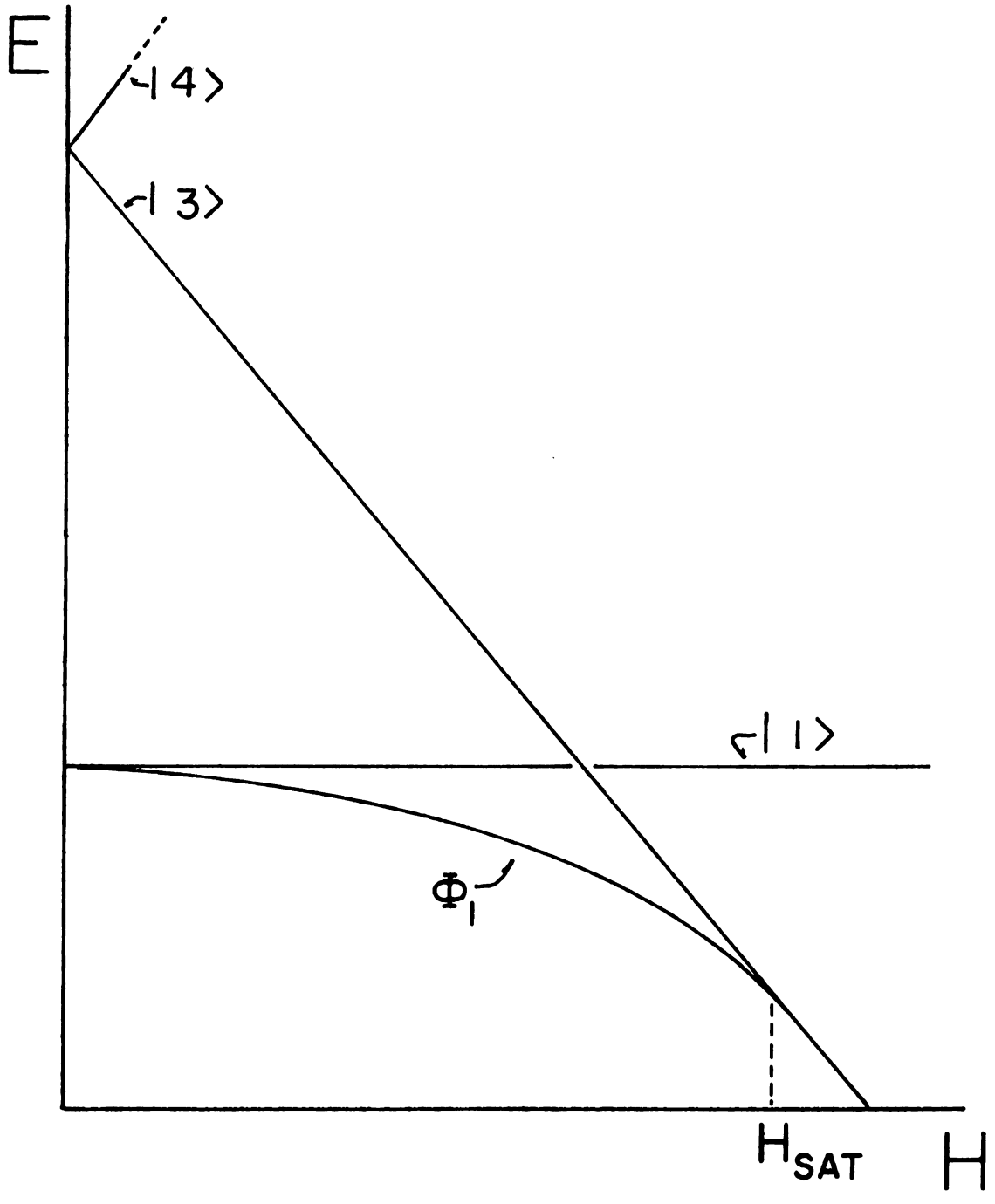

FIGURE 1. PED for a two sublattice uniaxial Heisenberg antiferromagnet (J<0).

$$E_{\phi_2}(H) = J_2^\circ - \frac{2\Gamma^2 H^2}{J_3^\circ - J_2^\circ} \tag{15}$$

The state $|1\rangle$ does not mix with $|3\rangle$ with $\vec{H}$ applied along the $\hat{z}$ axis. If we require that each of the sublattices in the mixed state:

$$\phi_2' = c|1\rangle + d|3\rangle \tag{16}$$

be normalized to unity:

$$\uparrow = c\uparrow + d\uparrow\uparrow = c+2d = 1 \tag{17a}$$

$$\downarrow = c\downarrow + 0 = c = 1 \tag{17b}$$

$$c = 1 \rightarrow d = 0 \tag{18}$$

where $\uparrow(\downarrow)$ represents a sublattice parallel (antiparallel) to the $\hat{z}$ axis. The PED for the two sublattice system in a field applied along $\hat{z}$ is shown in FIGURE 1 for $J<0$. The smallest finite field splits the states $|1\rangle$ and ϕ_1. The sublattices "flop" to a configuration which is perpendicular to the field. As the field increases, the sublattices rotate smoothly toward the field. At $H = H_{sat}$, the magnetization is saturated:

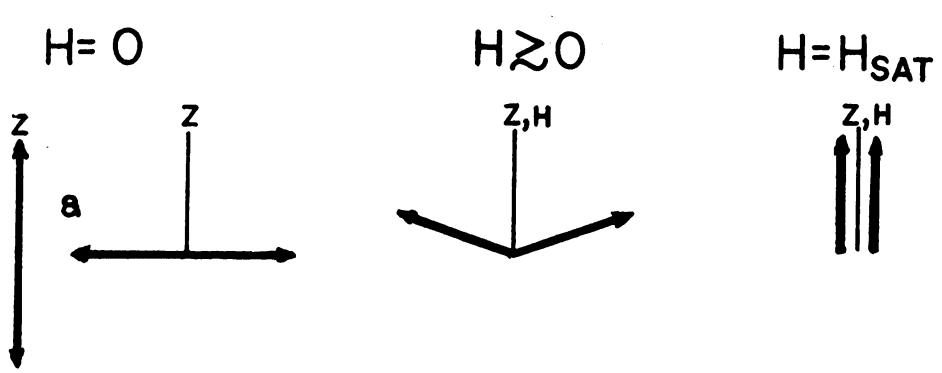

No sharp phase transition is produced. Next, consider an additional anisotropic interaction of the form

$$H = -k(S_{1z}^2+S_{2z}^2) \tag{19}$$

where k is a sublattice anisotropy constant. (The origins of interactions of this type are discussed in the next section.) The total Hamiltonian with a field applied along $\hat{z}$ is now:

$$H = -J\vec{S}_1 \cdot \vec{S}_2 - k(S_{1z}^2+S_{2z}^2) - \Gamma H(S_{1z}+S_{2z}) \tag{20}$$

This additional term splits the states |1> and |2> in zero field. The energy of each polarization state in zero field is:

$$E_1^\circ=-2k-J_1^\circ \quad E_2^\circ = +J_2^\circ \quad E_3^\circ=-2k+J_3^\circ \quad E_4^\circ=-2k+J_3^\circ \tag{21}$$

The energy of the mixed state ϕ_2 in an applied field is:

$$E_{\phi_2}(H) = -2k-J_2^\circ + \frac{-2\Gamma^2H^2}{-2k+J_3^\circ-J_2^\circ} \tag{22}$$

The PED for a field applied along $\hat{z}$ with anisotropy is shown in FIGURE 2 for $J<0$, $k>0$ and $|J|>2|k|$.

In this case, for $0<H<H_{SF}$, the sublattices are along the field. Since, as has been shown, this state does not couple to the polarization along the field, no moment appears and the system has no

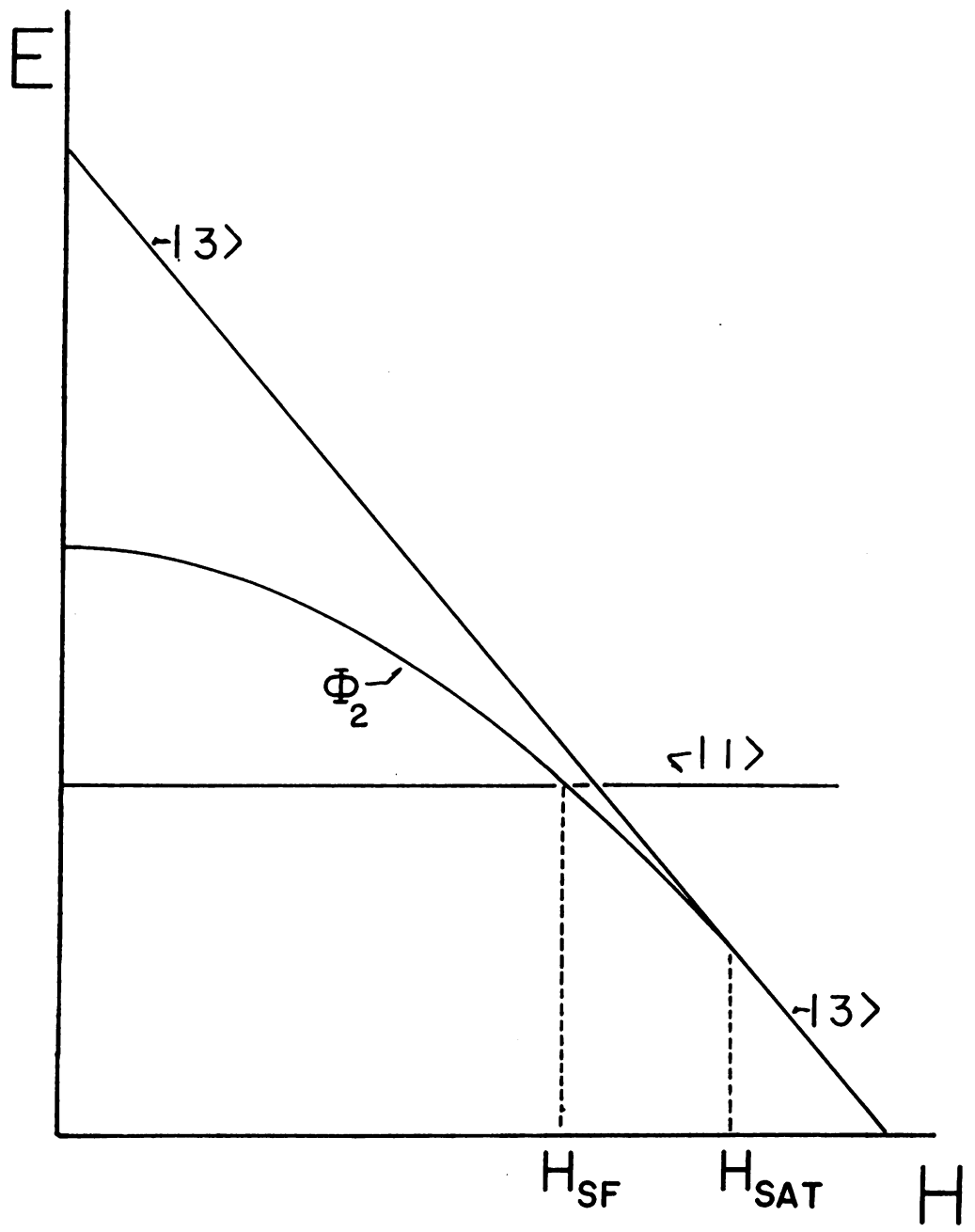

FIGURE 2. PED for a uniaxial antiferromagnet with weak anisotropy (k<J).

magnetic susceptibility. At $H=H_{SF}$, a "spin flop" transition reorients both sublattices so that they are almost perpendicular to the field with a small component (moment) along the field as a result of the mixed nature of ϕ_2. The moment continues to increase until $H=H_{sat}$:

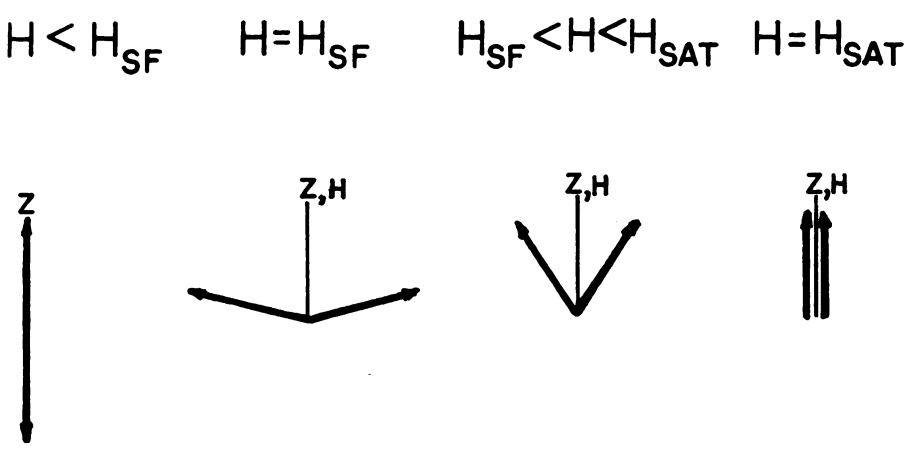

Now let us consider the case where k >> J. The energies in zero field are as before:

$$E_1^\circ = -2k+J \qquad E_2^\circ = +J \qquad E_3^\circ = -2k-J \qquad (23)$$

Because of the anisotropy, the state |2> is now highest in energy. The PED for this large anisotropy case is shown in FIGURE 3. In this situation, a direct transition occurs at $H=H_{crit}=\frac{J}{2\Gamma}$ from the pure antiferromagnetic state |1> to the pure ferromagnetic state |3>. The sublattice configurations for fields above and below H_{crit} are:

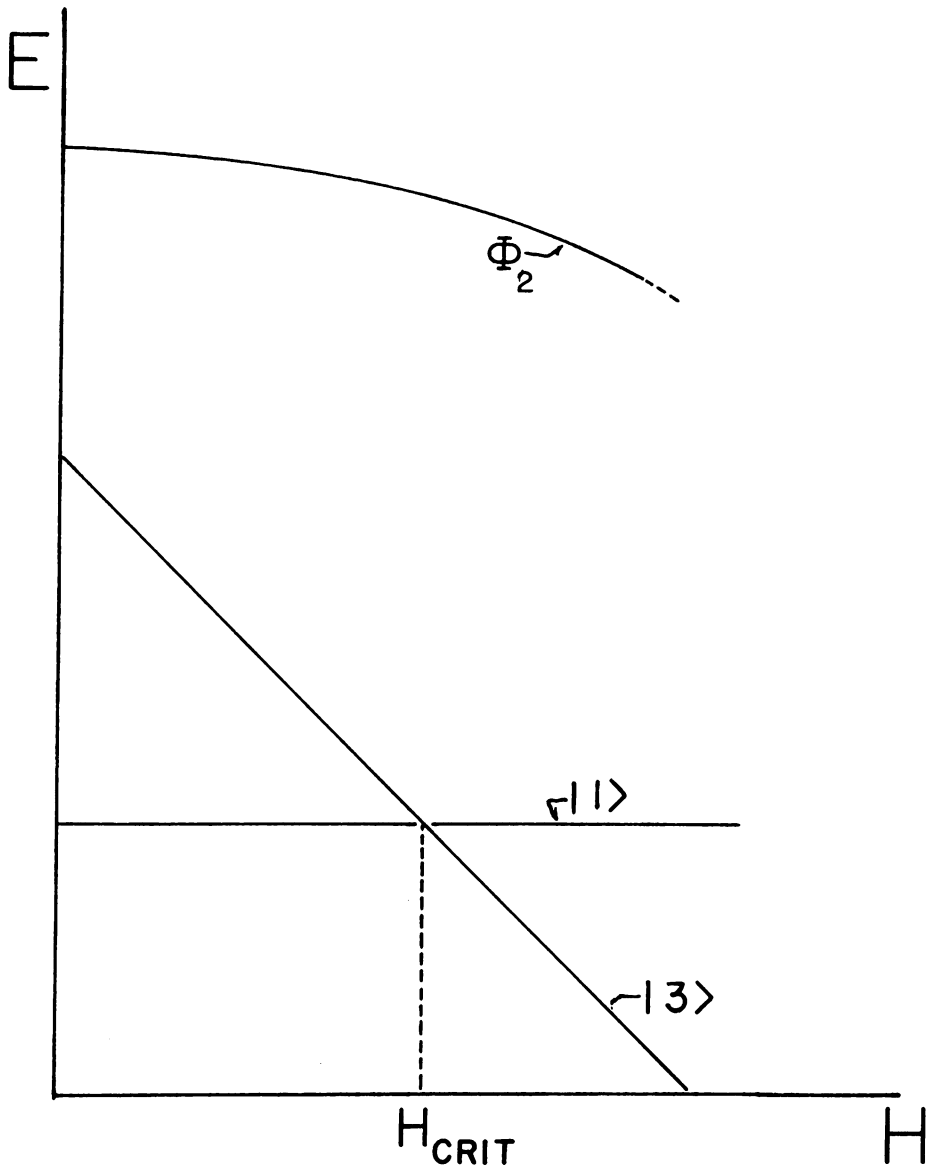

FIGURE 3. PED for a uniaxial antiferromagnet with strong anisotropy (k>>J).

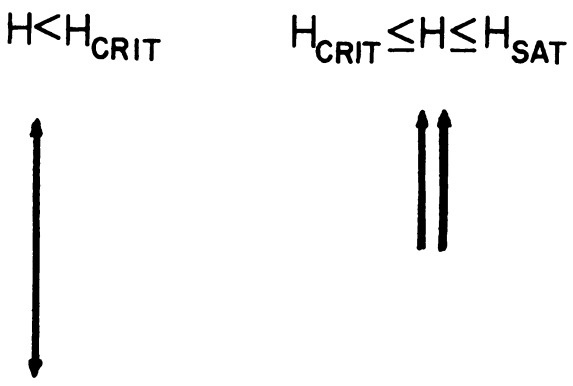

Since this transition has an abrupt increase in magnetization along the field and involves reversing only one of the two sublattices, the transition is metamagnetic .

We shall now turn to a more complicated example: the two sublattice canted antiferromagnet. This sublattice arrangement is such that the spins are no longer simply antiparallel along a particular axis but now are tipped or "canted" so they make some angle θ with the $\hat{z}$ axis.

This canted system has a net moment in the $\hat{x}$ direction whose magnitude depends on θ, the canting angle. This angle in turn, is a result of competition between the various sublattice interactions. Spin interactions which produce canted systems include competition between (1) first and second neighbor exchanges, (2) symmetric isotropic exchange and the antisymmetric Dzialoshinski-Moriya exchange($-\vec{D}\cdot\vec{S}_1 x \vec{S}_2$) and (3) anisotropic single ion interactions and exchange.

Closed form calculations for the two sublattice canted antiferromagnet are given in Appendix B for the case where the competing interactions are the Dzialoshinski-Moriya antisymmetric exchange and an isotropic antiferromagnetic exchange:

$$H = -J\vec{S}_1\cdot\vec{S}_2 - \vec{D}\cdot\vec{S}_1 x \vec{S}_2 \qquad (24)$$

In the presence of an applied field, closed form calculations become exceedingly complex. The analysis is often done[10] by using numerical methods on a computer. We will instead qualitatively discuss this example of the canted antiferromagnet using the PED technique. In zero field, the antisymmetric Dzialoshinski-Moriya term and the isotropic exchange term interact to produce states of mixed

polarization. Recalling the definition of the two sublattice basis states, we define two new mixed states:

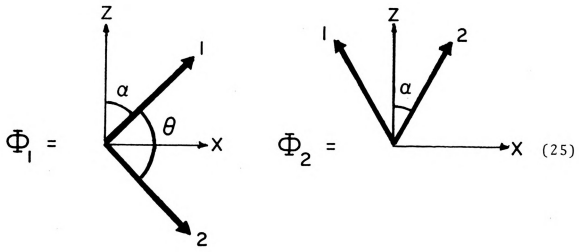

(25)

Assuming $\vec{D} = D\hat{y}$, the canting angle θ is found by minimizing the energy and is given by:

$$\tan 2\theta = \frac{D}{J} \tag{26}$$

where D is the Dzialoshinski-antisymmetric exchange constant. In the absence of an applied field, these two states are degenerate. A small field applied along the $\hat{z}$ axis will split the states leaving ϕ_2, which has the largest moment parallel to the field, lowest. The PED for the canted antiferromagnet is shown in FIGURE 4.

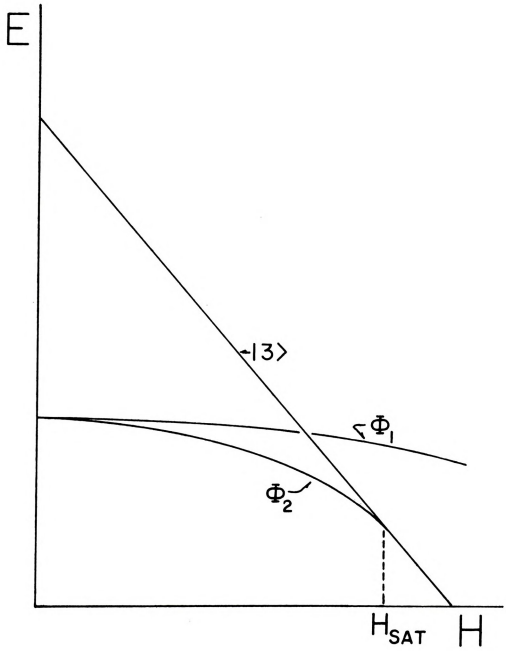

FIGURE 4. PED for the two sublattice canted antiferromagnet with no anisotropy.

For $H \gtrsim 0$, the sublattices "flop" into the mixed state ϕ_2. This state has a net moment which increases with increasing field. At $H=H_{sat}$, the spins are completely polarized along the field. No sharp transition is observed. This is consistent with the lack of anisotropy.

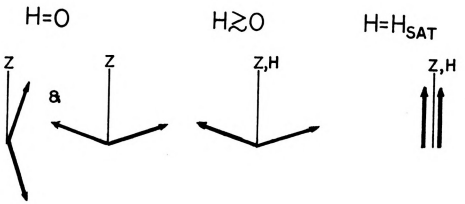

If we now apply an additional interaction of the form:

$$H = -k(S_{1z}^2 + S_{2z}^2) \qquad (27)$$

we will remove the degeneracy between the mixed polarization states Φ_1 and Φ_2. The canting angle in zero field will now also depend on the magnitude of k. If we parameterize the sublattice orientation energy in terms of an angle θ, we may calculate θ by minimizing the polarization

energy with respect to θ. The Hamiltonian,

$$H = -J\vec{S}_1 \cdot \vec{S}_2 - k(S_{1z}^2 + S_{2z}^2) - \vec{D} \cdot \vec{S}_1 x \vec{S}_2 \qquad (28)$$

with $k >> J > 0$

gives
$$E(\theta) = -S^2 J \cos\theta - DS^2 \sin\theta - kS^2 \cos^2\alpha \qquad (29)$$

$$= -S^2 J \cos\theta - DS^2 \sin\theta - kS^2 \sin^2\frac{\theta}{2}$$

Minimizing E with respect to:

$$\frac{\partial}{\partial\theta} = 0 = S^2 J \sin\theta - DS^2 \cos\theta - \frac{kS^2}{2} 2 \sin\frac{\theta}{2} \cos\frac{\theta}{2}$$

$$= J \sin\theta - D \cos\theta - \frac{k}{2} \sin\theta$$

$$\tan\theta = \frac{2D}{2J - k} \qquad (30)$$

The mixed state ϕ_1 will now have the lower energy in zero field. In an applied field, ϕ_2 will begin to descend in energy due to the Zeeman energy of the large net moment of this state. The resulting PED is shown in FIGURE 5. The relative spin configurations in applied field are shown below:

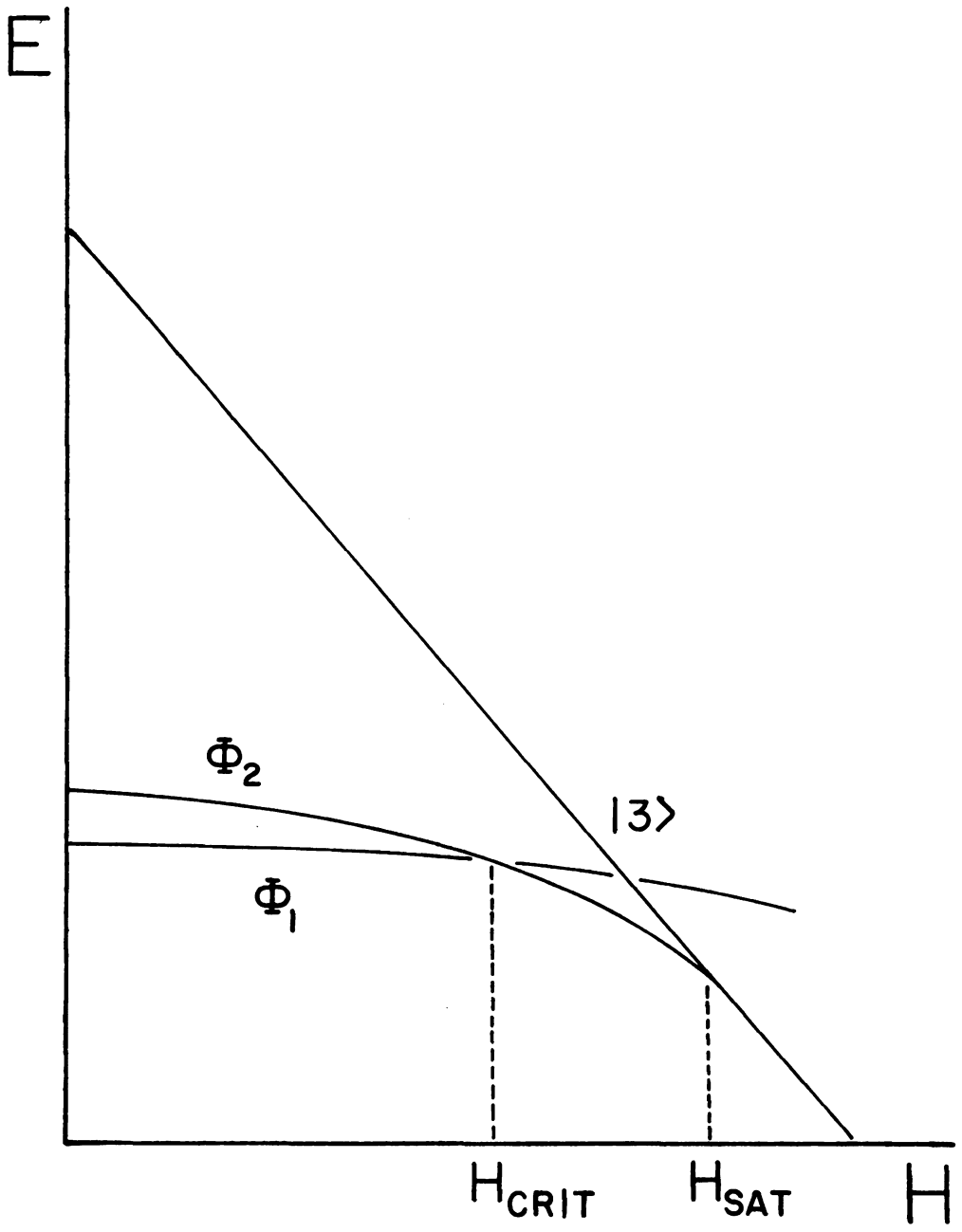

FIGURE 5. PED for the two sublattice canted antiferromagnet with anisotropy.

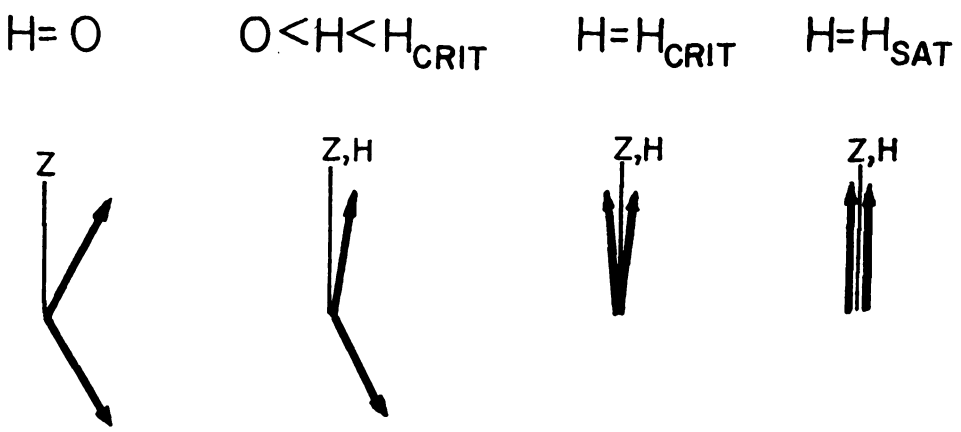

For $H<H_{crit}$, the system is mostly along the $\hat{z}$ axis but rotates slightly toward the field resulting in a nonzero susceptibility. This behavior manifests itself in the curvature of the energy of ϕ_1 in applied fields. At $H=H_{crit}$, an abrupt increase in magnetization occurs as the state ϕ_2 crosses ϕ_1. This results in a large net moment along the field. The moment continues to increase until $H=H_{sat}$. Without performing detailed calculations, we cannot say whether or not this transition is metamagnetic If the transition reverses the sublattice which was approximately antiparallel to the field while leaving the other sublattice unchanged, the transition is indeed metamagnetic. Finally, if the field is applied along either of the other two orthogonal directions, the spins smoothly

rotate toward the field until saturation occurs. This behavior is characterized by the absence of any sharp transition.

We shall discuss more complicated four sublattice canted systems in the context of experimental evidence in real crystals in later sections of this work.

As we have seen from the previous discussion, the role of anisotropy in magnetic transitions is crucial. Let us consider briefly the description of anisotropic interactions.

Anisotropic interactions produce the state of lowest energy with the spin sublattices oriented along a particular direction relative to a fixed set of coordinates in the crystal lattice. They differ in this respect from isotropic exchange interactions which depend only on the orientation of the spins relative to one another regardless of their orientation in the crystal. Anisotropic interactions arise physically from several different mechanisms.

We can divide anisotropic interactions into two categories: (1) those interactions which depend on the characteristics of the isolated ion in the lattice, and (2) those which involve interactions between two or more ions. Interactions which involve the characteristics of the isolated ion include interactions of the crystalline

electric field with the electronic multipole moment, and hyper-fine interactions between the electron and the ionic nucleus.

Spin-spin interactions which are anisotropic include magnetic dipole-dipole and Ising and x-y exchange interactions.

An excellent discussion of anisotropy is contained in an article by Kanamorai in the Magnetism[11] series edited by Rado and Suhl.

Having indicated some of the anisotropic interactions and noted their importance for a phase transition, we may further note that the exact nature of the transition depends on the relative strengths of the isotropic interactions compared to anisotropic interactions. As we have shown in the case of a uniaxial two sublattice antiferromagnet the condition $k>J$ produced a metamagnetic transition while $k<J$ gave a "spin flop" transition.

IV. Symmetry and the Magnetic Space Group

A principle attributed to Neumann states that "no measurement on a crystal can exhibit a greater space-time anisotropy than that of the crystal itself."[12] That is to say, any physical measurement involving the arrangement of atoms in a crystal, must reflect the symmetry operations contained in the crystallographic space group of the crystal. Magnetic measurements such as nuclear magnetic

resonance, which microscopically probe the symmetry of the magnetic spin system, reflect the properties of the operations contained not in the crystallographic space group but rather in the "magnetic space group." The magnetic space group consists of operations which affect axial vectors such as spin angular momentum, while the crystallographic space group contains operations pertaining to polar vectors such as the coordinates of atoms in a crystal. While there is no rigorous formal connection between the crystallographic space group and the magnetic space group, they often belong to the same family. Space groups which are members of the same family are derived from the same set of rotation operators called the "point group." In addition to the various symmetry operations contained in the crystallographic group, the magnetic group may also contain "anti-elements." An anti-element, which operates only on axial vectors, may be formed from a polar vector symmetry operator by "multiplying" it by the operation anti-inversion. (Multiplication is taken here to mean multiplication of the matrix representations of the two operations.) Anti-inversion reverses the direction of an axial vector. As an example, let us examine the operation "mirroring." The effect of a mirror plane on a polar vector is:

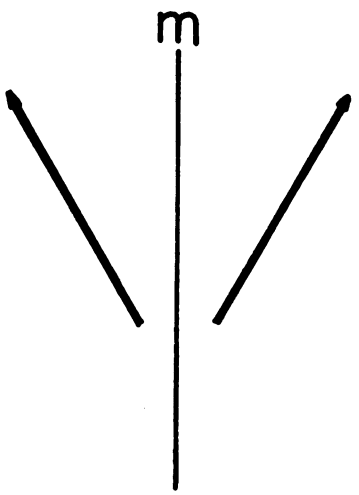

FIGURE 6. The mirror operation for a polar vector.

In the case of an axial vector however, the effect is quite different as shown:

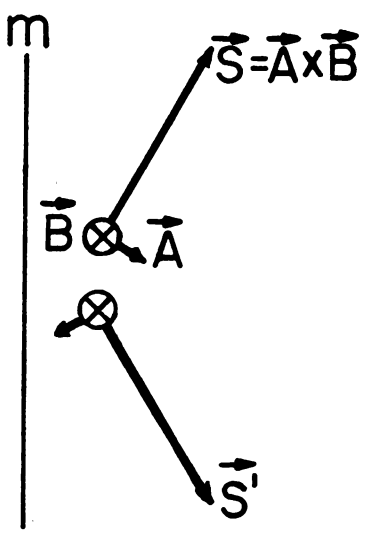

FIGURE 7. The mirror operation for an axial vector.

Now let us consider the effect of multiplying this operation by anti-inversion:

$$m' = m \times \bar{1}' \tag{31}$$

We first perform the mirroring operation on the axial vector as shown in FIGURE 7. We then reverse the direction of the axial vector producing the configuration:

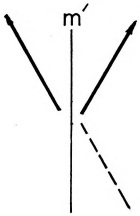

Several of the more common elements of the magnetic space group are shown in FIGURE 8.

We note that a nearest neighbor anti-translation reverses the spins along a given direction. This then doubles the separation between spins which are parallel. If an anti-translation is present in the magnetic space group it (1) produces antiferromagnetism and (2) doubles the size of the magnetic unit cell relative to the crystallographic cell.

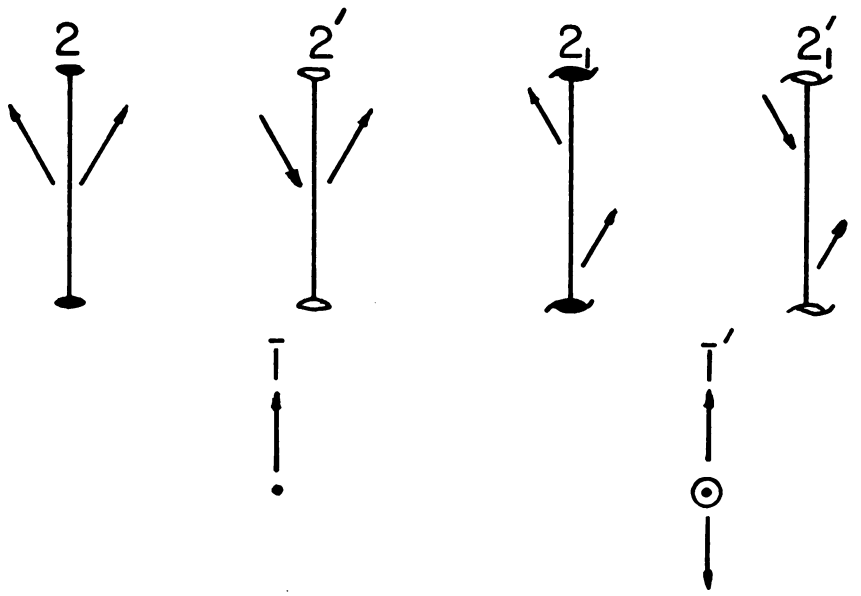

FIGURE 8. Symmetry operations for axial vectors.

The effects of point group operations which consist of rotations, reflections and inversions, shown in FIGURE 8 apply to spins which occupy general positions in the magnetic unit cell. If a spin occupies a special position such as on a two-fold rotation axis, in a mirror plane or on an inversion point, the operations produce stringent restrictions on the orientations of the spin. For example, if a spin is located on a two-fold axis, for every component of the spin which is perpendicular to the axis, the two-fold operation produces an equal but oppositely directed component which will cancel it. The component of the spin parallel to the two-fold axis will be unaffected by the rotation. Therefore, a spin which is

located on a two-fold axis can only have a nonzero moment parallel to the axis. A summary of the requirements of special positions for other operations is given in TABLE I.

Detailed discussions of the spin configurations produced by specific groups will be left until consideration of experimental results in later sections.

TABLE I

Restrictions of special spin positions

Spin In or On Position Of	Spin Orientation Requirements
n fold rotation axis	spin must be parallel to n-fold axis
n fold screw axis	no requirement
mirror plane	spin must be perpendicular to the mirror plane
anti two-fold axis	spin must be perpendicular to the two-fold axis
anti n (n>2)-fold axis	forbidden! spin may not occupy an anti n-fold axis.
n-fold anti screw axis	no requirement
anti mirror plane	spin must be parallel to the anti mirror plane
inversion point	no requirement
anti inversion point	forbidden! spin cannot occupy an anti inversion point

V. Chemical Bonding

We shall be discussing the following kinds of chemical bonds in the context of transition metal ions in organic complexes: (1) ionic bonding and (2) covalent bonding which bond the transition metal to its local atomic neighbors and (3) "weak ionic" bonding and (4) hydrogen bonds which bond large molecular subunits together to form a crystal.

We shall begin our discussion with ionic bonding. Ionic bonding is the result of electrostatic Coulomb interactions which causes a positively charged cation to be attracted to a negatively charged anion. The interaction may result between two ionized atoms such as sodium and chlorine in NaCl, or between a polarized system like H_2O and an ion such as a transition metal. In this last case, the polar water molecule orients itself so that the oxygen which is slightly negatively charged is pointing towards the positively charged transition metal ion.

Covalent bonding is said to occur when there is significant overlap of atomic wavefunctions so as to allow an electron to be transferred from a central ion to the overlap region. In the case of transition metal ions, the orbitals that overlap are not simply the occupied 3d orbitals but usually are "hybridized" orbitals. These orbitals consist of linear combinations of the 3d, 4s, and 4p orbitals. Linus Pauling has indicated[13] that the correct

combination of orbitals for covalent bonding is the one which is most directed toward the ligands.

Having established two methods for "gluing" ions together, let us examine ways of taking these molecular subunits and "sticking" them together to make a crystal. One of the simplest ways is simply the extension of ionic bonding to the larger subunits. As we have seen, ionic bonding holds the sodium to the chlorine in NaCl. This bonding of Na^+ to Cl^- extends throughout the crystal forming the lattice. This concept may be extended to larger subunits than two interacting ions. For example, a transition metal ion can coordinate with several negatively charged ligands as to yield a molecular subunit which has a slightly negative charge. An ionic interaction of a somewhat weaker nature may take place between this slightly negative subunit and a correspondingly positively charged subunit consisting of organic molecules such as methylanime groups. Since the charge is not localized the interaction which is frequently called "weak ionic" bonding,is usually weaker than ionic bonding between atoms.

Finally, there is a localized electrostatic interaction called "hydrogen bonding" which is frequently responsible for coordinating large molecular subunits in crystals. Hydrogen bonding is thought to occur when an electron rich atom such as an oxygen in one molecule approaches a slightly acidic (electron depleted) hydrogen

atom[14]. The hydrogen atom may be bonded to nitrogen for example, and carries a partial positive charge. A localized electrostatic interaction, as shown takes place:

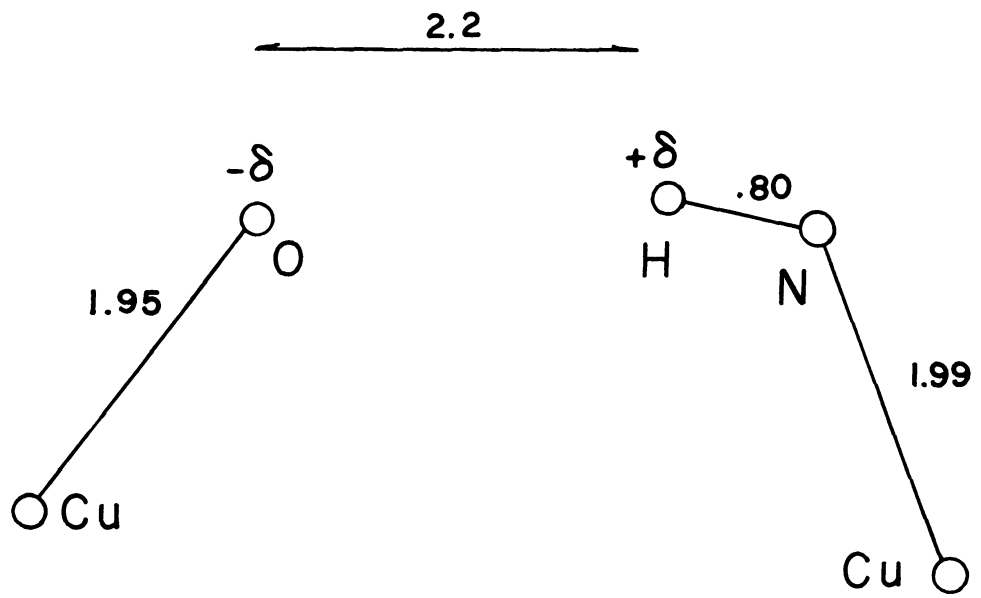

FIGURE 9. The hydrogen bond

The actual length of this bond is approximately 2Å which is thought to be too long to allow much covalent overlap. Typical energies for this interaction are 6 kcal which is between the covalent bonding (10-25 kcal) and the Van Der Waal's (1-5 kcal) bonding. The distance separating the atoms and the lack of real electronic wave function overlap tend to imply that a hydrogen bond is

an extremely poor path for superexchange.

VI. Crystal Field Theory

The five d electronic orbitals of an isolated transition metal ion are degenerate. In a crystal, these orbital energies are split by an electrostatic interaction which occurs between the d electrons of the ion and the electrons on the surrounding atoms or "ligands." In general, exact calculations of the electrostatic "crystal field" energy are a difficult and complex undertaking. The difficulty comes about because in a crystal, neither the transition metal electrons nor the ligand electrons are completely localized. Due to the rather complex types of bonding which can occur in a crystal, the electronic wavefunctions are no longer adequately described by wave functions of the isolated atom. More complex "hybridized" orbitals which consist of linear combinations of atomic wavefunctions are employed to describe the electrons.

However, under certain conditions, the bonding of the transition metal ion to its ligands is mostly ionic. The covalent nature of the bonding is not necessarily nonexistent but it is small enough so that to a very good approximation, the electrons are localized on the transition metal ion and can be adequately described by the d

atomic orbitals. In this situation, we may use the so-called "crystal field theory." The first investigation of the interactions of the ionic electrons and the crystalline electric field was by Becquerel[15] in 1929. At the same time Bethe[16] used group theory in conjunction with the relative strengths of the interactions to show how the energies of the atomic orbitals are modified by the ligands. In 1932, Van Vleck[17] succeeded, on the basis of a "point charge" approximation, in explaining the "quenching" of the orbital angular momentum and the resulting spin-only magnetic moment of paramagnetic transition metal ions. Van Vleck later went on to show[18] that Bethe's original crystal electric field ideas could be generalized and included in a more modern molecular orbital approach. In 1952, however, Kleiner[19] pointed out that if the classic electrostatic model is used to calculate the splitting of the orbital energies the sign of the splitting is actually reversed if an extended electron cloud model is used in place of the point charge model. A more recent quantum mechanical approach by Tanabe and Sugano[20] showed that even in certain "ionic" crystals such as $KNiF_3$[21], the itinerant or nonlocalized behavior of the transition metal electrons makes the dominant contribution to the crystal field splitting. This strongly suggests that although the point charge model of Van Vleck qualitatively, and often quantitatively yields the correct

result, more of the details of the nonlocalized quantum mechanical interactions are needed for a comprehensive theory.

Having outlined some of the deficiencies of the point charge model, we will use it to qualitatively discuss the effects of the crystal field on the orbital and spin states of transition metal ions. In this theory, we replace the atoms which surround the transition metal ion with point charges. An electrostatic repulsion will occur between the electrons in the d orbitals and these point charges. This interaction will be strongest for those orbitals which have the greatest spatial extent or "point" towards the ligand point charges. The energy of these orbitals will then be split from orbitals which do not extend toward the ligands. For example, let us consider an octahedral ligand coordination as shown in FIGURE 10a. The spatial extent of the d orbitals is shown in FIGURE 10b. By examining the relative orientations of the d orbitals and the six ligands, we see that the $d_{x^2-y^2}$ and d_{z^2} orbitals point directly towards the ligands, while the dxy, dxz and dyz orbitals all extend between the ligands. Calculations show the "e_g"^{2} orbitals ($d_{x^2-y^2}$, d_{z^2}) are degenerate and split from the remaining "t_{2g}" (d_{xy} d_{xz} d_{yz}) orbitals as shown in FIGURE 11.

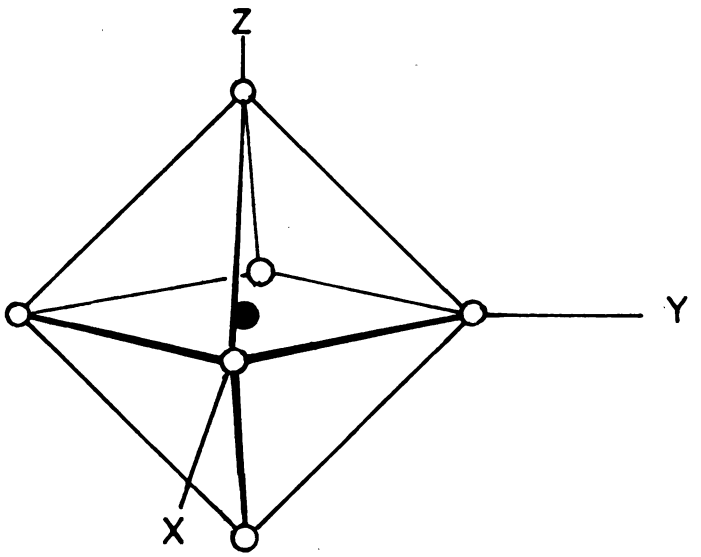

FIGURE 10a. Octahedral coordination of ligands.

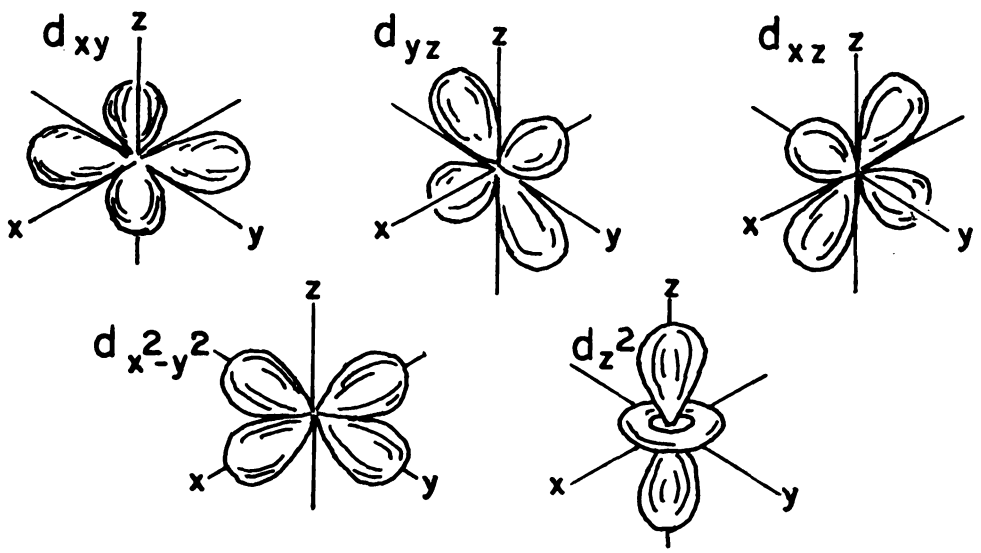

FIGURE 10b. Spatial extent of the d orbitals.

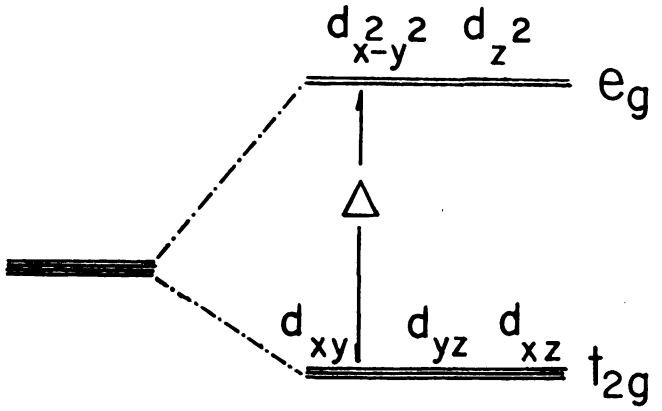

FIGURE 11. Splitting of the d orbitals in an octahedral environment.

Let us examine the effect of this interaction on the orbital and spin angular momenta in the case of five electrons ($3d^5$). When we examine the energies produced by occupying these orbitals, we must consider the relative strengths of two competing interactions. The first interaction, the energy which results from occupying the higher e_g orbitals can in theory be minimized by occupying only the t_{2g} orbitals. However, there is an electron-electron

repulsion interaction which occurs strongly between electrons in the same orbital. It is instructive to consider the two limiting cases.

In the first, the so-called "weak ligand field" case, the splitting Δ between the t_{2g}'s and the e_g's is small compared to the electron-electron repulsion energy. In this case the orbitals will be singly occupied. Hund's rule for coupling spin indicates the five electrons should all be "spin up" to give the maximum total spin of S=5/2. However, the Pauli exclusion principle states that no electrons can have the same quantum numbers. Since all five spins have the same spin projection, they must each have a different ℓ_z quantum number. One can see that the sum of all five projections (2, 1, 0, -1, -2) is zero. The result is that the total orbital angular momentum is L=0 (S-state).

The other limiting case, the "strong ligand field" occurs when Δ is large compared to the electron-electron repulsion. In this case the minimum energy occurs with all five electrons occupying the t_{2g} orbitals. The Pauli exclusion principle forces the electrons in doubly occupied orbitals to have their spins "paired" antiparallel. The four "paired" spins have zero net spin angular momentum. The only contribution to the spin comes from the single unpaired spin. This results in an S=1/2 spin state for the atom.

The strong ligand field results in low spin systems, while the weak ligand field results in high spin.

VII. The Internal Field in a Magnetic Sample

The magnetization for a paramagnet in an external field is given by:[23]

$$M(H,T) = Ng\mu_B SB_s(x) \qquad (32)$$

where Bs(x) is the Brillouin function

$$Bs(x) = \frac{2S+1}{2S} \coth \frac{(2S+1)X}{2S} - \frac{1}{2S} \coth \frac{X}{2S} \qquad (33)$$

with $$X = \frac{g\mu_B HS}{kT}$$

and

N = Avogadro's number

g = spectroscopic splitting factor

μ_B = Bohr magneton

S = spin quantum

k = Boltzmann's constant

H = internal magnetic field

T = absolute temperature

As we shall see, the field inside a magnetic crystal is generally not equal to the applied field. The Brillouin function is plotted as a function of the argument "X" ($\frac{g\mu_B HS}{kT}$) in FIGURE 12. Let us examine the behavior of the magnetization for small values of X(high temperature and/or low field).

FIGURE 12. The Brillouin function.

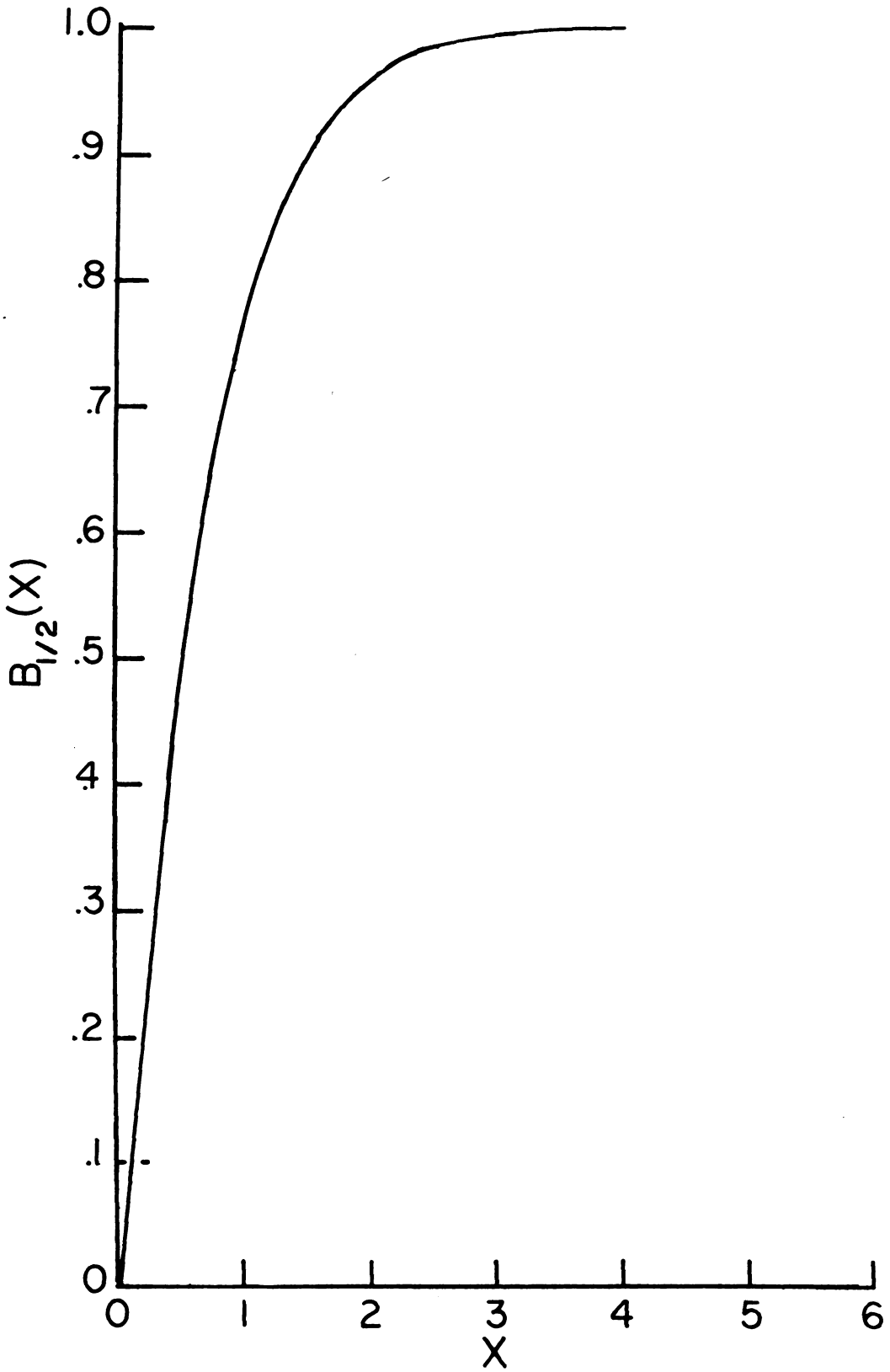
1.0
.9
.8
.7
.6
.5
.4
.3
.2
.1
0
$B_{1/2}(X)$
0
1
2
3
4
5
6
X

For $y<<1$: $\coth y = \frac{1}{y} + \frac{y}{3} + \ldots$ (34)

$$x<<1: M(H,T) = \frac{Ng\mu_B S}{kT}\left(\frac{2S+1}{2S}\quad\frac{2S}{(2S+1)x} + \frac{(2S+1)x}{3\cdot 2S}\right.$$

$$\left. - \frac{1}{2S}\quad\frac{2S}{x} + \frac{x}{3\cdot 2S}\right) = \frac{Ng\mu_B S}{kT}\left(\frac{2S+1}{2S}^{\,2}\,\frac{x}{3}\right.$$

$$\left. - \frac{1}{2S}\quad 2\,\frac{x}{3}\right) = \frac{Ng\mu_B S}{kT}\,\frac{x}{3}\left(\frac{4S^2+4S+1-1}{4S}\right)$$

$$= \frac{Ng\mu_B Sx}{3kT}\quad (S+1)$$

$$M(H,T) = \frac{Ng^2\mu_B{}^2\, S(S+1)H}{3kT} \tag{35}$$

$$= \frac{CH}{T} \tag{36}$$

where C, the "Curie" constant is

$$C = \frac{Ng^2\mu_B{}^2 S(S+1)}{3kT} \tag{37}$$

The magnetic susceptibility for this system in this limit can be calculated as:

$$\chi = \frac{dM}{dH} = \frac{C}{T} \tag{38}$$

which in this case is identically equal to $\frac{M}{H}$.

In actual experimental situations, the magnetization of the sample is measured as a function of the external applied field. The value of the magnetic field inside the

sample is modified by the magnetic moment $\vec{M}$ of the sample. Uncompensated magnetic "poles" or magnetic "charges" are induced on the surface of the sample by the external field. These "poles" in turn, induce a field inside the sample whose magnitude and direction depend on the shape of the sample and its net magnetization. For ellipsoidal samples the "demagnetizing" field is usually written[24]:

$$\vec{H}_{Demag} = -\vec{\vec{D}}\cdot\vec{M}\,\frac{\rho}{M.W.} \qquad (39)$$

where $\vec{\vec{D}}$ is the shape dependent "demagnetizing" tensor and $\vec{M}$ is the magnetization of the sample in magnetic moment/mole, ρ is the sample density and M.W. is the molecular weight.

In addition to the surface demagnetizing effects, the magnetic material inside the bulk of the sample also modifies the internal fields. The effects of the bulk of the sample excluding the demagnetizing fields are, in general, difficult to calculate exactly. A unique method for approximating the magnetic field at a point "P" inside the sample has been developed by Lorentz. In this analysis, we shall divide the sample into two regions by surrounding the point P with a sphere of radius R. R is assumed to be microscopically large so that the sphere can be considered uniformly magnetized material and macroscopically small so that the magnetic inhomogeneities of the sample may be neglected. We then "remove" the magnetic material inside the sphere and calculate the "Lorentz field" in the

resulting spherical cavity. The Lorentz field is given by[25]:

$$\vec{H}_{Lorentz} = \frac{4\pi}{3} \vec{M} \frac{\rho}{M.W.} \tag{40}$$

We may calculate the field at P due to the magnetic material contained inside the sphere by numerically summing the field at point P due to each dipole.

$$\vec{H}_{DIP} = \sum_j \frac{-\vec{\mu}_j + 3(\hat{n}_j \cdot \vec{\mu}_j)\hat{n}_j}{r_j^3} \tag{41}$$

where $\vec{\mu}_j$ is the dipole located a distance r_j from the point P. $\hat{n}$ is a unit vector which points from the dipole to P. The total internal field due to all these effects is:

$$\vec{H}_{int} = \vec{H}_{app} + \vec{H}_{LOR} - \vec{H}_{DEM} + \vec{H}_{DIP} \tag{42}$$

$$\vec{H}_{int} = \vec{H}_{app} + (\frac{4\pi}{3} - \vec{\vec{D}}) \cdot \frac{\vec{M}\rho}{M.W.} + \sum_j \frac{-\vec{\mu}_j + 3(\hat{n}_j \cdot \vec{\mu}_j)\hat{n}}{r_j^3} \tag{43}$$

The magnitude of the dipole field is usually small compared to the Lorentz and demagnetizing fields. For this reason it will be neglected in the discussion which follows.

We have shown that for small fields or high temperature:

$$\chi^\circ = \frac{M}{H_{int}} \quad \text{(emu/cc)} \tag{44}$$

where χ° is the magnetic susceptibility that would be observed in the absence of demagnetizing and Lorentz fields. Then:

$$\chi^\circ = \frac{M}{Happ + (\frac{4\pi}{3} - D)\frac{M\rho}{M.W.}}$$

$$= \frac{\frac{M}{Happ}}{1 + (\frac{4\pi}{3} - D)\frac{M}{Happ}\frac{\rho}{M.W.}}$$

Now if we define:

$$\chi_{meas} \equiv \frac{M}{Happ}$$

we can write

$$\chi^\circ = \frac{\chi_{meas}}{(1 + (\frac{4\pi}{3} - D)\chi_{meas}\frac{\rho}{M.W.}} \qquad (45)$$

Knowing the physical dimensions of a magnetic sample, its density and its molecular weight, we can correct the experimentally measured susceptibility as long as the measurement is made at small applied fields or high temperatures so that the magnetization is a linear function of the field.

CHAPTER 2

EXPERIMENTAL APPARATUS: MAGNETOMETER

I. Introduction

In order to measure the bulk magnetization of magnetic insulators, we have constructed a magnetometer capable of measuring magnetization at liquid He^4 temperature in applied fields up to 16 kOe. The design was suggested by an article by Mcquire[26] and is based on the original design of an induction magnetometer by Cioffi[27]. The magnetization of the sample is detected by measuring the EMF induced in a pickup coil when the sample is moved through the coil. The EMF is then electronically integrated to give the net change in flux caused by the moving sample. This change in flux is related to the bulk magnetization of the sample.

II. Theory

The magnetic fields of a uniformly magnetized sphere are given[28] by:

$$\vec{B}_{out} = \vec{H}_{out} = \frac{8\pi M_o R^3}{3r^3}\left(\cos\theta\hat{r} + \frac{\sin\theta}{2}\hat{\theta}\right) \qquad (46a)$$

$$\vec{B}_{in} = \frac{8\pi}{3} M_o \hat{z} \qquad (46b)$$

$$\vec{H}_{in} = \frac{-4\pi}{3} M_o \hat{z} \qquad (46c)$$

where $\vec{B}_{in}$ and $\vec{H}_{in}$ are the magnetic fields inside the sphere and

M_o = magnetization in emu/unit volume

R = radius of sphere

r = distance from center of the sphere

and $\hat{r}$ and $\hat{\theta}$ are defined:

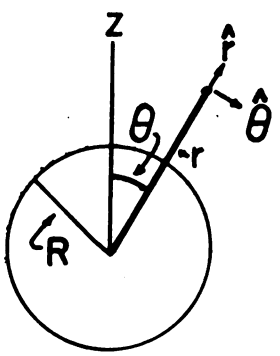

We note that the fields outside the sphere are those of a magnetic dipole of moment $\vec{\mu} = \frac{4\pi R^3}{3} M_o \hat{z}$.

Let us consider the flux through a loop of radius a with the sphere located a distance z away from the plane of the loop along the axis of the loop as shown in Fig. 27. The flux through the loop is given by:

$$\Phi = \int_S \vec{B}\, d\vec{A} = \int B_{norm} \times d \times d\phi \qquad (47)$$

$$= 2\pi \int_o^a B_{norm}\, xdx$$

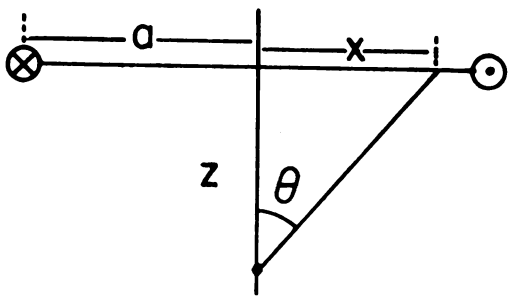

$$= 2\pi\mu \int_o^a \frac{3\cos^2\theta - 1}{r^3}\, x\,dx$$

$$= 2\pi\mu \int_o^a \left(\frac{3\left(\frac{z^2 x}{x^2+z^2}\right)}{(x^2+z^2)^{3/2}} - \frac{x}{(x^2+z^2)^{3/2}} \right) dx$$

$$= 2\pi\mu \int_o^a \left(\frac{3\, z^2 x}{(x^2+z^2)^{5/2}} - \frac{x}{(x^2+z^2)^{3/2}} \right) dx$$

$$\Phi\ (Z>R) = \frac{8\pi R^3 M_o}{3} \left(\frac{-z^2}{(a^2+z^2)^{3/2}} - \frac{1}{(z^2+z^2)^{1/2}} \right) \qquad (48)$$

If the sphere intersects the plane of the coil, we must modify the calculation due to the altered geometry:

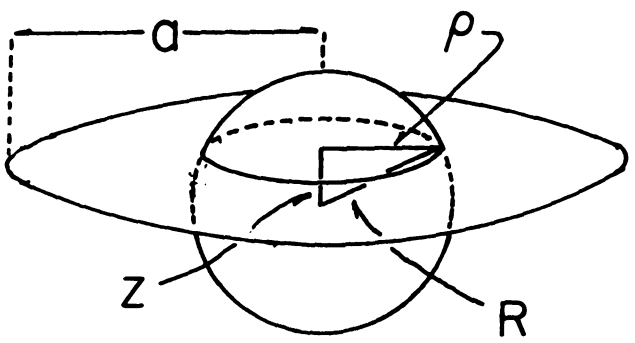

We may derive ρ from the equation of the circle which results from the intersection of the plane of the loop and the sphere:

$$\rho^2 = x^2 + y^2 \tag{49}$$

The equation for the sphere is:

$$R^2 = x^2 + y^2 + z^2 \tag{50}$$

Substituting from this last equation we find:

$$\rho = (R^2 - z^2)^{1/2} \tag{51}$$

The flux through the loop from the fields outside the sphere is given by:

$$\Phi_{out} = 2\pi\mu \int_{\rho}^{a} (B_{out})_{norm}\, x dx$$

$$= \frac{8\pi^2 R^3 M_o}{3}\left(-Z^2 \left(\frac{1}{(a^2+z^2)^{3/2}} - \frac{1}{R^3}\right) + \left(\frac{1}{(a^2+z^2)^{1/2}} - \frac{1}{R}\right)\right) \tag{52}$$

$$\Phi_{in} = 2\pi\mu\int_o^\rho (B_{in}) \text{ norm } x\,dx$$

$$= \frac{8\pi^2 M_o}{3}(R^2 - Z^2) \tag{53}$$

$$\Phi(Z \leq R) = \Phi_{out} + \Phi_{in} = \frac{8\pi^2 R^3 M_o}{3} \frac{-Z^2}{(a^2+z^2)^{3/2}}$$

$$+ \frac{1}{(a^2+z^2)^{1/2}} \tag{54}$$

Thus the flux through the loop has the same functional dependence for all values of z.

As the sphere is moved along the z axis the flux through the loop will change thereby inducing an EMF in the coil:

$$E = -\frac{\partial \Phi}{\partial t} \tag{55}$$

Integrating this EMF as a function of time:

$$\int E\,dt = -\int \frac{\partial \Phi}{\partial t}\,dt = -\Delta\Phi = \Phi(z') - \Phi(z) \tag{56}$$

Since the Φ involves the magnetization of the sample, we

can measure the magnetization by integrating the EMF induced in the coil. We note that this result is independent of the path of the sample, but involves only the flux indicated at the two end points.

In a practical experiment, the sensitivity and noise rejection of the apparatus can be improved by using an astatic pair of pickup coils. The experimental sample coils, shown in FIGURE 13, consist of two coaxial solenoids of N turns counterwound on the same cylindrical form. There are two advantages to such a system. The first is that any fluctuations in applied magnetic field will affect both coils equally. Since the coils are wound in opposite directions the EMFs induced by the fluctuating fields will have the opposite sign and cancel. The second advantage is that in addition to increasing the sensitivity by a factor of N over that of the single loop, the EMF's induced in the two coils by the moving sample will have the <u>same</u> sign and therefore will add. To calculate this, we must evaluate the flux through both coils as we move the sample from the center of one coil to the center of the other. However, by symmetry, the flux at the two end points should be the same. Therefore, it will suffice to evaluate the total flux with the sample in the center of one coil and then double the result. The detailed calculation involves summing the flux through each of the N

FIGURE 13. The magnetization apparatus.

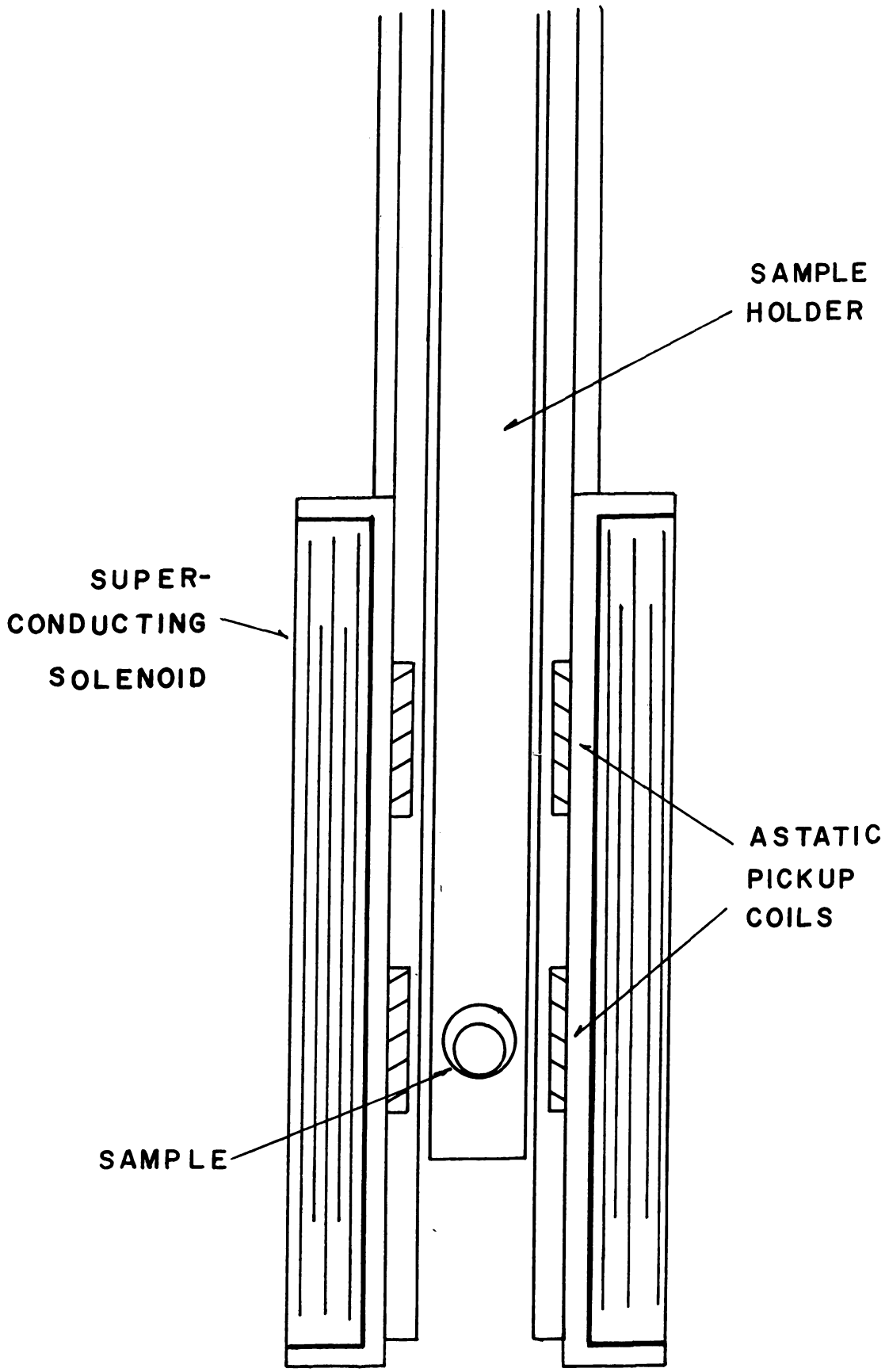
SAMPLE
HOLDER
SUPER-
CONDUCTING
SOLENOID
ASTATIC
PICKUP
COILS
SAMPLE

loops of the two coils:

$$\Phi_o = \sum_{i=1}^{2N} \Phi_i(z_i)$$

$$= \frac{8\pi^2 R^3 M_o}{3} \sum_{i=1}^{2N} \left(\frac{-z_i^2}{(a^2+z_i^2)^{3/2}} + \frac{1}{(a^2+z_i^2)^{1/2}} \right) \quad (57)$$

A computer calculation for the sample coils in our apparatus was carried out. The total flux change in moving the sample from one coil to another is:

$$\Delta\Phi_{tot} = 2\Phi_o = \frac{8\pi^2 R^3 M_o}{3} \quad (2.62 \times 10^3) \qquad (58)$$

III. The Cryostat

The cryostat is shown in FIGURE 13. The sample holder is supported by a piece of 1/4" thin wall cupronickel tubing. This tubing is fed through an 0-ring "Veeco" vacuum seal in the lid. The 0-ring makes a sliding contact with the tubing and allows movement of the sample without significantly affecting the vacuum over the helium bath. The static applied field is produced by a superconducting solenoid consisting of 14,712 turns of 0.0178 cm diameter copper jacketed Niobrum Zirconium wire wound on a form of "Synthane" type G-11 fiberglass epoxy.[29] The solenoid produces a field of 1680 oersteds per ampere. The maximum current at 1.1k is approximately 12 amperes which

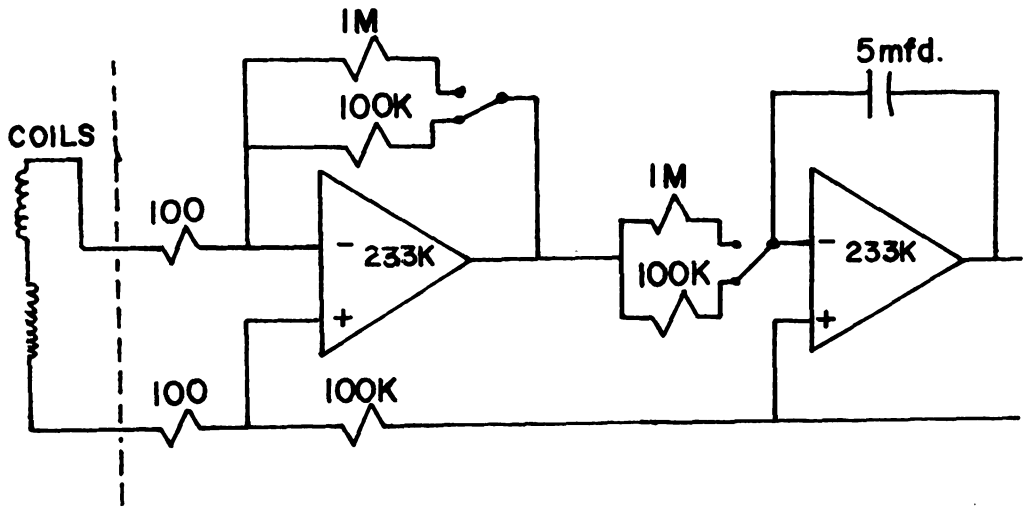

FIGURE 14. Circuit diagram for the amplifier and electronic integrator.

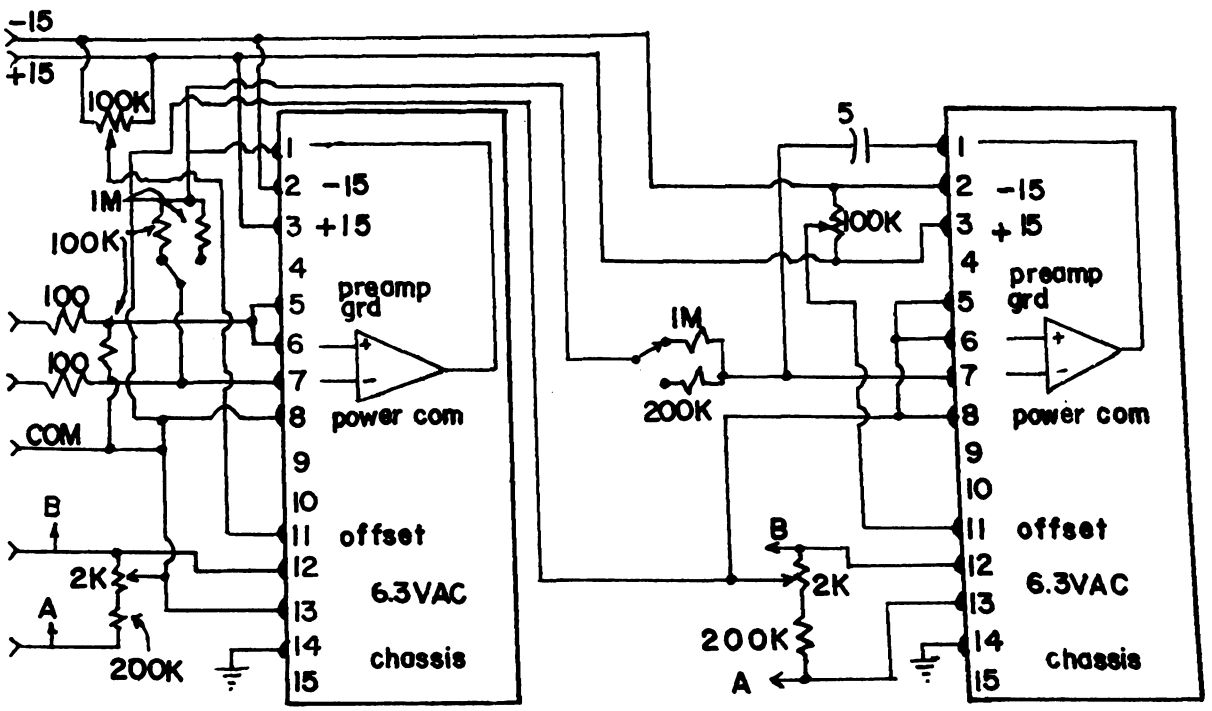

FIGURE 15. Schematic showing electrical connections of components.

gives a maximum field of 20 kilo-oersteds. The current is determined using a digital voltmeter to measure the voltage across a resistor connected in series with the solenoid. The value of the resistor is 1.31 ± .05 milliohms. The field in the solenoid as a function of the voltage across the series resistor is:

$$H(\text{oersteds}) = 1282 \times V_{res}\ (\text{millivolts}) \qquad (59)$$

The sample holder is machined from epoxied linen. The two pickup coils are wound astatically on a synthane type G-11 epoxy form. Each coil consists of approximately 2500 turns of number 36 enameled copper wire. The output of the pickup coils is connected to a differential amplifier and then to an integrator. Both the amplifier and the integrator utilize an Analog Devices Corporation model 233k chopper stabilized operational amplifier powered by an Analog Devices model 904 dual 15 volt power supply. The circuit is shown in FIGURE 14, and the schematic is shown in FIGURE 15. The gain may be switched from 1000 to 10,000 and the integration time constant can be set to either one or five seconds. The voltage output of the integrator is measured using a digital voltmeter. Typical integrated output voltages ranged from 15 millivolts to 9.5 volts with a signal to noise ratio of one at the lowest voltages. The zero offset of the operational

amplifiers must be periodically readjusted since the offset voltage will appear as an integrated signal. Typical drift rates are: 1 millivolt/second with a gain of 10,000 and a time constant of 5 seconds; 0.5 millovolts/sec with a gain of 10,000 and a time constant of 1 second; and 5 microvolts/second with a gain of 1000 and a 5 second time constant.

IV. Calibration

The overall calibration of the system was performed using a sample of ferric ammonium sulfate, $Fe_2(SO_4)_3\ (NH_4)_2\ (SO_4)\cdot 24H_20$. This material is an S=5/2 paramagnet at liquid He^4 temperatures. The magnetization is given by:

$$M(H,T) = (Ng\mu_B \tfrac{5}{2}) B_{5/2}\ (\frac{g\mu_B H}{kT}) \qquad (60)$$

The experimental data is shown in FIGURE 16. The solid line is a fit to the expression:

$$\frac{M.W.}{m} M(\text{volts}) = \frac{\tau}{A} K\ (\frac{\text{emu}}{\text{volt}\cdot\text{mole}})\ M(H,T) \qquad (61)$$

where M = is the integrated EMF in volts

M.W. = the molecular weight

m = the sample mass

K = the system calibration constant

τ = the integrator time constant

FIGURE 16. Magnetization of ferric ammonium sulfate. Solid curve is the theory.

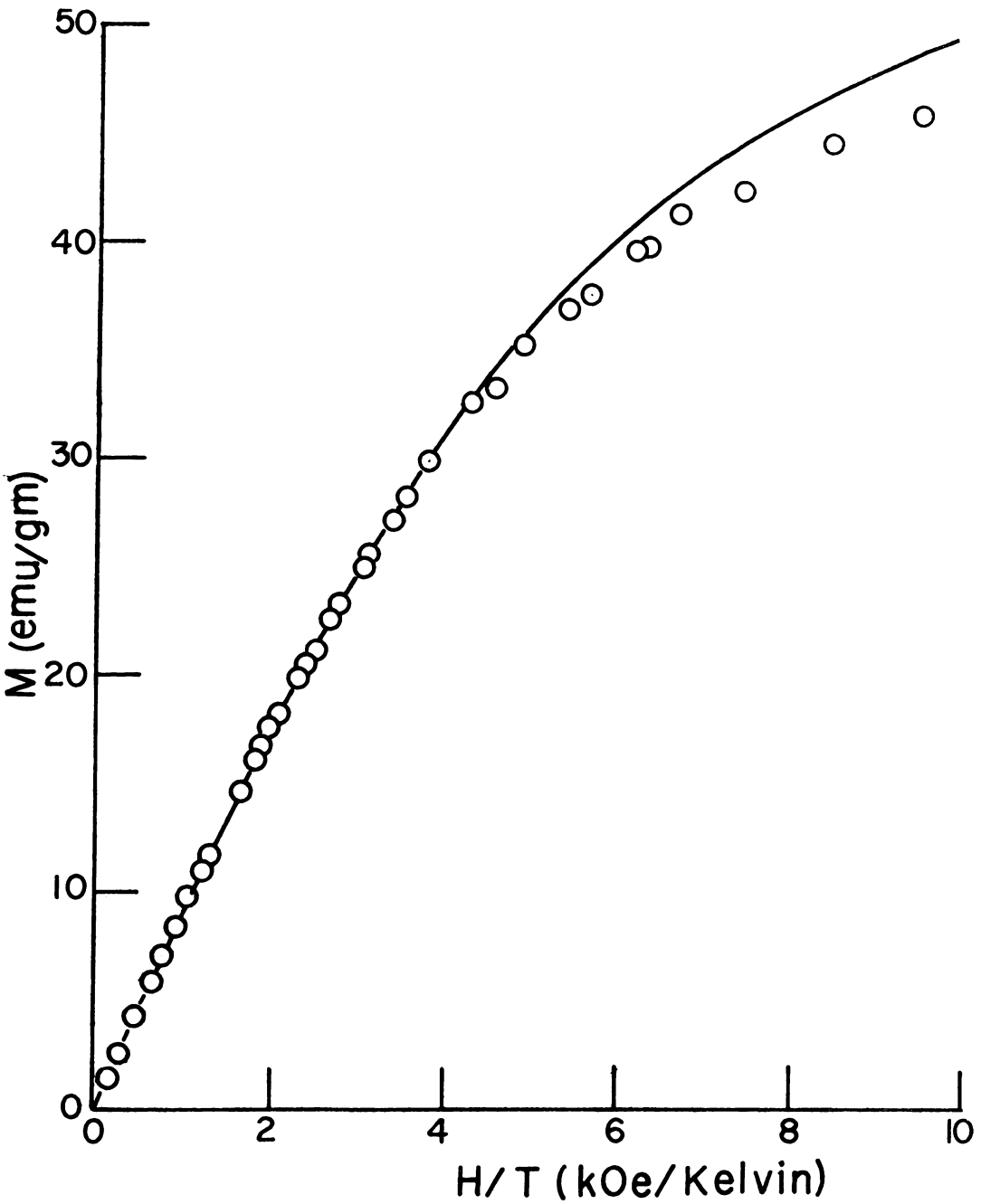
50
40
30
20
10
0
M (emu/gm)
0
2
4
6
8
10
H/T (kOe/Kelvin)

A = the amplifier gain

The derived calibration constant is:

$$K = (2.93 \pm .05) \times 10^{-5} \frac{\text{emu}}{\text{mole-volt}} \qquad (62)$$

We have previously derived (eq. 58) a theoretical expression for the EMF for our coils:

$$EMF = (2.62 \times 10^{3}) \frac{8\pi^2 R^3 M_o}{3}$$

with M_o in emu/cc. To compare this expression with our experimental value, we must convert it to the same units:

$$\frac{4\pi R^3 M_o}{3} = \text{magnetic moment in emu}$$

To express this in emu/mole, we multiply by m/M.W.:

$$\frac{4\pi R^3 M_o}{3} \frac{m}{M.W.} = \text{magnetization } (\frac{\text{emu}}{\text{mole}})$$

$$= \frac{EMF}{(2.62 \times 10^{3})2} (\frac{m}{M.W.})$$

$$K_{theor} = \frac{1}{(2.62 \times 10^{3})2} = 6.07 \times 10^{-5} \frac{\text{emu}}{\text{mole-volts}} \qquad (63)$$

Thus the constant derived from a theoretical expression differs from the experimental number by only a factor of two.

CHAPTER 3

MANGANESE BROMIDE TRIMETHYL AMINE

I. Introduction

Manganese bromide trimethyl amine dihydrate (MBTMA), $MnBr_3[(CH_3)_3NH]\cdot 2H_2O$ is a member of the general class of metallo-halide organic compounds: $MX_3[(CH_3)_3NH]\cdot 2H_2O$ (where M = Co, Cu, Ni, Mn and X = Cl, Br), which have been the subject of extensive structural and magnetic measurements.[30-33] In these compounds, the metal ion is generally octahedrally coordinated by two waters and four halides. The octahedra are edge shared along the halides so that the metal ion-ligand structure takes the form of chains or sheets giving rise to experimentally observed low dimensional magnetic behavior.

Although the crystal structure of MBTMA has not been determined, measurements of the magnetic specific heat[34] and zero field susceptibility[35] have demonstrated low dimensional behavior and a transition to a three dimensionally ordered state at 1.56K.[36]

NMR, magnetization and susceptibility (in applied field) experiments have led to a zero temperature model for the spin system and a tentative crystal structure which is

consistent with the space group derived from x ray analysis and is similar to the crystal structures for other members of this group of compounds.

II. Experimental

Large single crystals of $MnBr_3[(CH_3)_3NH]\cdot 2H_2O$ were prepared by reacting a 25% aqueous solution of $(CH_3)_3NH$ with $MnBr_2\cdot 4H_2O$. A solution of 48% hydrobromic acid, HBr, was then slowly added to the mixture. The resulting pinkish-orange solution was then filtered and slowly evaporated near room temperature. Within several days, well formed (FIG. 17) orange-pink crystals appeared. The solution was filtered and several small "seeds" were suspended on threads in the solution and allowed to continue growing. Upon reaching a mass of several hundred milligrams, the crystals were removed from the solution and used in the following experiments.

A. Crystallography The density of the crystal was determined by weighing the crystal in air and in methanol. The lattice dimensions and crystallographic space group were determined by x ray diffractometry of aligned single crystals using MoKα radiation. The lattice of MBTMA has dimensions: a = 8.45±.02Å b = 7.65±.02Å and c = 8.45±02Å and is monoclinic with an angle of $\beta = 91°56' \pm 4'$. The derived cell volume used in conjunction with the experimentally determined density indicates

FIGURE 17. The morphology of manganese bromide trimethyl amine dihydrate.

there are two molecular units in the crystallographic unit cell. The extinctions of every other reflection along the crystallographic b axis as well as the presence of the monoclinic angle imply the crystallographic space group $P2_1/m$. The point group 2/m was confirmed as was the monoclinic angle by measuring the crystal face normals using an optical goniometer.

B. Electron Spin Resonance Electron spin resonance was performed on an aligned single crystal at 9.2 GHz (x-Band) in applied fields up to 20 kilo-oersteds. The microwave cavity was immersed in liquid He^4 and measurements were made from 4.2 to 1.1K. Only one broad resonance ($\approx$2kOe. wide) was observed. Within experimental uncertainty the g-value and the line width are isotropic. The persistence of the single line through the Neel temperature (1.56K) with only a slight decrease in line width is thought to be due to regions of paramagnetic material. The crystal is very hydroscopic and some of the surface material may have been dissolved. This dissolved material would then behave as a paramagnetic glass at low temperatures.

No evidence of a $\vec{k}=0$ spin wave resonance was observed at the lowest experimental temperature of 1.1K.

C. Nuclear Magnetic Resonance Nuclear magnetic resonance experiments were performed on aligned single crystals immersed in liquid He^4 using a marginal oscillator. The spectrum in zero applied field was recorded at T=1.1k and is shown in TABLE II. The line which occurred at 18.74 MHz (at 1.1K) was recorded as a function of temperature and is shown in FIGURE 18.

Deuterated crystals of MBTMA were prepared by first heating $MnBr_2 \cdot 4H_2O$ to drive off the waters of hydration. The resulting powder was then reacted with $(CH_3)_3NH$ in D_2O in the presence of hydrobromic acid HBr. Crystals were again produced by slow evaporation. This time, however, the evaporation took place in a desiccator and great care was taken to prevent H_2O from contaminating the crystals. The spectrum for the resulting deuterated crystals was recorded in zero applied field below T_N. The lines at 18.17 and 18.74 MHz decreased by almost two orders of magnitude. Since it is expected that there is no significant exchange of hydrogen atoms for deuterons in the methyl or amine groups, it is probable that only the waters of hydration were replaced by D_2O. We infer that the two NMR lines which decreased in magnitude in the deuterated crystal are due to the protons in the residual waters of hydration. No other lines were affected by the deuteration.

An applied field of 300 oersteds was used to probe the rotational symmetry of the magnetically ordered

TABLE II

Zero field NMR frequencies and line widths in MBTMA (T=1.1K)

ν(MHz)	$\Delta\nu$(KHz)	ν(MHz)	$\Delta\nu$(KHz)	ν(MHz)	$\Delta\nu$(KHz)
1.53	250	8.15	250	26.91	125
1.86	200	9.76	200	28.56	125
1.94	250	18.17	250		
3.195	250	18.74	250		
7.68	250	23.50	125		

FIGURE 18. Temperature dependence of a proton nuclear magnetic resonance frequency in MBTMA.

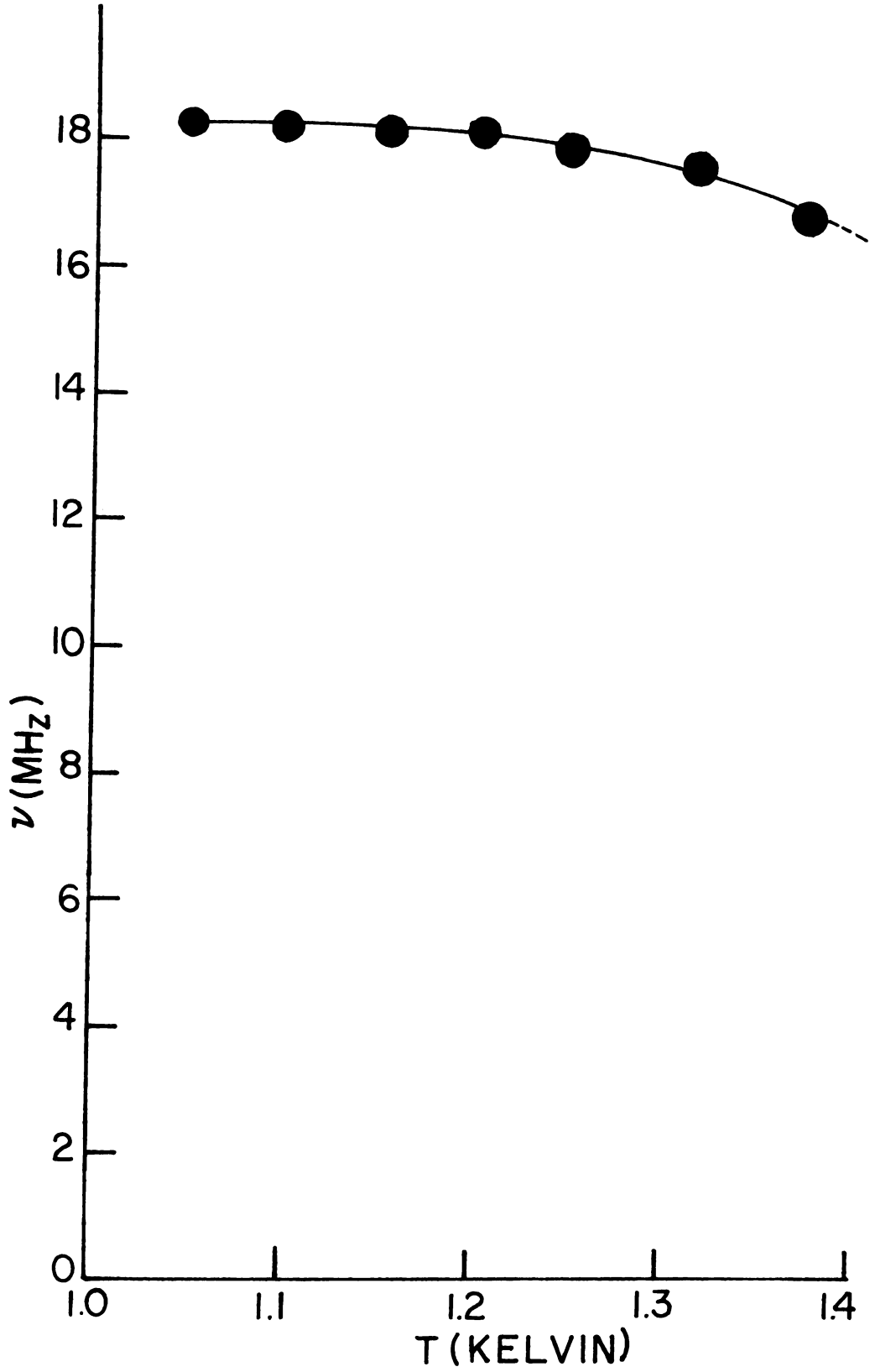
18
16
14
12
10
8
6
4
2
0
ν (MHz)
1.0
1.1
1.2
1.3
1.4
T (KELVIN)

FIGURE 19. Rotation diagram for proton nuclear magnetic resonance in MBTMA with an applied field of 300 0e. (T=1.1K).

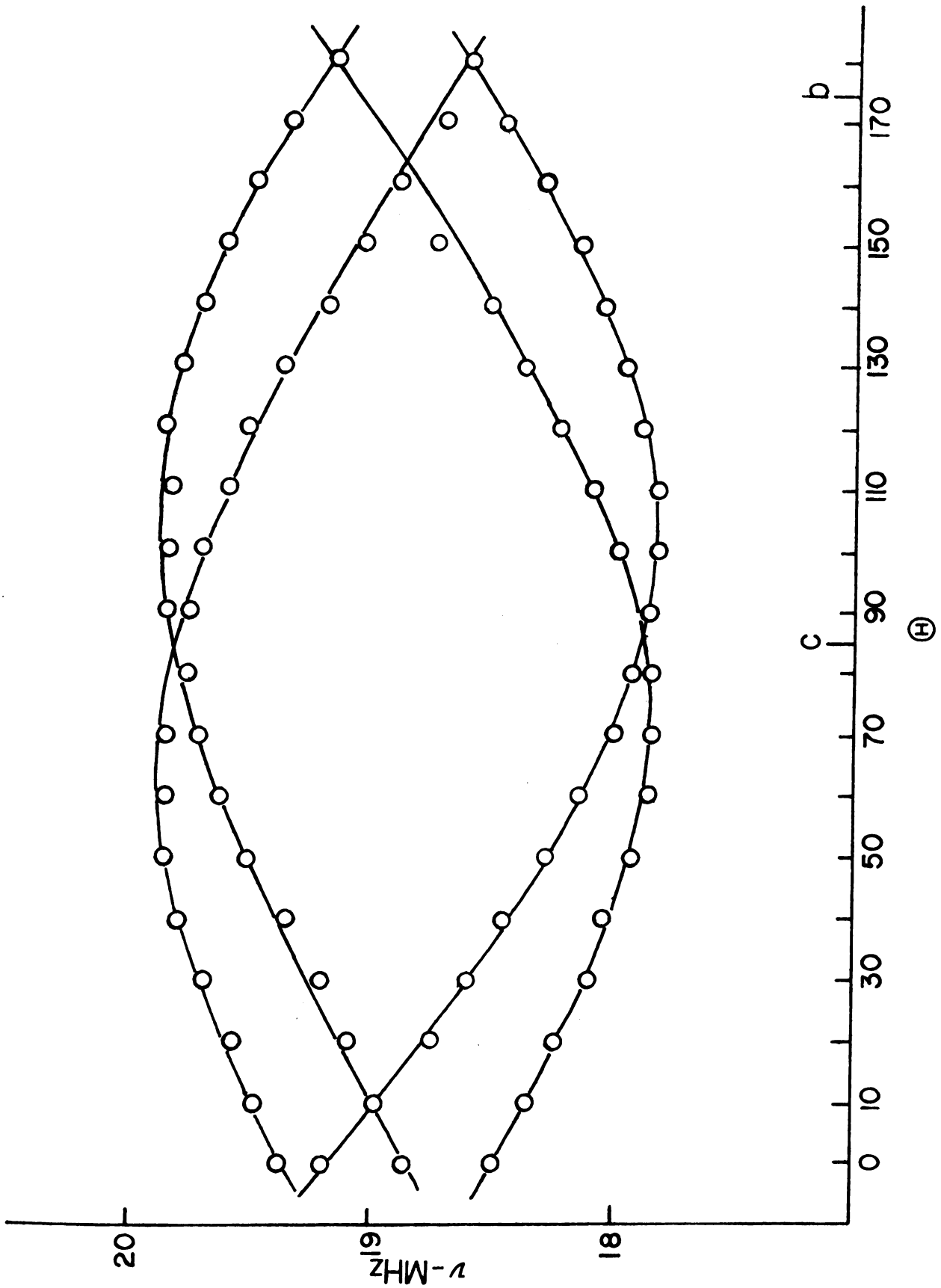
ν-MHz
20
19
18
0
10
30
50
70
90
110
130
150
170
c
b
Θ

state. Rotations were made about each of the three crystallographic axes. A typical rotation diagram is shown in FIGURE 19. Although the frequencies are different for the other lines, the rotational behavior for all lines in applied field is identical. A detailed examination of these rotation diagrams shows that for each local field magnitude, there are four distinct local field directions.

D. Magnetic Susceptibility The near zero field susceptibility for MBTMA has been measured by the group at the University of Illinois at Chicago Circle.[37] The susceptibility and magnetic specific heat data are shown in FIGURES 20 and 21. The data indicate a T_N=1.56K.

The ac susceptibility in applied fields up to 16 kilo-oersted has been measured at liquid He^4 temperatures using standard mutual inductance coils inside a superconducting solenoid.

The data with the external field applied along the crystallographic b axis is shown in FIGURE 22 for several different temperatures. At temperatures below T_N, an anomalous peak at H $\approx$ 1200 oersteds is observed. No such anomaly is observed with the field applied along the other two axes. The values of the critical field and the temperature at the peak in susceptibility are shown in FIGURE 23. This diagram indicates the presence of at least three distinct magnetic phases. Saturation of the

FIGURE 20. Zero field magnetic susceptibility of MBTMA (after J. N. McElearney et al.).

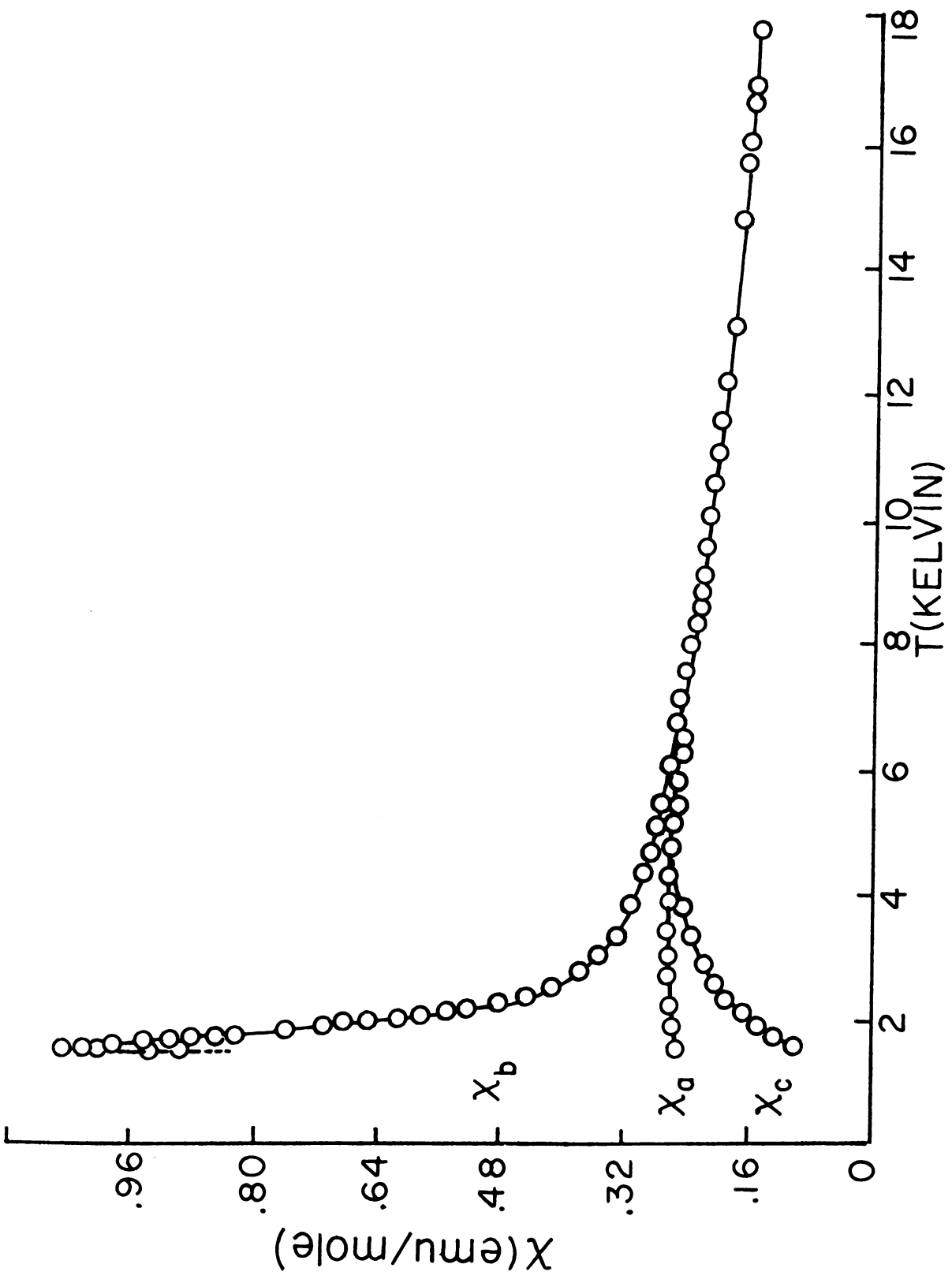
χ (emu/mole)
.96
.80
.64
.48
.32
.16
0
2
4
6
8
10
12
14
16
18
T(KELVIN)
χ_b
χ_a
χ_c

FIGURE 21. Magnetic specific heat of MBTMA (after J. N. McElearney *et al.*).

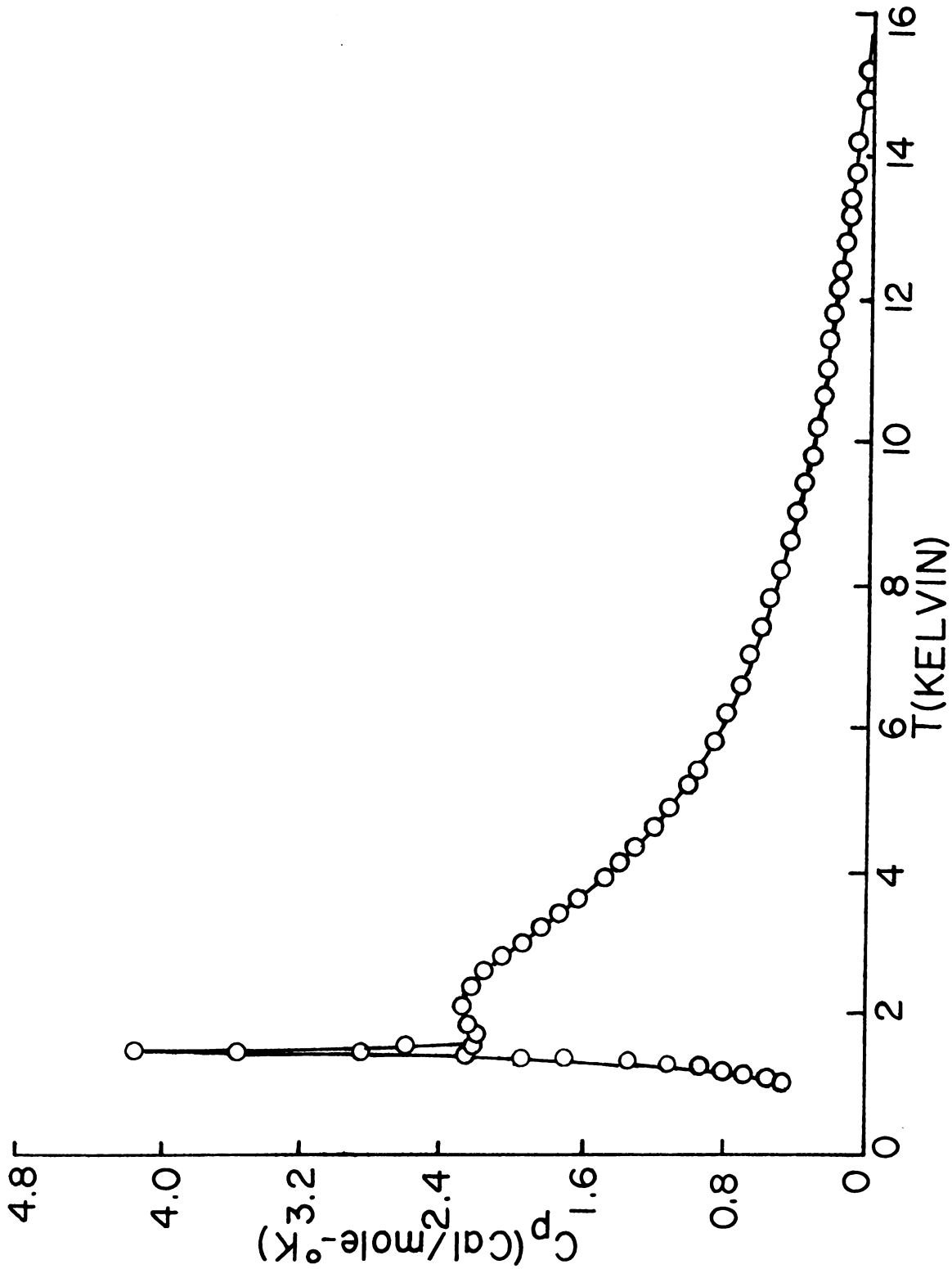
C_p(Cal/mole-°K)
4.8
4.0
3.2
2.4
1.6
0.8
0
0
2
4
6
8
10
12
14
16
T(KELVIN)

FIGURE 22. The magnetic susceptibility of MBTMA with the external magnetic field parallel to the b axis.

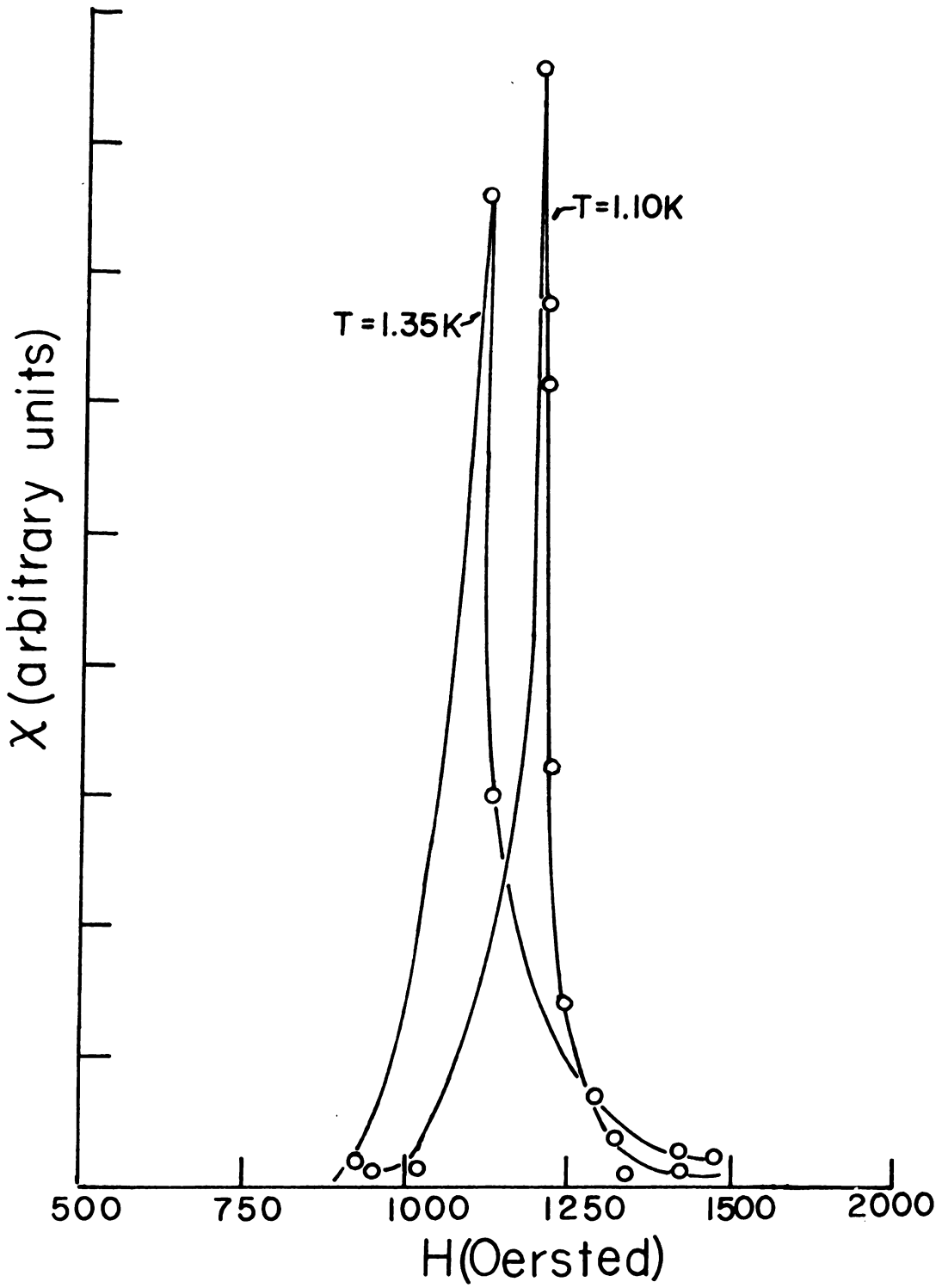
T=1.10K
T=1.35K
χ (arbitrary units)
500
750
1000
1250
1500
2000
H(Oersted)

FIGURE 23. Magnetic phase diagram for MBTMA.

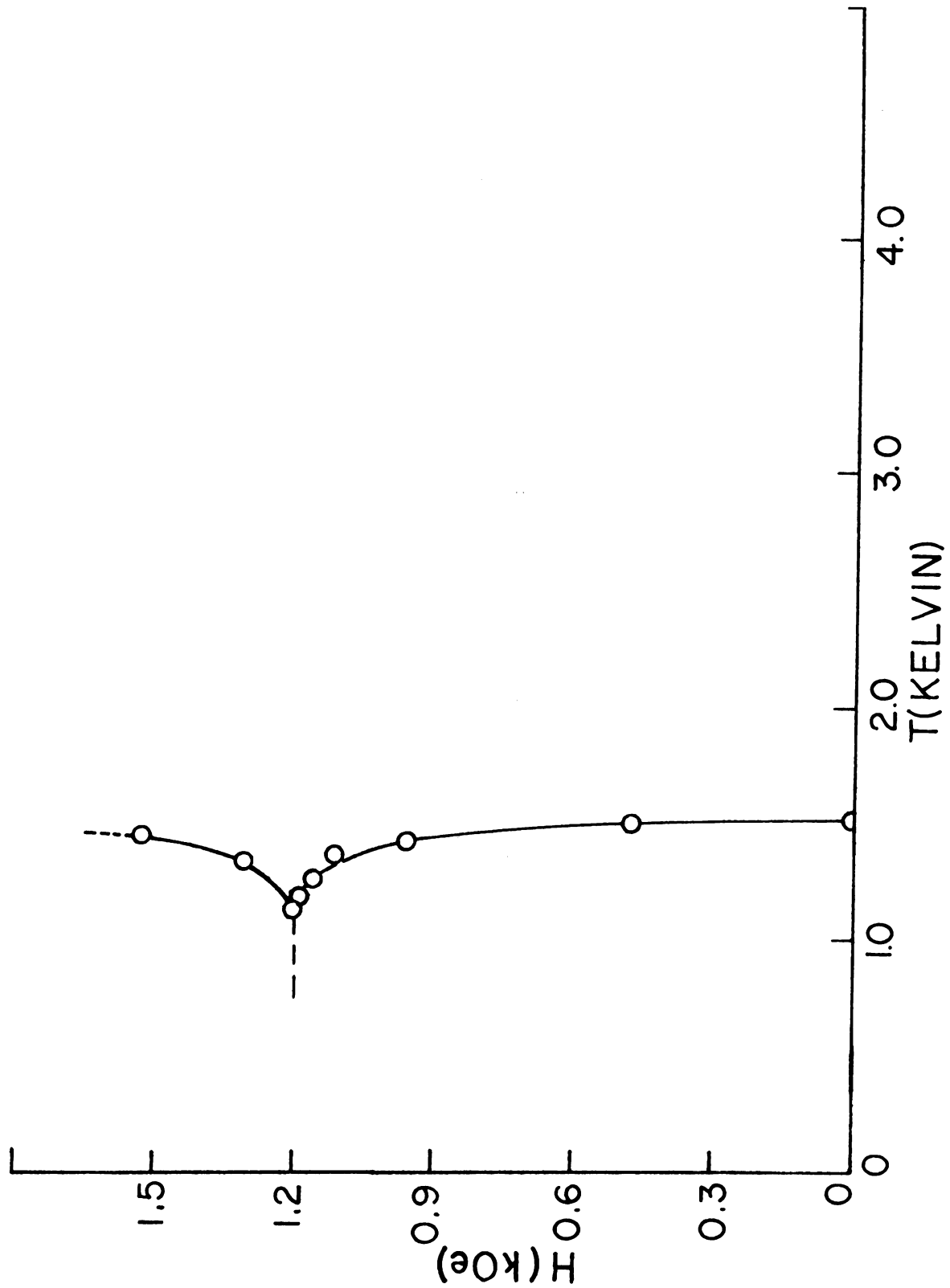
H (kOe)
1.5
1.2
0.9
0.6
0.3
0
0
1.0
2.0
3.0
4.0
T(KELVIN)

spin system was not observed at the highest experimental field. It is possible that another magnetic phase may exist at fields above 16 kOe.

E. Bulk Magnetization The bulk magnetization has been measured as a function of applied field at liquid He^4 temperatures in a "snatch coil" magnetometer (see experimental apparatus: Magnetometer). The magnetization with the field applied along the crystallographic b axis is shown for various temperatures in FIGURE 24. As the temperature is lowered from 4.2k to T_N one observes a linear increase in magnetization for small increasing applied fields. The slope dM/dH is consistent with the measured susceptibility. At temperatures close to T_N, however, an abrupt change in the slope occurs at a field of several hundred oersteds. If one extrapolates the high field portion of the magnetization curve back to zero applied field, one finds a nonzero magnetization whose magnitude increases as temperature is lowered toward T_N. There is no discontinuity in magnetization in the other directions.

At temperatures below T_N, the magnetization in the b-direction shows (FIGURE 25) a sudden increase which occurs at $H \simeq 1200$ Oe. At higher applied external fields the magnetization continues to rise smoothly, although not linearly with increasing applied field. Saturation of the magnetization was not observed for fields up to 16 kOe.

FIGURE 24. Magnetization of MBTMA with the external magnetic field parallel to the b axis.

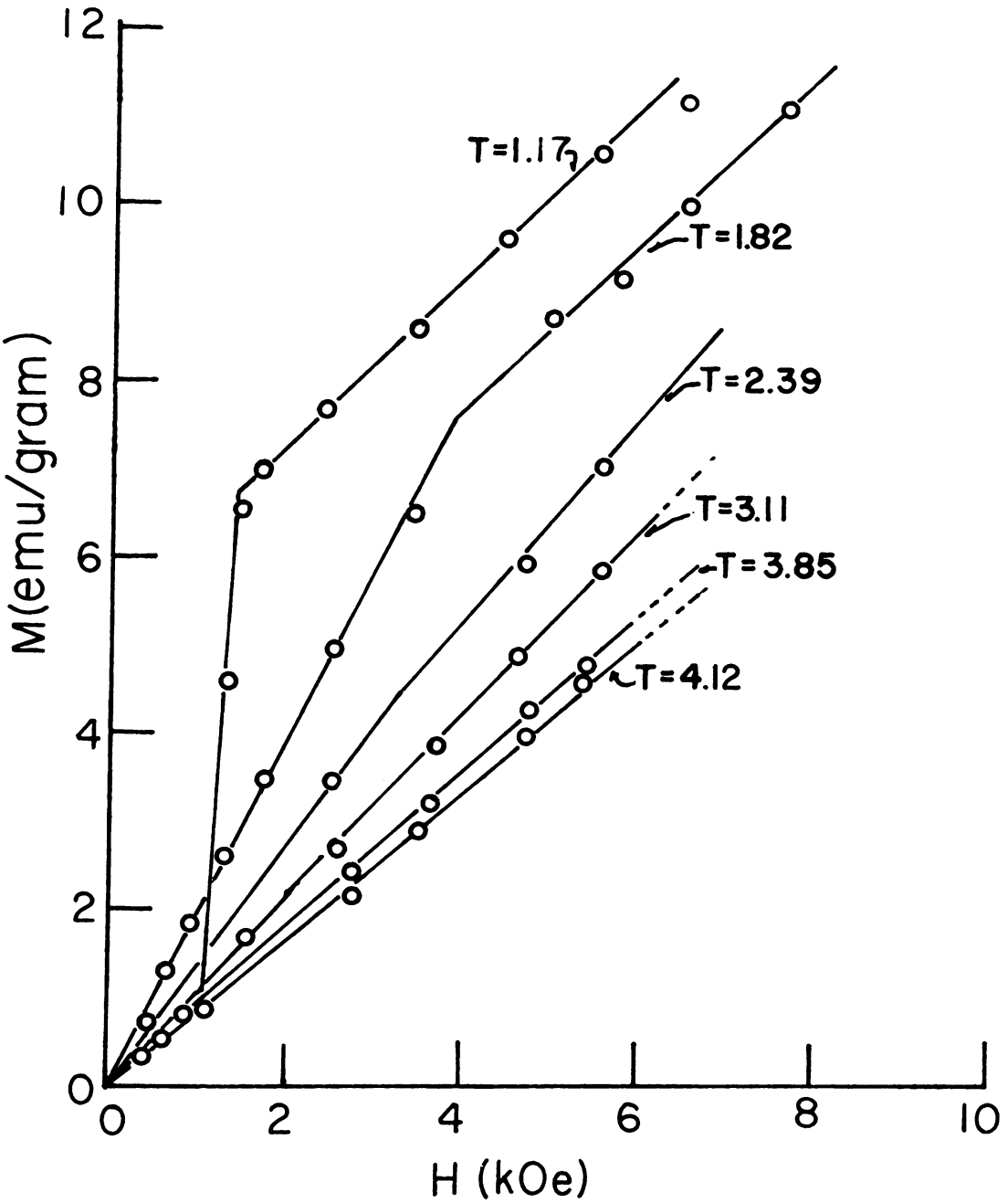
12
10
8
6
4
2
0
M(emu/gram)
T=1.17
T=1.82
T=2.39
T=3.11
T=3.85
T=4.12
0
2
4
6
8
10
H (kOe)

FIGURE 25. Magnetization of MBTMA below T_N (T=1.1K) with the external field along the crystallographic axes.

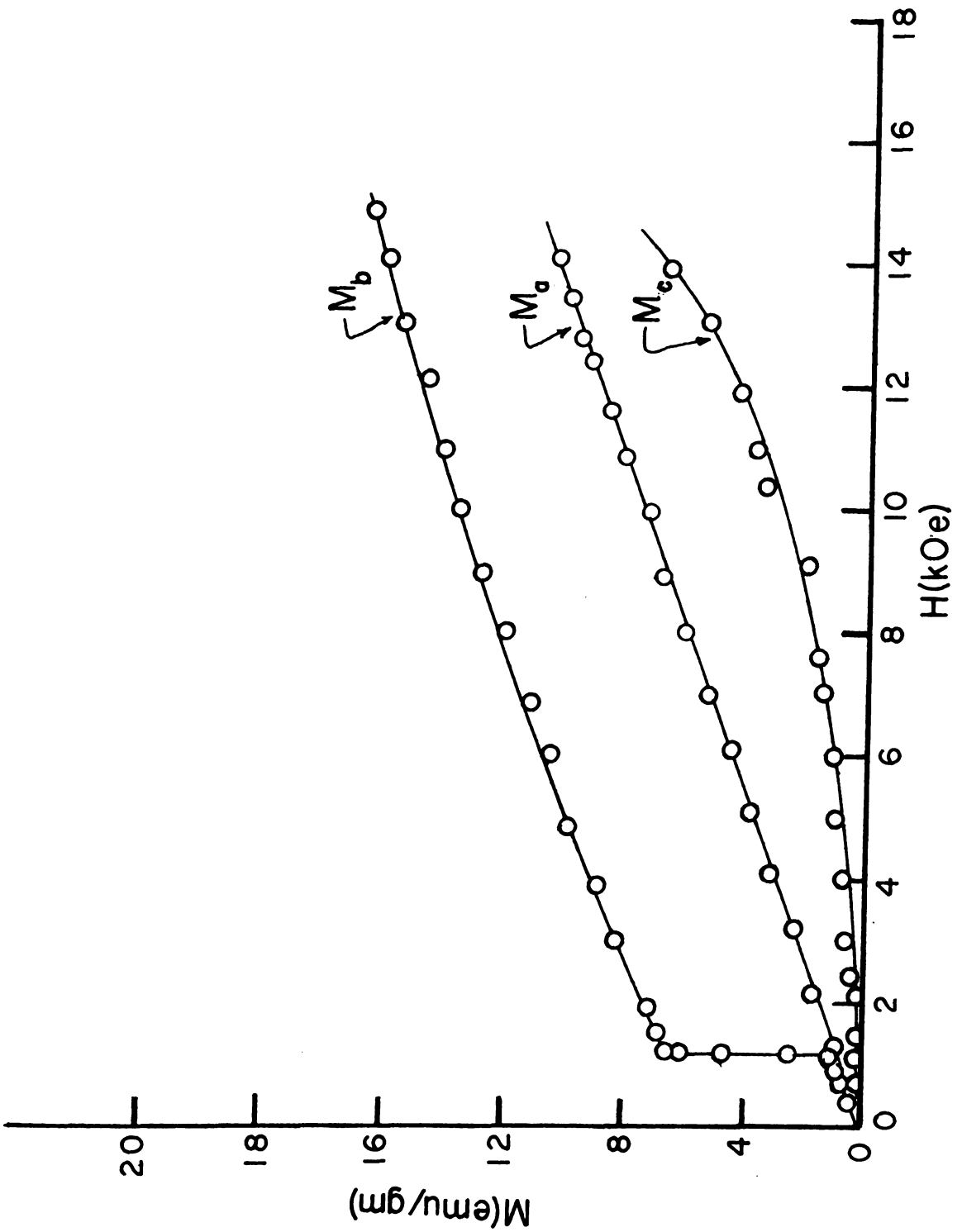
M(emu/gm)
H(kOe)
M_b
M_a
M_c
0
4
8
12
16
18
20
2
6
10
14

III. Discussion

A. Evidence for a Proposed Crystal Structure

The exact crystal structure for MBTMA is at present unknown. It appears likely, however, that the structure is closely related to that of $CoCl_3[(CH_3)_3NH]\cdot 2H_2O$ (CCTMA). The structure of the cobalt complex,[38] shown in FIGURE 26 is characterized by chains of edge sharing octahedra which extend parallel to the b axis. The local coordination of the metal ion is octahedral consisting of four chlorines and two water molecules. The water molecules lie mostly above and below the cobalts in the c direction. The unit cell of CCTMA is orthorhombic with four molecular units in the crystallographic cell.

We assume that in MBTMA, the atomic configuration of the $CoCl_3^-$ and $(CH_3)_3NH^+$ molecular subunits are still preserved, but that a structural modification occurs which affects only the molecular packing of these units. The proposed unit cell modification is exhibited in FIGURE 27.

This change moves the chain running through the center of the CCTMA unit cell down until it coincides with the chains in the ab plane. The cell becomes slightly distorted and descends in symmetry from orthorhombic in CCTMA to monoclinic in MBTMA. The local coordination of the manganese ion is presumed to be octahedral with four bromines and two waters of hydration. The edge sharing character of

FIGURE 26. The crystal structure of cobalt chloride trimethyl amine dihydrate (after D. B. Lossee et al.).

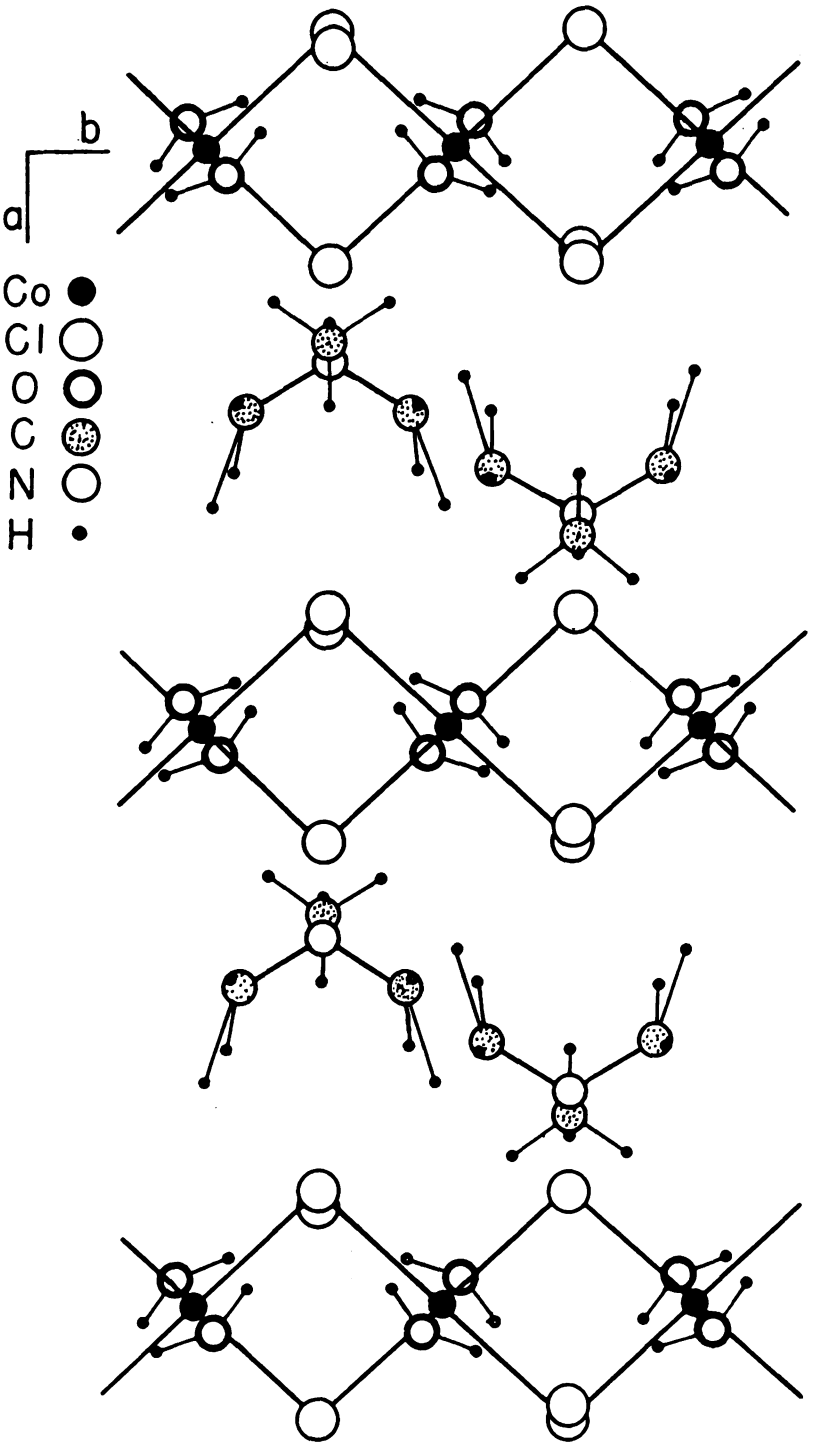
b
a
Co
Cl
O
C
N
H

FIGURE 27. Comparison of the proposed unit cell of MBTMA (lower) with the unit cell of cobalt chloride trimethyl amine dihydrate (upper).

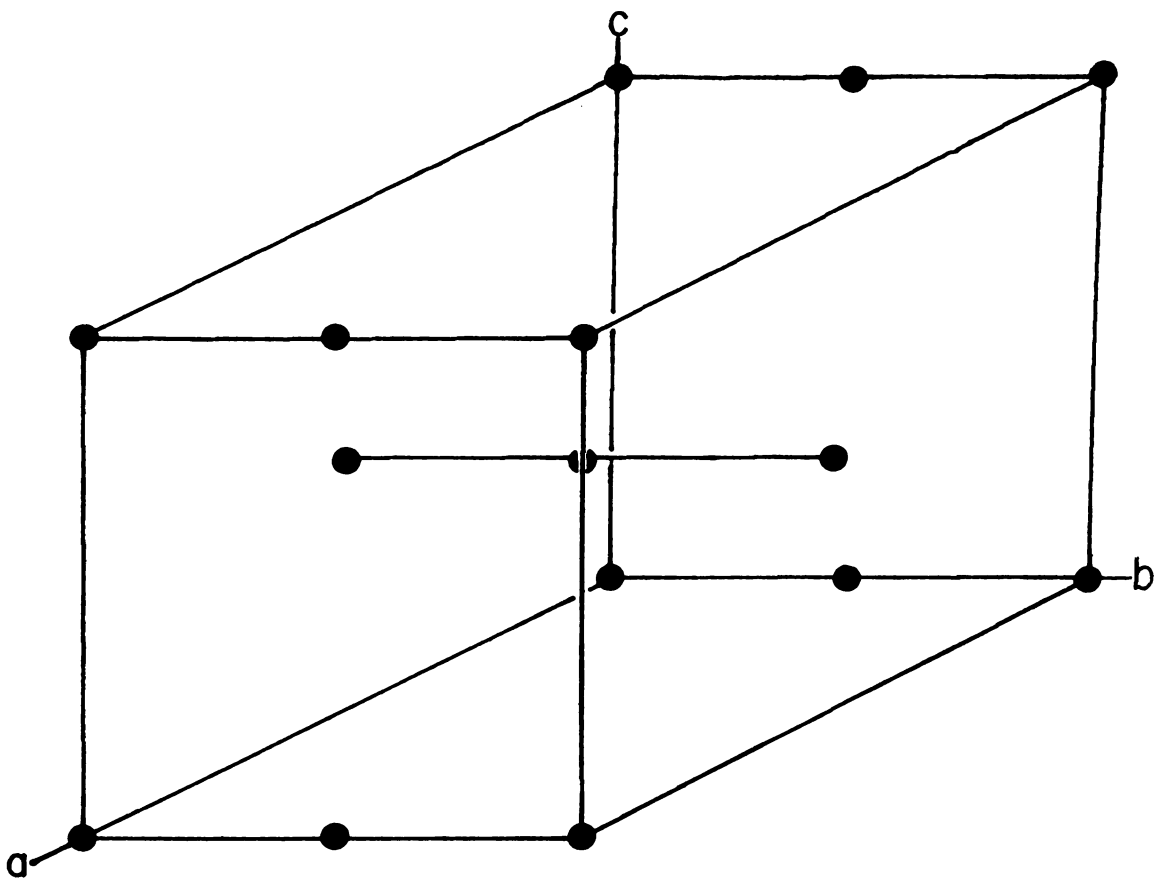
c
b
a

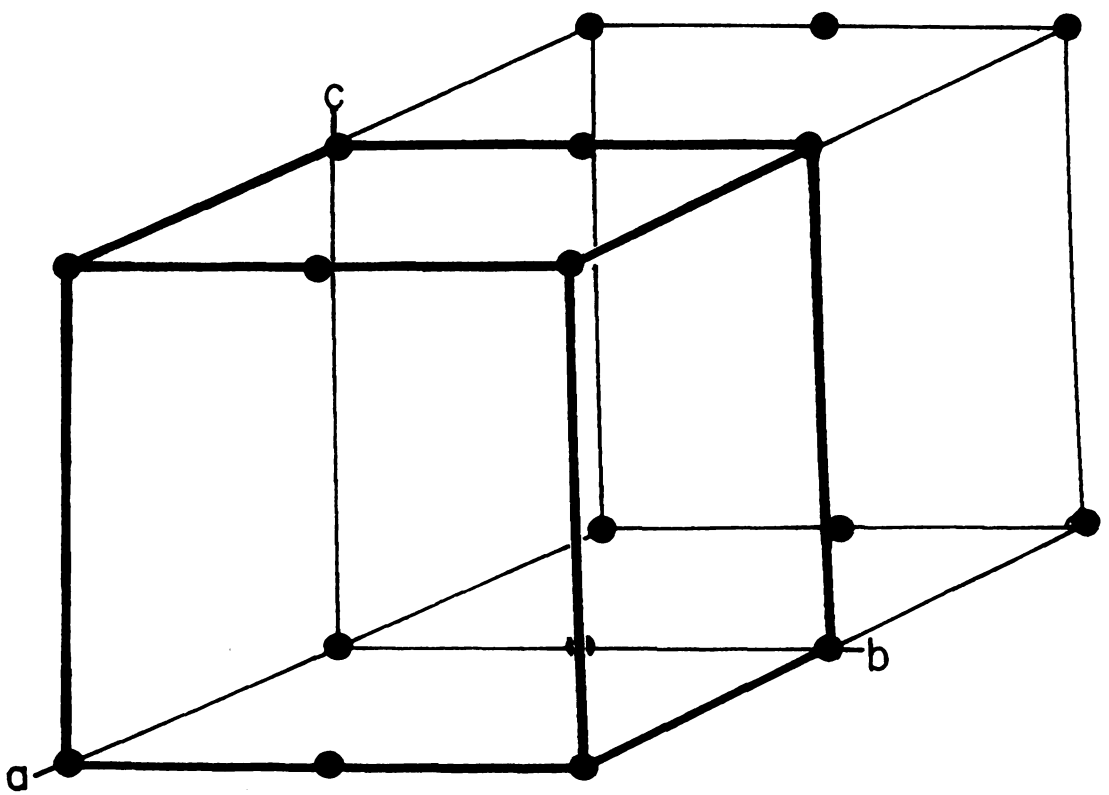
c
b
a

the octahedra in CCTMA which results in a chain of metallo halide bridges is also thought to be present in MBTMA. With the proposed modification of the relative arrangement of these "chains," the length of the a axis in MBTMA should be half that of CCTMA and there will be only two molecular units in the cell. TABLE III is a summary of the crystallographic parameters of both systems. The chemical unit $MnBr_3[(CH_3)_3NH]\cdot 2H_2O$ contains fourteen protons. As there are two molecules in the chemical unit cell, the cell contains a total of 28 protons. Atoms may be located at "general" symmetry positions in the unit cell as follows: place the first atom in the unit cell at some position (X,Y,Z) which is <u>not</u> on a rotation axis, in a mirror plane or at an inversion point. We then perform each of the symmetry operations in the group and generate the remaining general positions. The group $P2_1/m$ has four symmetry operations:"2",mirror, inversion and identity in its point group 2/m. Thus there are four general positions in the crystallographic unit cell which are related by symmetry operations. We could place all twenty eight protons in the MBTMA unit cell in seven groups of four general positions. The four protons in each group are said to be "equivalent." Physically this means that aside from relative differences in orientations produced by the symmetry operations, the local atomic surroundings of each proton would be the same. This last statement implies that

TABLE III

Comparison of unit cell parameters
of MBTMA and CCTMA

	$MnBr_3[(CH_3)_3NH]\cdot 2H_2O$	$CoCl_3[(CH_3)_3NH]\cdot 2H_2O$
Number of molecules in cell	2	4
Lattice dimensions		
a	8.45 ± .02 Å	16.671 Å
b	7.65 ± .02 Å	7.273 Å
c	8.54 ± .02 Å	8.113 Å
	β= 91°56'	

physical properties such as the magnitudes of the local magnetic fields of all four protons in this symmetry related group, would be identical. The fields, of course, will, in general, have four different directions. A different group of four protons which were generated from another "general" starting position (X', Y', Z') need not have the same atomic surroundings or physical properties. Thus, for the seven groups of four protons we would expect seven distinct local field magnitudes. However, the spatial locations of the protons are not all independent. One of the protons, for example, belongs to the amine (NH) unit. Since there are only two such units in the cell, we cannot place these protons (and nitrogens) in general positions which would result in there being four of them in the unit cell. We must then, place them in "special" positions. A special position is a particular location in the unit cell, such as in a mirror plane or at an inversion point. An atom which is placed at one of these positions is unaffected by one or more of the symmetry operations. For example, an atom located in a mirror plane is unaffected by the mirroring operation. There are a total of eighteen methyl (CH_3) protons. Since eighteen is not a multiple of four, a least two and perhaps more of these protons are in special positions. The deuteration experiment shows that there are two distinct local field magnitudes for the water protons. Since there are eight H_2O protons we may place

all of them in general positions producing the requisite two groups of four. TABLE IV shows a possible assignment of special and general positions and the resulting number of local field magnitudes. This assignment produces nine local field magnitudes which is consistent with the number of zero field proton resonances. Finally, because the cell only contains two manganese ions, these also must be in special positions.

Let us elaborate on the reasoning for the assertion that the local coordination of the metal ion is similar in both MBTMA and CCTMA. The broad peak in the magnetic specific heat data above T_N for both systems indicates low dimensional magnetic behavior. This behavior, which is thought to be due to short range correlations, is also evident in the nonzero (extrapolated) moment observed in the bulk magnetization measurements above T_N. This supports the assertion that chains of metal halide bridges are present in both MBTMA and CCTMA. The water molecule which completes the octahedral local coordination of the metal ion in the cobalt salt appears to have the same location in MBTMA. Evidence for the location of the waters of hydration is provided by the zero field susceptibility and NMR below T_N. The zero field susceptibility data along the c axis has the smallest value at the lowest experimental temperature. We infer this axis behaves much

TABLE IV

Assignment of proton special positions in MBTMA

Chemical unit	Number in General positions (4 operations)	Number in Special Positions (2 operations)	Number of Distinct Proton Local Field Magnitudes
CH_3	12	6	3+3 = 6
NH	0	2	0+1 = 1
H_2O	8	0	2+1 = 2
			9

like the parallel axis in a uniaxial antiferromagnet. The spins in MBTMA then are mostly along the c axis. If we assume the waters of hydration which complete the octahedra are located above and below the manganese ion along the c direction, we can calculate the local field at the protons due to the manganese moment. A typical configuration for a water molecule bonded to a manganese ion is shown in FIGURE 28.

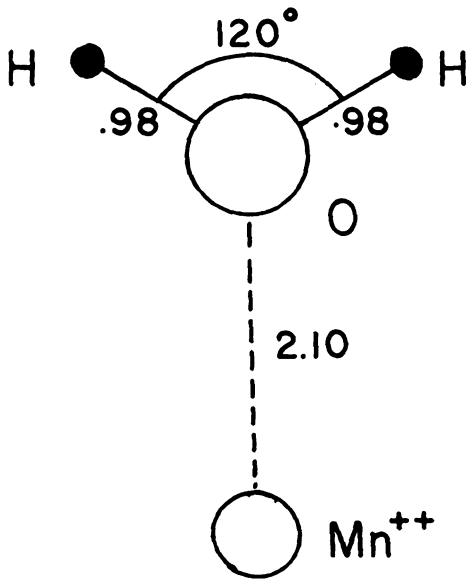

FIGURE 28. Bonding of a water molecule to a manganese ion.

The magnetic dipole field at a distance "r" from the manganese is given by:

$$\vec{\beta} = \frac{3\hat{n}(\vec{\mu}\cdot\vec{\mu})-\vec{\mu}}{r^3} \qquad (64)$$

where $\hat{n}$ is a unit vector which points along r and $\vec{\mu}$ is the manganese magnetic moment:

$$\vec{\mu} = \mu_B \vec{\vec{g}}\cdot\vec{S} \qquad (65)$$

If we assume the magnanese moment points along the line joining the manganese and the oxygen, we calculate that the magnetic field at the water proton is 4425 oersteds. The nuclear magnetic resonance frequency for a proton in a field of this magnitude is 18.84 MHz. The apparent excellent agreement of the calculated frequency with our experimental values of 18.17 and 18.74 MHz is somewhat fortuitous since this calculation used only one manganese ion, while the real field is due to all spins in the lattice. A dipole sum was carried out using our proposed crystallographic lattice with the spins coordinated antiferromagnetically along the chains with the moments in the + and - c directions as shown in FIGURE 29. The sums were calculated by computer over the volume of a sphere which contained 6800 manganese spins. The result gave a field of 4354 oersteds or a nuclear magnetic resonance frequency of 18.54 MHz. The magnetic moment used in this calculation is based on a

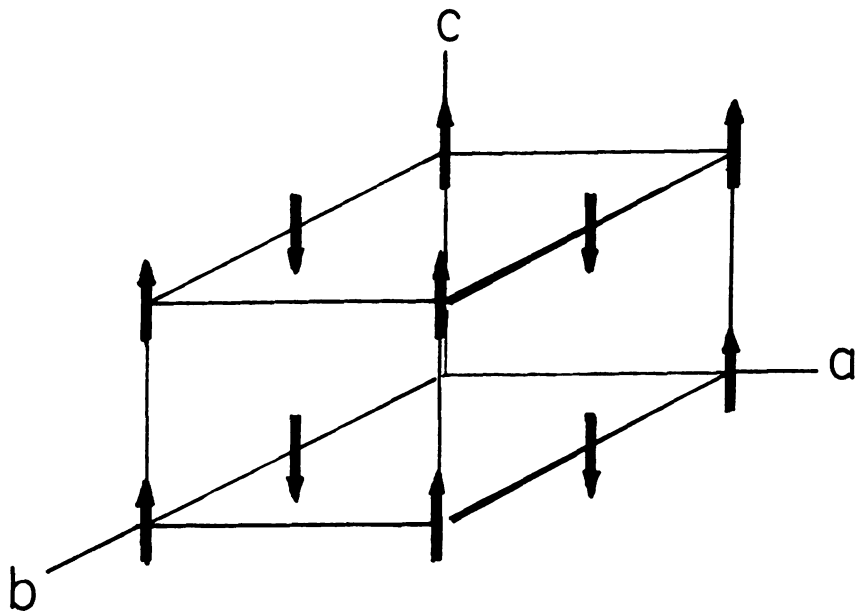

FIGURE 29. Magnetic dipole arrangement used in computer calculation.

spin of S=5/2 and the g-value of 2.12 which was derived from the ESR data. Let us next consider, at least qualitatively, the details of the interactions which determine the spin state of Mn^{++} in MBTMA.

B. Magnetism of $3d^5$ S=5/2

Doubly ionized manganese is a transition metal ion with a $3d^5$ orbital configuration. As previously indicated it is likely that the local coordination in MBTMA is octahedral. In octahedral symmetry the five d orbitals are split by the crystalline electric field interactions as shown in FIGURE 12. If the energy separation "Δ" between the t_{2g} and e_g states is not large (the "weak ligand field" limit), the minimum energy configuration is achieved by singly occupying each orbital. Each of the five d electrons are coupled "spin up" resulting in the maximum spin angular momentum, S=5/2. The fact that all the spins are parallel requires that the orbital angular momentum be $\vec{L}=0$; an "S"-state configuration. This zero net angular momentum will cause all matrix elements involving $\vec{L}$ (in particular $\vec{H}\cdot\vec{L}$ and $\vec{L}\cdot\vec{S}$) to vanish in first order. Since as we have shown earlier these matrix elements are responsible for the deviation of the g-value from 2, manganese with S=5/2 should have a g equal to 2. In addition, one would not expect any crystalline electric field splitting of the $\pm 5/2$, $\pm 3/2$ and $\pm 1/2$ Kramer's doublets. There are however, excited configurations of the d orbitals which are produced by doubly occupying one of the orbitals. The resulting S=3/2 system will have a nonzero orbital angular momentum. However, because of the resulting large

electron-electron repulsion produced by the double occupancy of one of the orbitals, matrix elements calculated in second order between the ground ($\vec{L}=0$) state and this excited state are reduced by the large energy difference which appears in the denominator. Experimentally, one normally finds the g value very nearly 2 for S=5/2 manganese in octahedral coordination.

MBTMA, for example, has a g value of 2.12±.02 which is isotropic within experimental (E.S.R.) resolution. Only one resonance line with a width of approximately 2 kilo-oersteds was observed. This width is quite usual for manganese which in addition to having an electron spin of S=5/2, has a nuclear spin of I=5/2. Each of the six (2S+1) spin states is split by the hyperfine interaction into six (2I+1) components giving a total of 36 levels! In a concentrated magnetic system such as MBTMA, spin-spin interactions broaden the individual levels so that the resonance line would appear as one broad signal. The fact that only one such broad resonance is observed, indicates the three Kramer's doublets (S= 5/2, ±3/2, ±1/2) are only slightly split by the crystal field. This again is consistent with a small spin orbit coupling due to the $\vec{L}=0$ (S-state) orbital ground state.

C. The Ordered State: Metamagnetism

As previously discussed, the zero field susceptibility data indicates the sublattice magnetization in MBTMA is mostly along the c axis. The large peak in the b axis susceptibility data and the nonzero extrapolated moment above T_N, are both consistent with the formation of a net moment produced by canting the spins. The magnetic phase transition which is observed below T_N occurs with H applied along the b axis. This implies the transition which is observed is not a spin flop, which occurs with H parallel to the sublattice magnetization but is more likely a metamagnetic transition. If the ordered state consisted of a uniaxial antiferromagnetic system, one would observe a spin flop only with the field applied along the direction of sublattice magnetization. If the sublattices are canted, the zero field susceptibility data along each of the three axes behaves differently whereas a uniaxial system would be characterized by a parallel and a perpendicular susceptibility. The facts that the magnetization in small applied fields vanishes smoothly for decreasing fields and that there were no discontinuities in the NMR rotation patterns in applied field imply that the total spin configuration in the ordered state has no net moment.

The observations that MBTMA: (1) has a magnetic transition in applied field which appears to be metamagnetic; (2) exhibits four distinct local field directions

for all proton lines; (3) has an antiferromagnetic unit cell, suggest the following model. We postulate that the system behaves as a four sublattice canted antiferromagnet, with the following zero temperature sublattice Hamiltonian:

$$H = -\Gamma\vec{H}\cdot\Sigma\vec{S}_i - k\Sigma S_{i\xi_i}^2 - J_{AF}^{\circ}(\vec{S}_1\cdot\vec{S}_4 + \vec{S}_2\cdot\vec{S}_3)$$
$$-J_{AF}^{1}(\vec{S}_1\vec{S}_3 + \vec{S}_2\vec{S}_4) \qquad (66)$$

with $k \gtrsim |J_{AF}^{\circ}| > |J_{AF}^{1}|$ and J_{AF}°, J_{AF}^{1} both negative and where ξ_i represents an anisotropy axis whose direction is different for each sublattice but are related by symmetry. Here again, the S's represent sublattices. The model is shown with the interactions indicated in FIGURE 30a. The sublattices are mostly along the + and - c directions and are canted in the + and - b directions. The magnetic transition is presumed to be metamagnetic and results in the spin configuration shown in FIGURE 30b. The canting angle θ may be calculated from

$$\Delta M = Ng\,\mu_B\,S\sin\theta \qquad (67)$$

where ΔM is the field induced change in magnetization at the phase transition. Using the observed value of 1.91×10^3 emu/mole we deduce a canting angle of approximately 4°. We shall qualitatively discuss the behavior of the system in an applied field by using the previously derived sublattice polarization energy diagrams (PED).

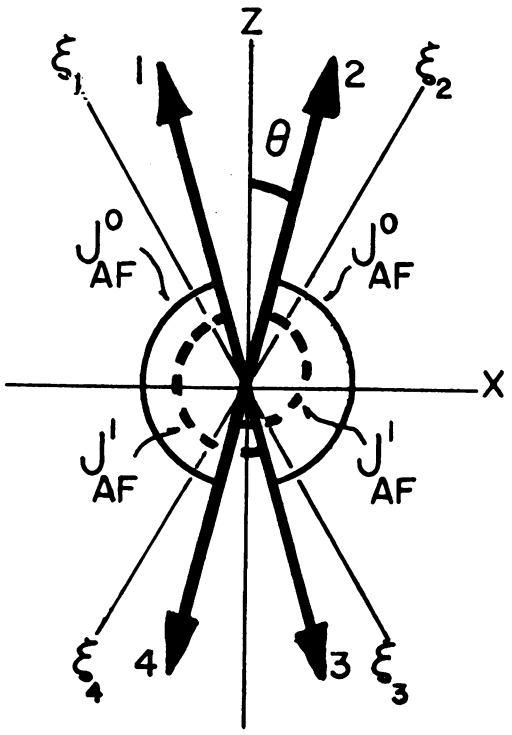

FIGURE 30a. Zero temperature sublattice model for MBTMA with H=0.

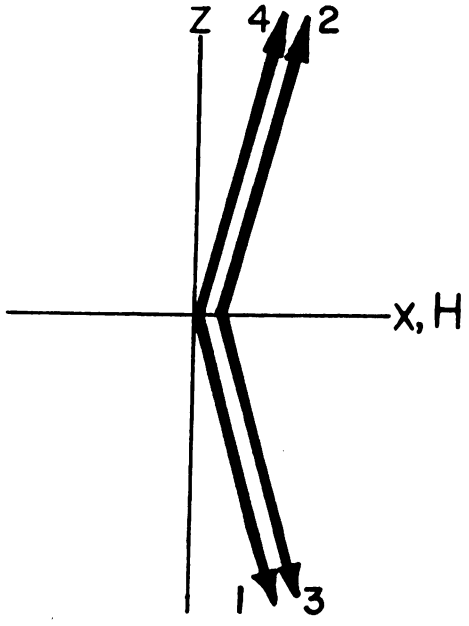

FIGURE 30b. Zero temperature sublattice model for MBTMA with $H \geq H_{CRIT}$

We shall take as our polarization basis states the following:

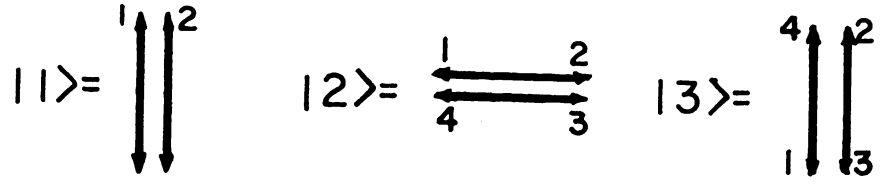

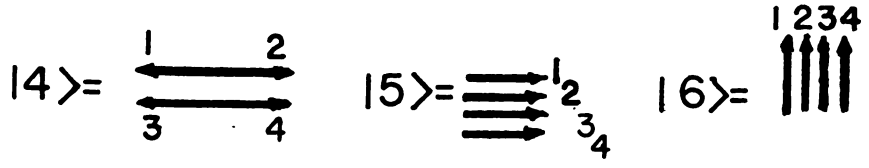

In zero applied field, these polarization states are mixed by the competition between the anisotropy and the antiferromagnetic exchange, to form the following states:

$$\Phi_1 = a|1\rangle + b|2\rangle =$$ 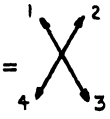

(68a)

$$\phi_2 = c|3\rangle + d|4\rangle$$ 

(68b)

The polarization state ϕ_2 is higher in energy in zero field because of the exchange energy J_{AF}^{1}. Let us consider first the behavior of this system with a field applied along the x(b) axis.

FIGURE 31. PED for manganese MBTMA with H along the b axis.

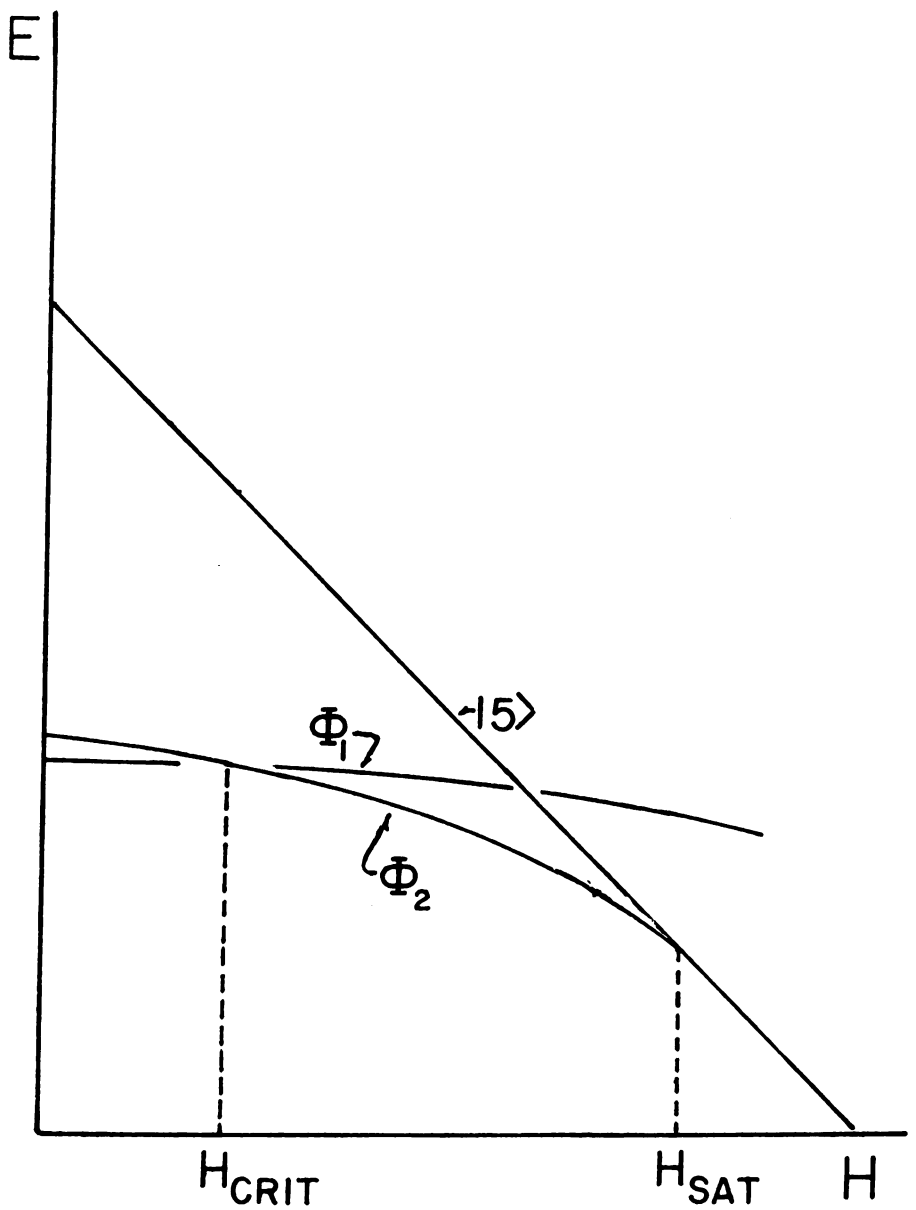
E
|15>
Φ_{17}
Φ_2
H_{CRIT}
H_{SAT}
H

The applied field couples some of the state $|4\rangle$ into ϕ_1. This produces a net moment so that the energy of the state decreases because of the Zeeman interaction. The state ϕ_2 has a larger moment than ϕ_1, so that it descends in energy faster than ϕ_1 as shown in FIGURE 31. For $H < H_{crit}$, the system is polarized mostly along + and - z but is canted in the + and - x directions. As the field is increased, the sublattices rotate towards the field. At $H = H_{crit}$ sublattices 1 and 4 reverse their direction so that they coincide with 3 and 2 respectively. This results in an abrupt increase in the magnetic moment. The moment then continues to increase until $H = H_{SAT}$.

With the magnetic field applied along the z(c) axis we must consider a new mixed polarization state.

$$\phi_3 = e|4\rangle + f|6\rangle = \quad (69)$$

Again the state ϕ_1 is lowest in zero applied field. The state ϕ_3 is significantly higher in energy than ϕ_2 because of the assumption $J_{AF}^{\circ} > J_{AF}^{1}$. The applied field mixes some of the ferromagnetic polarization $|6\rangle$ with ϕ_1. This causes the energy of ϕ_1 to decrease because of the Zeeman interaction. The state ϕ_3 has a large moment and descends rapidly in energy with increasing applied field. The PED for this situation is shown in FIGURE 32.

FIGURE 32. PED for MBTMA with H along the c axis.

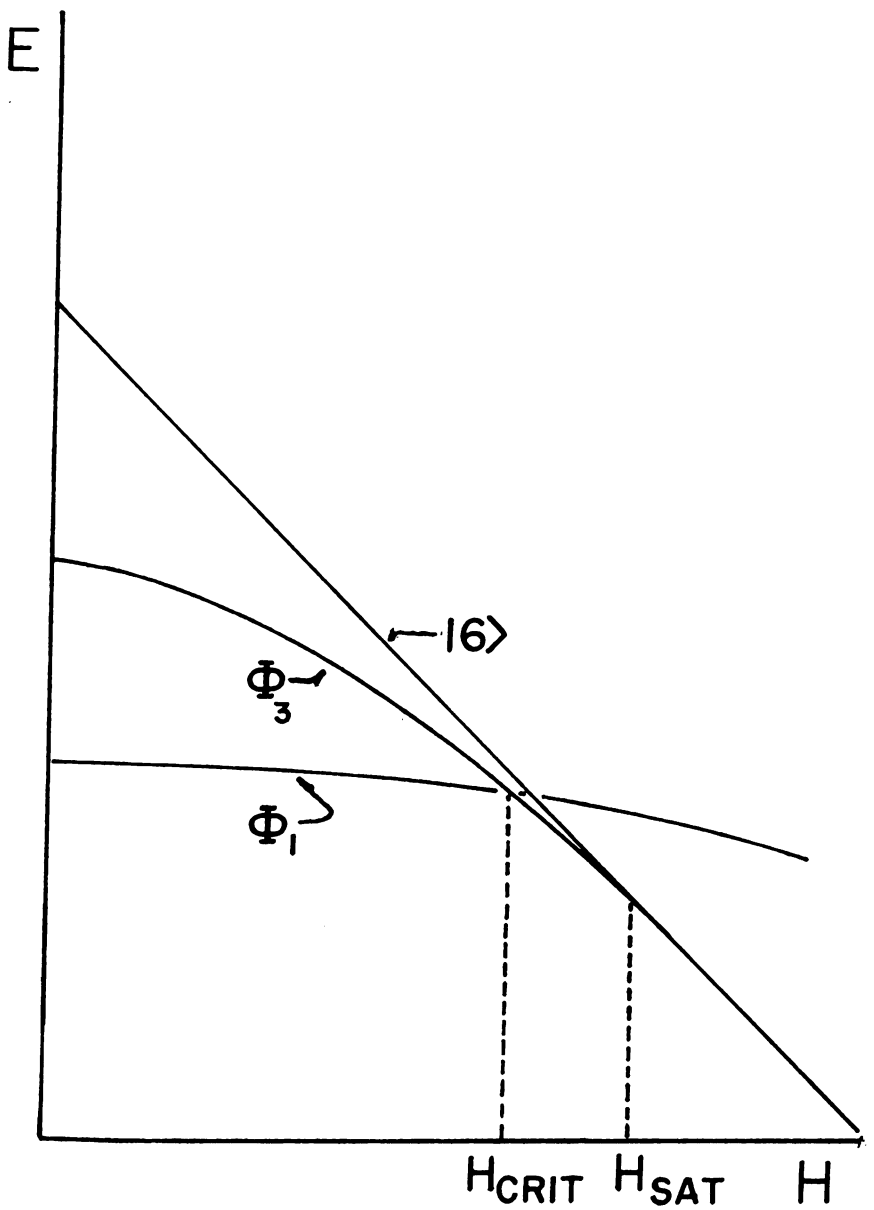
E
|16>
Φ_3
Φ_1
H_{CRIT}
H_{SAT}
H

For $H < H_{crit}$, the spins rotate toward the field. The critical field with H_{app} along the z axis is higher than H_{crit} along the x axis again because of the assumption $J_{AF}^{\circ} > J_{AF}^{1}$. This presumably raises the critical field, with H_{app} along z(c), beyond the highest experimental field of 16 kOe. and therefore it was unobserved. At the critical field, sublattices 3 and 4 reverse and become colinear with sublattices 1 and 2 respectively. This again results in an abrupt increase in magnetization. The moment continues to grow until $H = H_{sat}$. Finally, a field applied along y, rotates all spins toward the field until $H = H_{sat}$. No sharp transition is observed.

Let us examine the implications of this model for the magnetic space group.

D. The Ordered State: The Magnetic Space Group

X-ray studies and optical goniometry show the chemical space group is $P2_1/m$ with the two fold screw axis parallel to the crystallographic b-axis. The magnetic space group may be formed by taking some or all of the elements of the crystallographic group and replacing these elements with anti elements. All of the magnetic space groups which result[39] from $P2_1/m$ are listed in TABLE V. Each of these groups is derived from the point group 2/m. Each group contains four symmetry operations. Except for

TABLE V

Magnetic space groups resulting from $P2_1/m$

Group	Ferromagnetic	Antiinversion	Antitranslation
$P2_1/m$	Yes	No	No
$P2_1'/m$	No	Yes	No
$P2_1/m'$	No	Yes	No
$P2_1'/m'$	Yes	No	No
$P_{2c}\ 2_1/m'$	No	Yes	Yes
$P_{2s}\ 2_1/m$	No	No	Yes

the last two groups which contain eight. If we assume the magnetic spins are confined to one plane and canted along the two fold axis (the b-c plane in the crystal) the number of distinct spin directions within the magnetic unit cell produced by each point group is shown in FIGURE 33.

We recall there are only two manganese ions in the chemical unit cell. Therefore, they must be located in special positions. The special positions for the crystallographic space group $P2_1/m$ occur with the atom located at inversion centers or on the mirror plane. In Section IV of the theory, SYMMETRY AND THE MAGNETIC SPACE GROUP, we tabulated the restrictions placed on the orientation of a spin if it occupies a special position in the magnetic unit cell. To reiterate: a magnetic ion cannot be located on an antiinversion center and a spin which is in a mirror plane must be perpendicular to the mirror plane if it is real or must lie in the plane if it is an anti mirror plane. The mirror planes in MBTMA are perpendicular to the b (the two fold) axis. Our proposed model for the spin arrangement has the spins along + and - c and canted in the + and - b directions. This canting is not allowed if the spins are located in either a mirror plane or antimirror plane. Therefore, the spins must occupy the only remaining special position, an inversion center.

FIGURE 33. The magnetic point groups formed from 2/m.

Our proposed spin model also requires a total of four unique directions in the magnetic unit cell. The point groups 2/m and $2'/m'$, which both contain inversion centers, result in only two distinct directions. As previously indicated, antitranslation will reverse the spin orientations in alternate crystallographic unit cells. Antitranslation will then produce a total of four unique directions if added to the groups 2/m and $2'/m'$ resulting in the groups $2/m1'$ and $2'/m1'$. The groups $2/m'$ and $2'/m$ do not contain inversion centers and do result in four unique directions in the unit cell. The requirement of four unique spin orientations in the unit cell is met by a group which contains <u>both</u> inversion and antitranslation or <u>neither</u> operation.[40] This requirement is satisfied by the groups

$$2/m' \qquad 2'/m \qquad 2/m'1' \quad \text{and} \quad 2/m1'$$

The first three groups contain antiinversion centers. If the manganese ion is located on an inversion center in the crystallographic unit cell, the corresponding magnetic unit cell must not contain antiinversion centers. Therefore, if the manganese is on an inversion center, the correct point group is $2/m1'$ which results in the magnetic space group $P_{2_S}2_1/m$. The subscript 2s indicates the magnetic unit cell is doubled along some direction perpendicular to b, relative to the crystallographic

unit cell. Determination of the direction in which the unit cell doubles requires further experimental evidence.

CHAPTER 4

COPPER L-ISOLEUCINE MONOHYDRATE

I. Introduction

Bis L-Isoleucinato copper (11) monohydrate. $C_{12}H_{24}CuN_2O_4 \cdot H_2O$, the copper (II) complex of the amino acid L-Isoleucine, (hereafter referred to as copper L-Isoleucine) is an example of a five-coordinated transition element ion in which the local coordination forms a square pyramid. Although there have been extensive spectroscopic investigations of[41-45] similar systems and some magnetic measurements,[46-47] there have been few reports of the low temperature behavior of five-coordinated systems.[48] We shall present and discuss the magnetic susceptibility in near zero and applied fields and electron spin resonance (ESR) spectra of powder and single crystal samples of Cu^{2+} L-Isoleucine monohydrate.

The crystal structure is orthorhombic with four chemical units in the crystallographic unit cell. The unit cell dimensions are a=9.451Å b=21.67Å c=7.629Å and the reported space group is $P2_12_12_1$.[49] The copper atom lies approximately in the center of the base of a square pyramid. Two oxygens and two nitrogens form the base of the pyramid

FIGURE 34. The square pyramidal coordination of copper L-Isoleucine showing the derived principal axes of the g tensor.

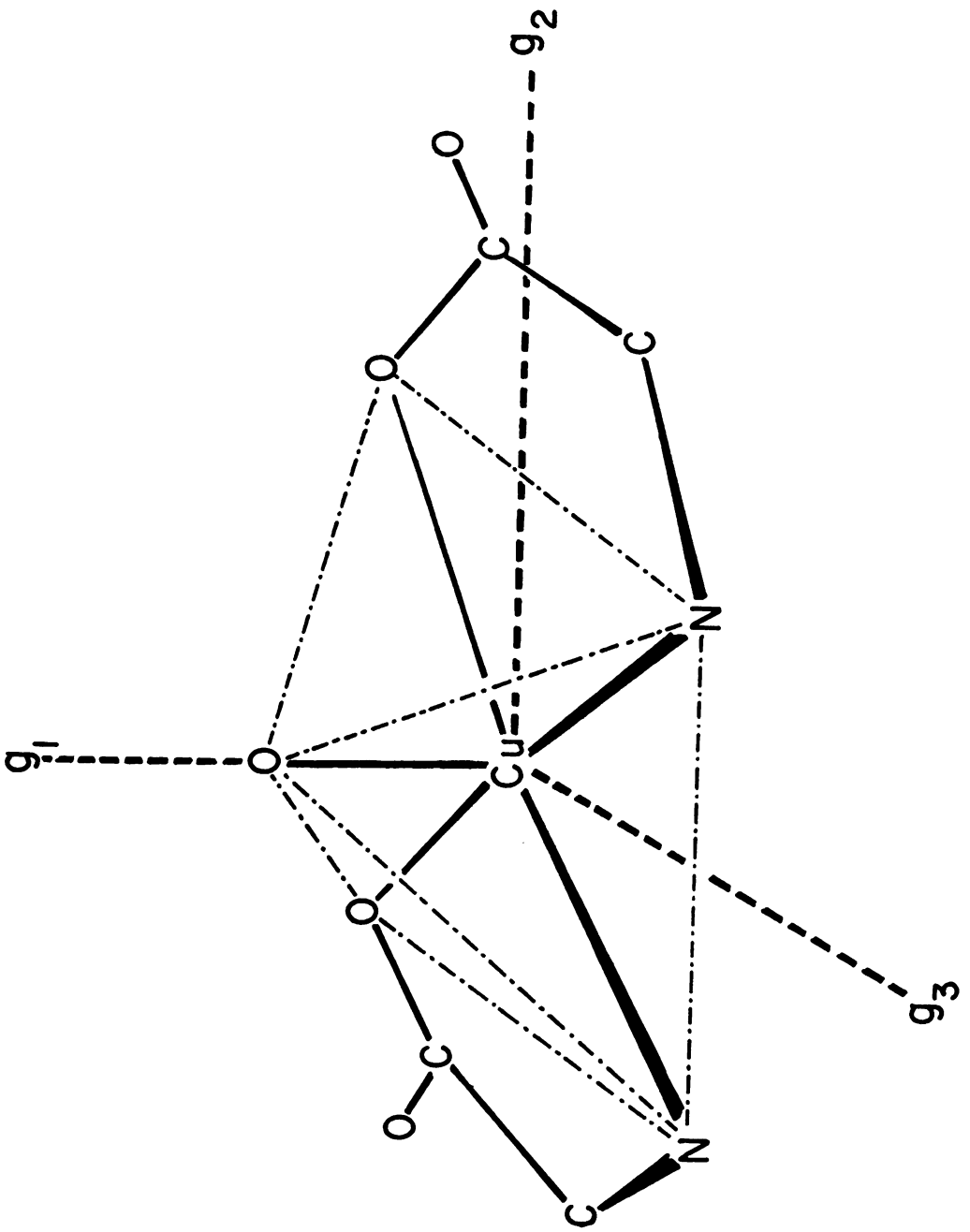
g2
O
C
O
C
N
g1
O
Cu
O
g3
C
O
N
C

FIGURE 35. The crystal structure of copper L-Isoleucine (after Weeks *et al.*).

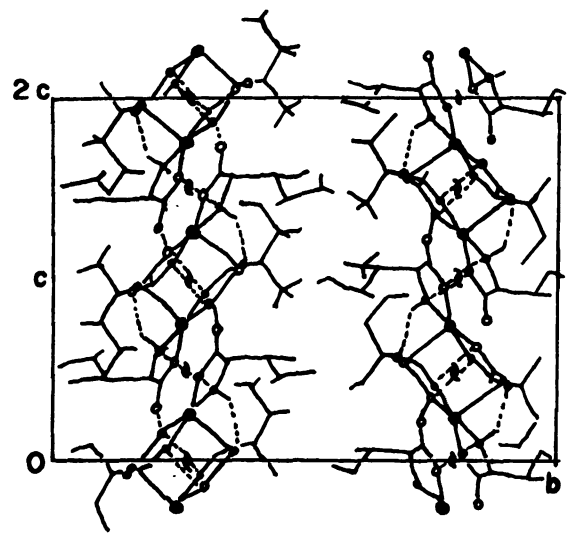

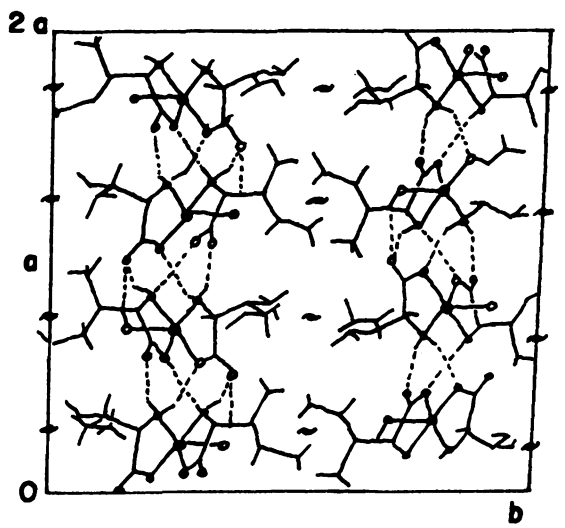

● Cu ·N ·O -----hydrogen bond

and a water oxygen completes the top of the pyramid (FIGURE 34). The symmetry of this configuration is $4mm(C_{4v})$.

The molecules are "hydrogen-bonded" along the a and c axes, but are well isolated in the b-direction. (See FIGURE 35.) These structures will be referred to as "sheets" in the ac plane but in fact the copper L-Isoleucine molecules are indeed three dimensional; it is only the bonding which is two-dimensional. This two-dimensional character suggests the possibility of two-dimensional magnetic behavior.

II. Experimental

Copper L-Isoleucine monohydrate, $C_{12}H_{24}CuN_2O_4 \cdot H_2O$ was prepared by reacting basic copper carbonate ($CuCO_3 \cdot Cu(OH)_2$), with L-Isoleucine, ($CH_3CH_2CH(CH_3)CH(NH_2)(OOH)$),in water. The resulting dark blue solution was filtered and slowly evaporated near room temperature. The complex crystallized in thin deep blue diamond shaped platelets (FIGURE 36). The largest single crystals had a mass of 15 milligrams. The crystals were oriented for the various single crystal experiments by using the external morphology after comparing the morphology with the known lattice parameters using X-ray diffractometry.

Since, as will be shown, the magnetic susceptibility results indicate the possibility of nonstoichiometric

FIGURE 36. The morphology of copper L-Isoleucine.

copper, the copper content was determined by neutron activation analysis of a 35.6 milligram powder sample. The sample was irradiated at the M.S.U. "TRIGA" nuclear reactor. There are two naturally occurring isotopes of copper: Cu^{63} (70%) and Cu^{65}(30%). The analysis was performed on the 1.348 MeV gamma ray of the Cu^{64} isotope which results from neutron capture by Cu^{63}. The half-life of Cu^{64} is 12.75 hours, which was sufficiently long to enable accurate counting without a significant correction for half-life. By comparing the activity of the sample of copper L-Isoleucine with a standard containing a known amount of copper, the content in the copper L-Isoleucine could be established. The results indicated there were 6.8 mg of copper in a 35.6 mg sample of copper L-Isoleucine, or a mass concentration of 19±2%. The theoretical concentration of copper in the Isoleucine complex is 18.6%, so that to within the accuracy of the analysis, there is no uncombined copper.

A. Magnetic Susceptibility - Zero Field

The magnetic susceptibility of powder and aligned single crystal samples was measured in a field of less than 5 0e. from 0.01K to 4.2K. Temperatures from 4.2 to 1.1K were achieved in a conventional He^4 cryostat[50]. The ultra-low temperatures were produced in a He^3-He^4 dilution

refrigerator.[51] Both conventional ac mutual inductance coils and a superconducting quantum interference device (SQUID) magnetometer were used.[52]

The experimental susceptibilities are rather large ($\chi \simeq 16$ emu/mole) and significant corrections for the Lorentz and demagnetizing fields were made. The expression for the corrected susceptibility in terms of the measured susceptibility is derived in Chapter I (THE INTERNAL FIELD IN A MAGNETIC SAMPLE) and is given here for convenience.

$$\chi^{\circ} = \frac{\chi_m}{1 + (\frac{4\pi}{3} - D)\frac{\chi_m \rho}{M.W.}} \qquad (70)$$

where as before: χ_o is the susceptibility that would be observed in the absence of any demagnetizing or Lorentz fields; χ_m is the experimentally measured susceptibility; D is the demagnetizing factor; ρ is the density and M.W. is the molecular weight. Numerical values for the corrections which were made to the susceptibilities of both single crystal and powder samples are given in Table VI along with figures indicating the sample shapes used in the various experiments. The numbers were obtained by assuming that the single crystals approximated oblate spheroids of the appropriate axial ratios. The corrected susceptibility data are shown in FIGURES 37 and 38. The powder data and the single crystal data exhibit similar

TABLE VI

Demagnetizing corrections for various samples of copper L-Isoleucine

SAMPLE NO. 1 (SQUID)

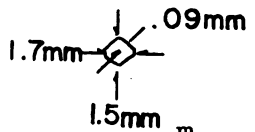

m = .00037 gr

$$\chi_a^\circ = \frac{\chi_a^m}{1+0.016\chi_a^m} \qquad \chi_b^\circ = \frac{\chi_b^m}{1-0.032\chi_b^m} \qquad \chi_c^\circ = \frac{\chi_c^m}{1+.016\chi_c^m}$$

SAMPLE NO. 2 (COILS)

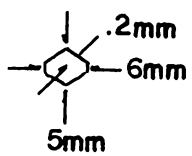

m = 0.015 gr

$$\chi_a^\circ = \frac{\chi_a^m}{1+.0165\chi_a^m} \qquad \chi_b^\circ = \frac{\chi_b^m}{1-.0477\chi_b^m} \qquad \chi_c^\circ = \frac{\chi_c^\circ}{1+.0164\chi^m}$$

SAMPLE NO. 3 (POWDER)

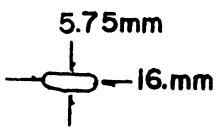

m = .139 gr

$$\bar{\chi}^\circ = \frac{\bar{\chi}^m}{1+.015\bar{\chi}_m}$$

FIGURE 37. Zero field susceptibility of copper L-Isoleucine. Curve "a" is a Curie Weiss law and curve "b" is a high temperature expansion for a two dimensional ferromagnetic Heisenberg exchange.

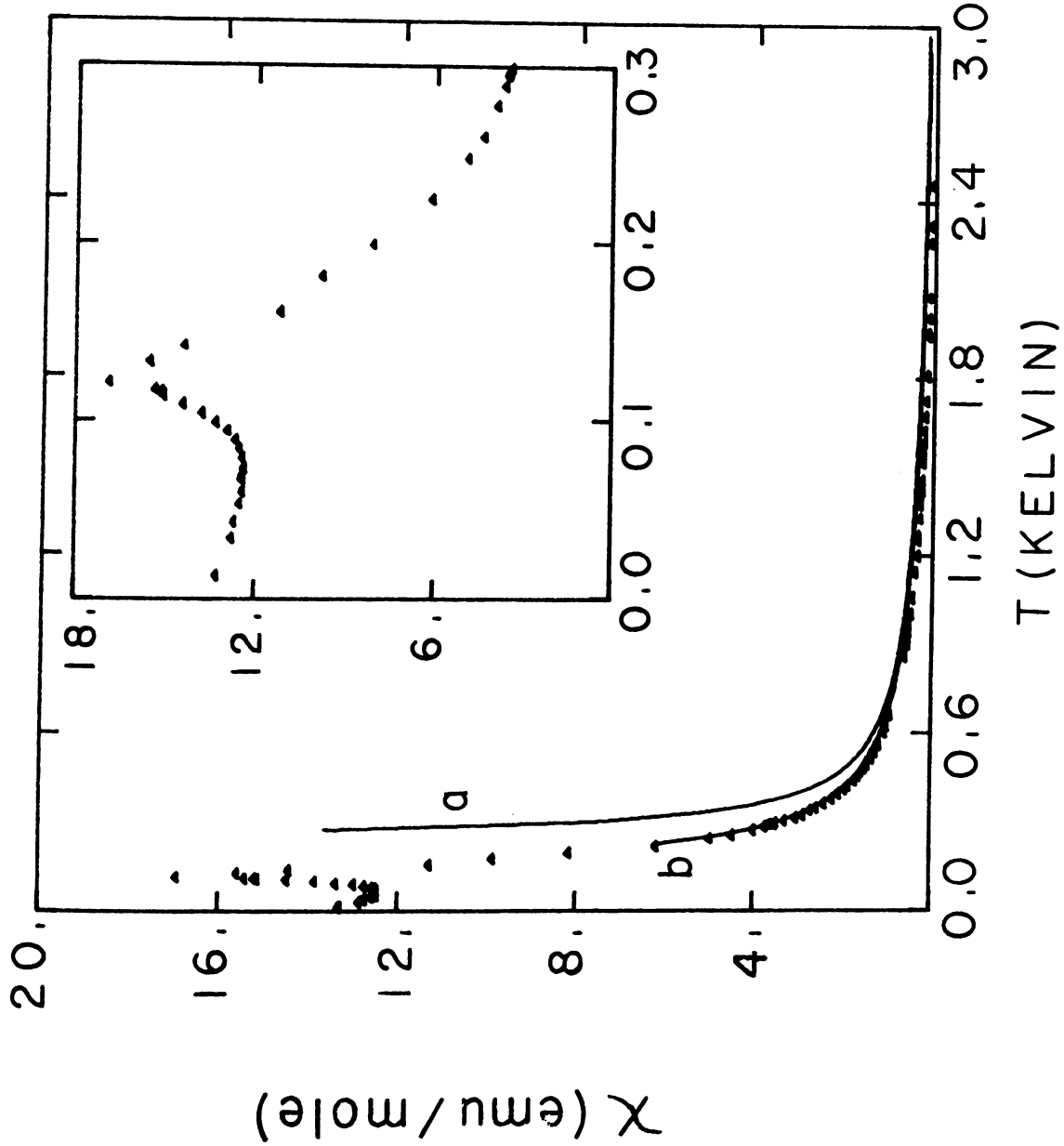
χ (emu/mole)
T (KELVIN)
a
b
20.
16.
12.
8.
4.
0.0
0.6
1.2
1.8
2.4
3.0
18.
12.
6.
0.0
0.1
0.2
0.3

FIGURE 38. Inverse susceptibility of copper L-Isoleucine. Solid line is a Curie Weiss law.

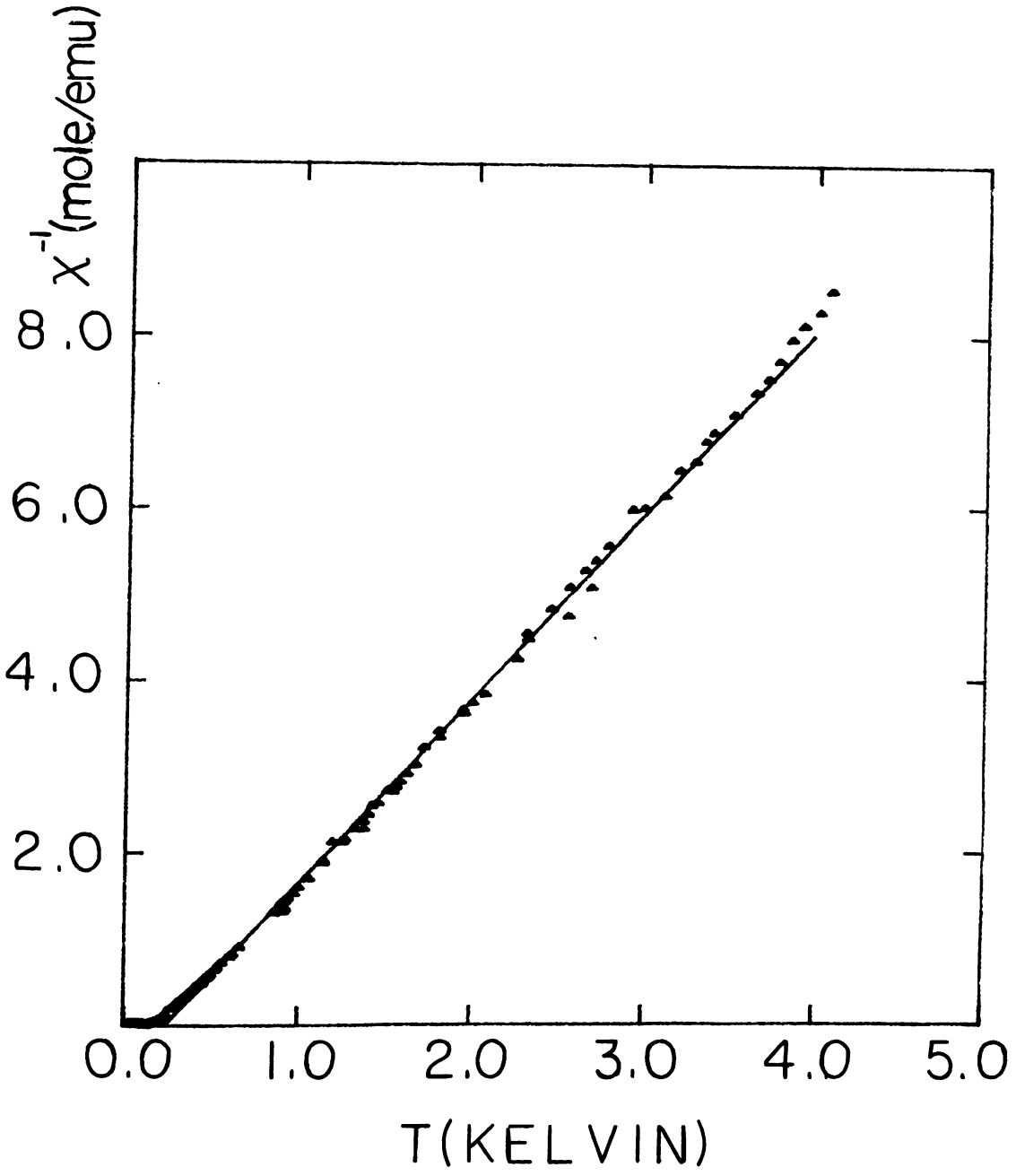
8.0
6.0
4.0
2.0
χ^{-1}(mole/emu)
0.0
1.0
2.0
3.0
4.0
5.0
T(KELVIN)

behavior over the entire experimental temperature range. In all cases, the susceptibility is Curie-Weiss like from 4.2K down to 0.05K. The data then passes through a large ($\chi \simeq 16$ emu/mole) well defined peak at T_c = 0.117K. Below this temperature the susceptibility falls, levels off, and then begins to rise again near 0.03k.

B. Magnetic Susceptibility - Applied Field

The ac susceptibility was measured in applied static fields up to 200 Oe. in the temperature range from 0.01 to 0.3K. The experiment was performed using conventional mutual inductance coils inside a superconducting solenoid.[53] At low fields, the critical temperature is depressed for all orientations of the magnetic field but somewhat more with H applied parallel to a or c than with H along the b axis. At low temperatures (below .1K) a peak (FIGURE 39) in the susceptibility is observed with H parallel to the a and c axes at $H_{crit} \simeq 140$ Oe.

FIGURE 40 is a composite graph of the applied field susceptibility data for all three axes. The diagram reveals the presence of at least three distinct magnetic phases with a triple point at $H_{TP} \simeq 150$ Oe.and $T_{TP} \simeq 0.050$K.

The internal field with H along b is significantly affected by the demagnetizing field. Our previous methods

FIGURE 39. Magnetic susceptibility of copper L-Isoleucine with H parallel to the c axis.

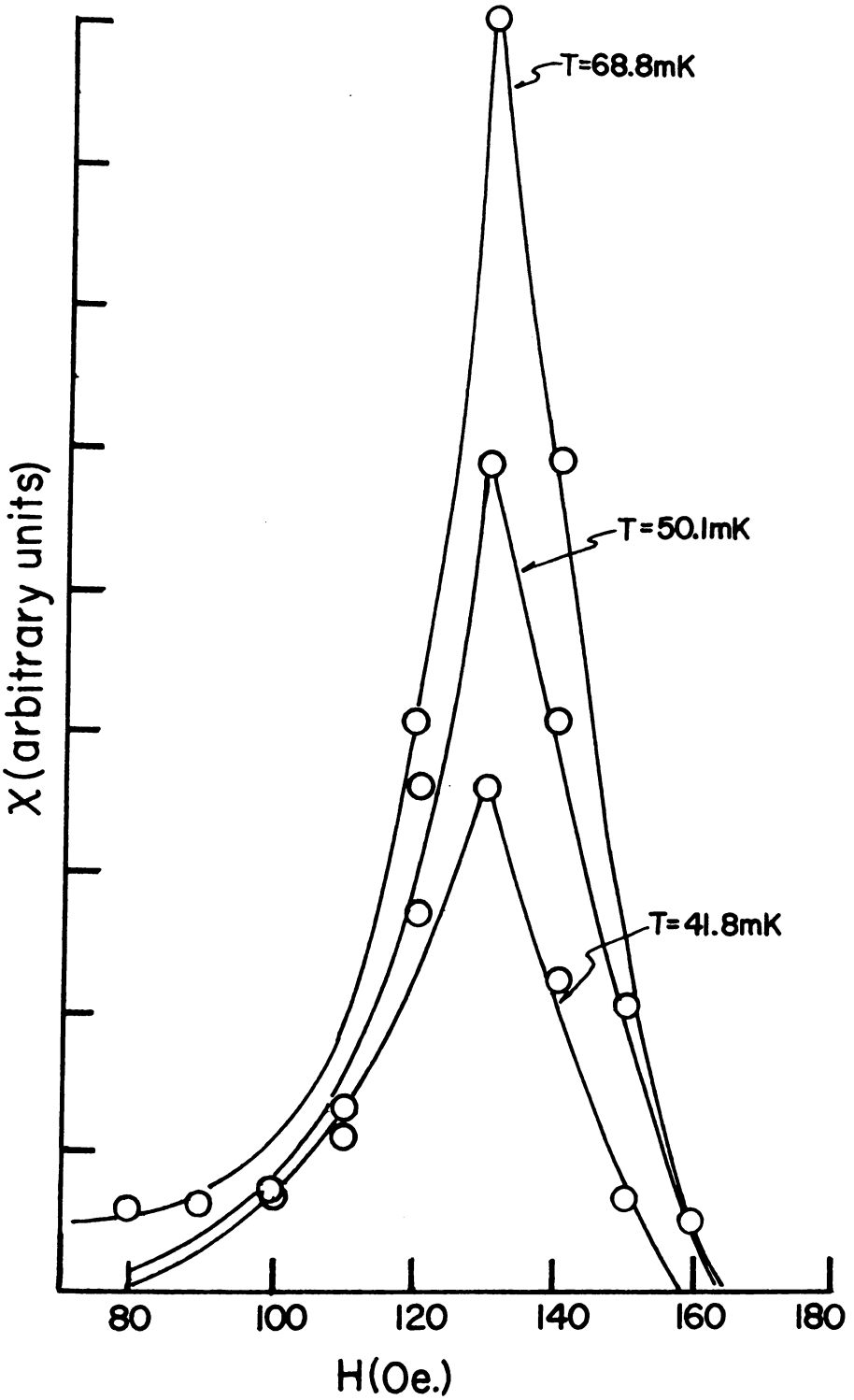
T=68.8mK
T=50.1mK
T=41.8mK
χ(arbitrary units)
80
100
120
140
160
180
H(Oe.)

FIGURE 40. Composite H-T phase diagram for copper L-Isoleucine.

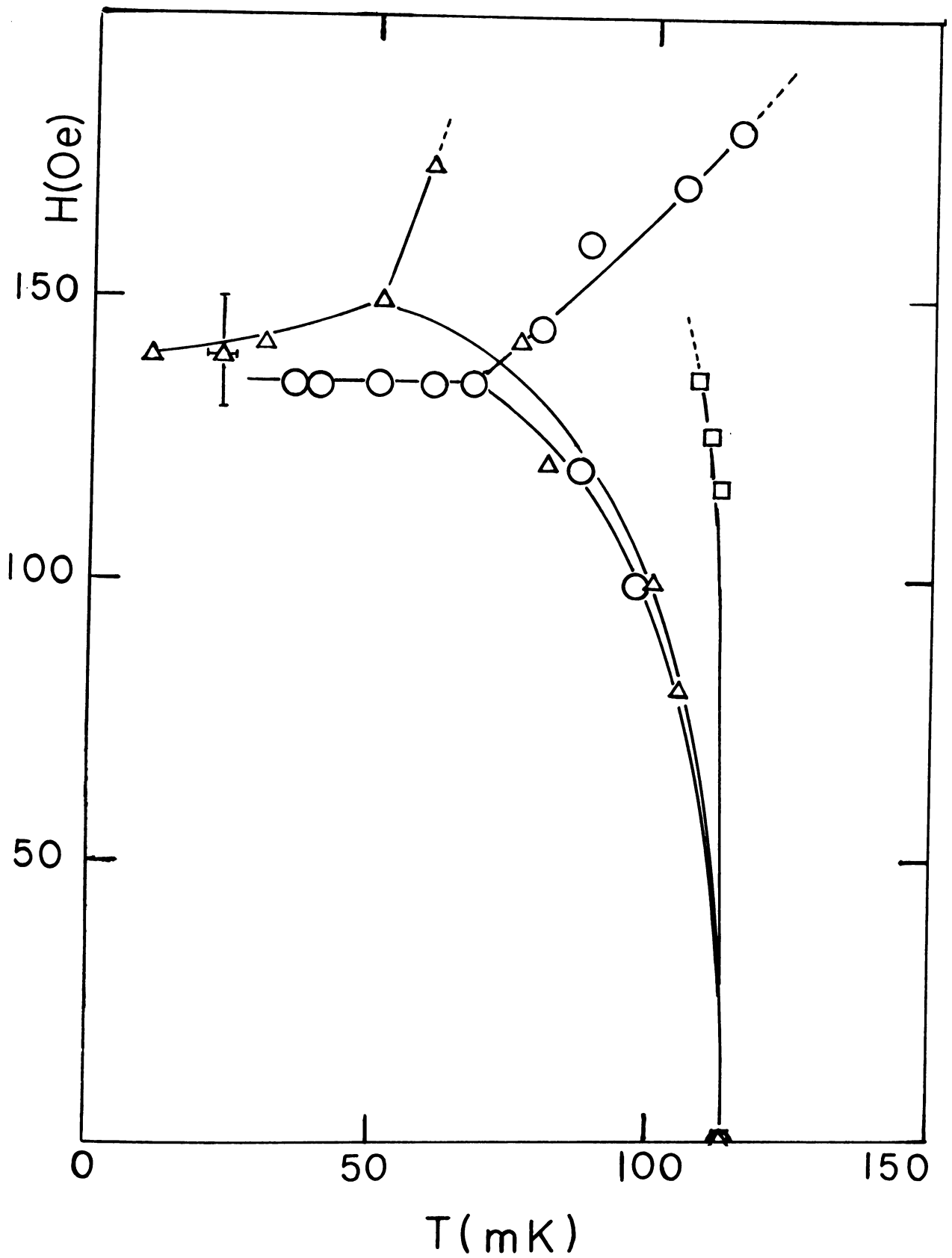
H(Oe)
150
100
50
0
50
100
150
T(mK)

of correcting for the demagnetizing and Lorentz fields are no longer applicable because of the large fields and anomalous behavior of the susceptibility along the a and c axes, which indicates M is no longer a linear function of H. However, we may crudely estimate the highest internal field which would result from a 200 Oe. field along the b axis. Let us assume that

$$M = \chi H \tag{71}$$

The internal field is given by:

$$H_{int} = H_{app} + (\frac{4\pi}{3} - D)\chi^{\circ} H_{int} \frac{\rho}{M.W.}$$

$$H_{int} = \frac{H_{app}}{1-(\frac{4\pi}{3} - D)\chi^{\circ}\frac{\rho}{M.W.}} \tag{72}$$

Using the data in TABLE VI for sample number 2:

$$H_{int}^{max} = \frac{200}{1-(.0477)16} = 113 \text{ Oe.}$$

C. Electron Spin Resonance

Electron spin resonance experiments were performed on aligned single crystals at temperatures near 1°k. The data was taken using a rectangular cavity immersed in liquid He^4. Rotation diagrams were obtained at x-band

(9.2 GHz) about all thru crystallographic axes. In addition, the a axis data were taken at k-band (22 GHz) to improve the resolution of the lines (FIGURE 41). Since these experiments were performed in the paramagnetic state at relatively low fields (the argument for the Brillouin function is 0.2), we may use our previously derived expressions to correct the internal field for demagnetizing effects:

$$H_{int} = H_{app} + (\frac{4\pi}{3} - D)\ \chi^{\circ}H_{int}\frac{\rho}{M.W.}$$

$$H_{int} = \frac{H_{app}}{1-(\frac{4}{3} - D)\chi_{o}\frac{\rho}{M.W.}}$$

$$g^{\circ} = \frac{h\nu}{\mu_B H_{int}} = \frac{h\nu}{\mu_B H_a}\ (1-(\frac{4\pi}{3} - D)\chi_{o}\frac{\rho}{M.W.}$$

$$= g_{meas}\ (1-(\frac{4\pi}{3} - D)\chi_o\ \frac{\rho}{M.W.} \qquad (73)$$

where h = Plank's constant

ν = microwave frequency

The corrected rotation diagrams are shown in FIGURES 42-44. Each diagram is symmetric about the crystallographic axes. This is consistent with the point group 222 (three orthogonal two-fold axes) which results from the reported space group $P2_12_12_1$.

FIGURE 41. ESR signals with H in the bc plane of copper L-Isoleucine. Curve a is for H parallel to c. Curve b is with H 50° from c.

FIGURE 42. ESR rotation about the a axis in copper L-Isoleucine

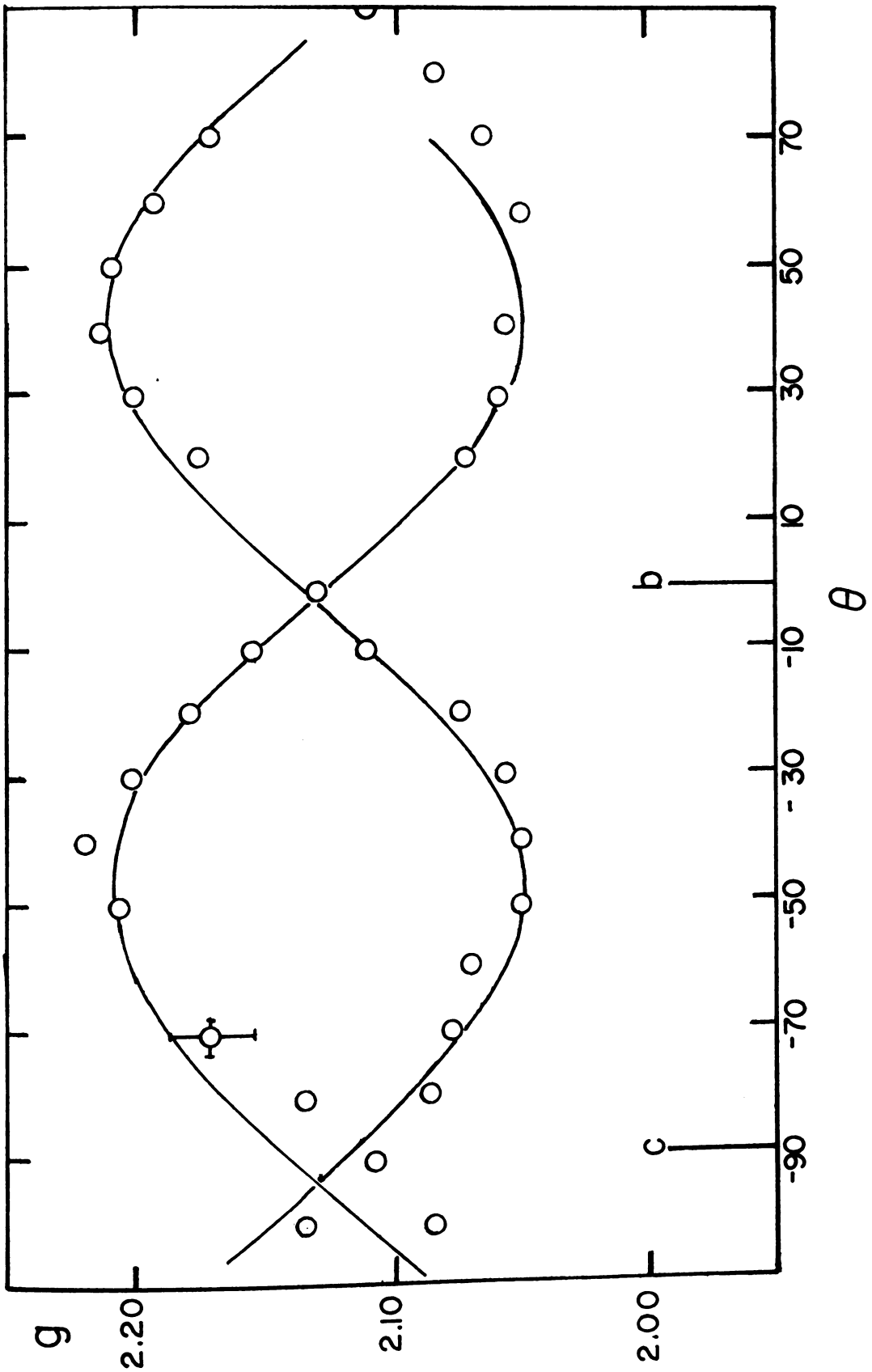
g
2.20
2.10
2.00
c
b
θ
-90
-70
-50
-30
-10
10
30
50
70

FIGURE 43. ESR rotation about the b axis.

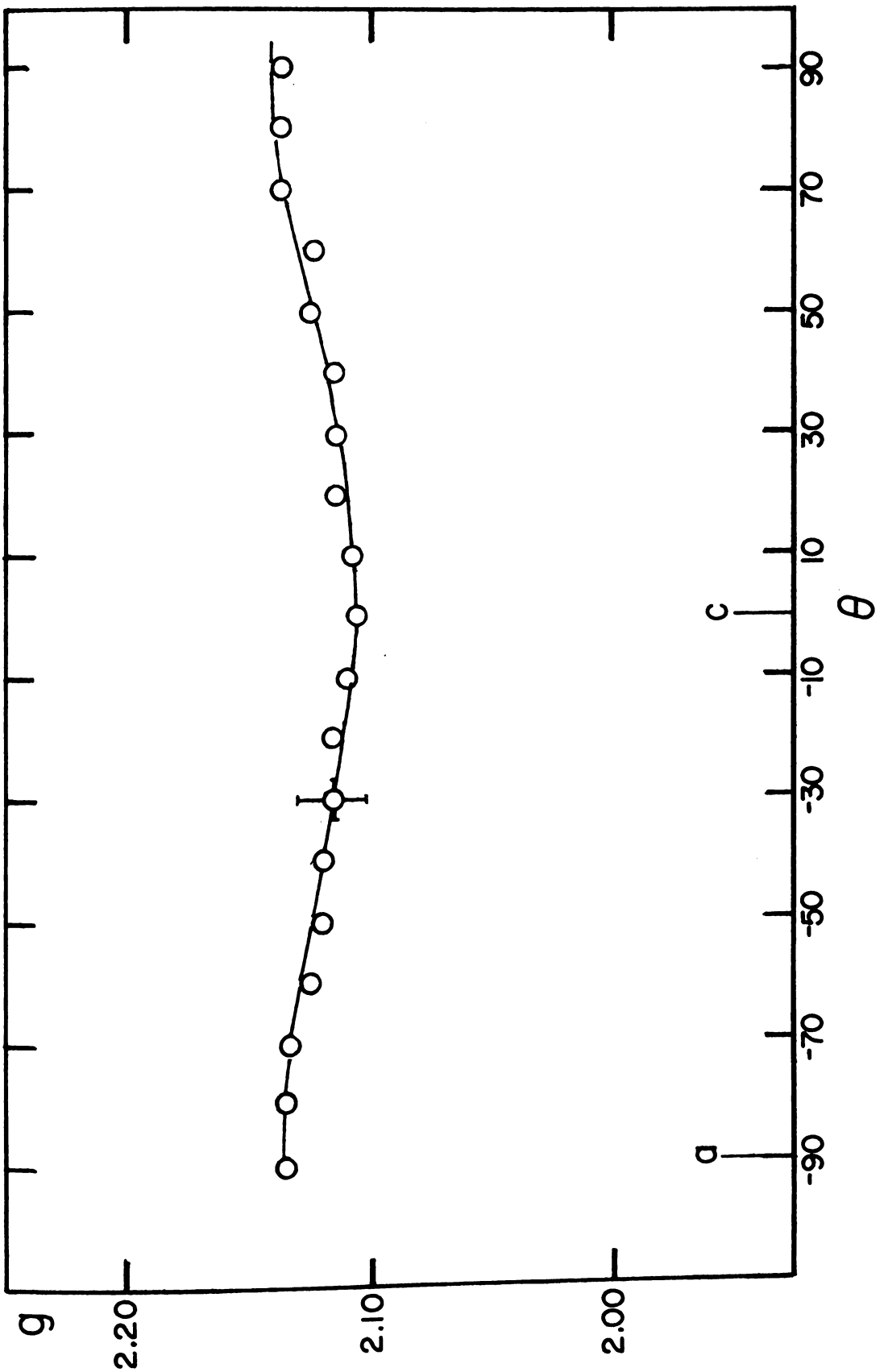
g
2.20
2.10
2.00
a
c
θ
-90
-70
-50
-30
-10
10
30
50
70
90

FIGURE 44. ESR rotation about the c axis.

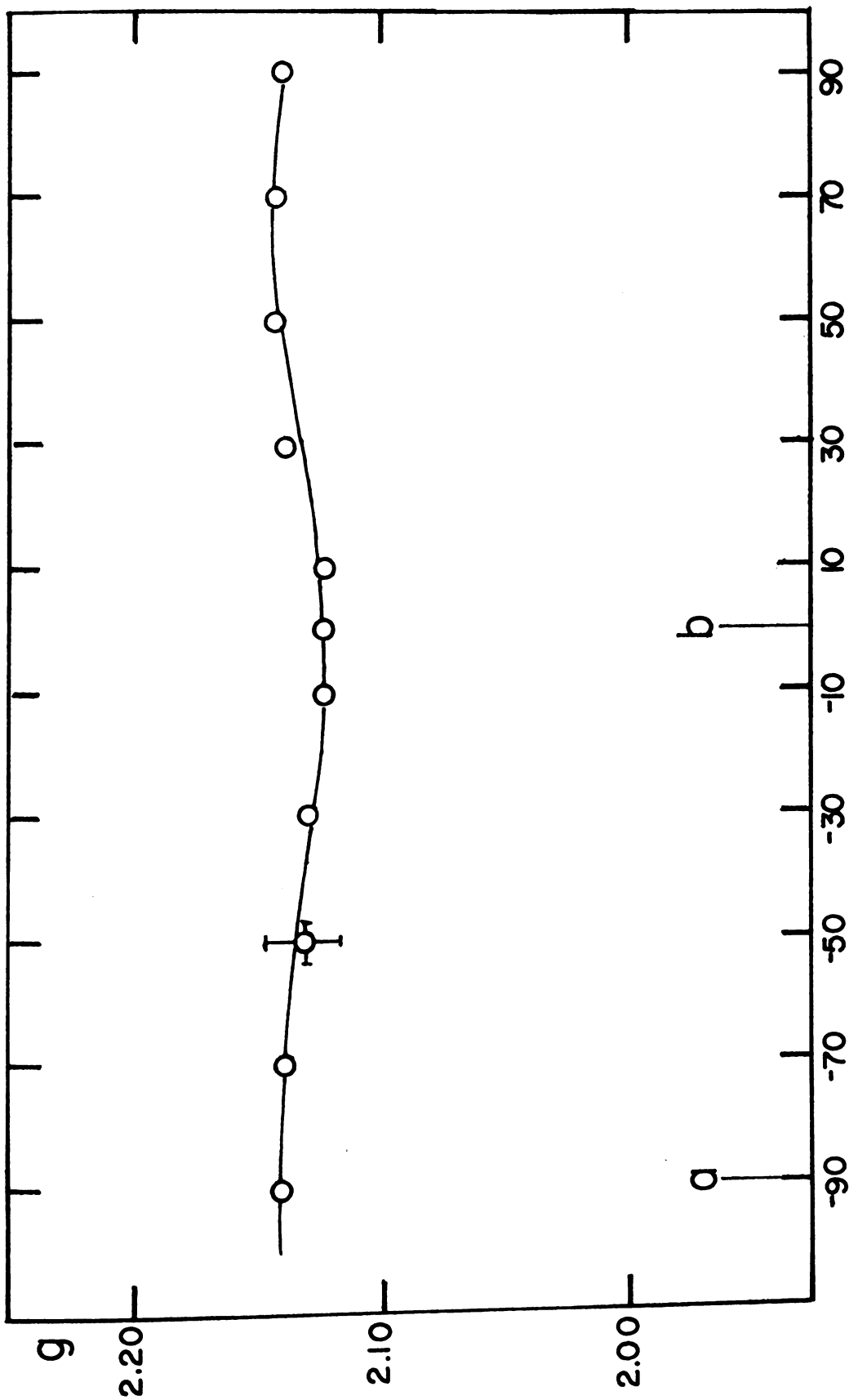
g
2.20
2.10
2.00
a
b
-90
-70
-50
-30
-10
10
30
50
70
90

The ESR signal for the b and c axis rotations consists of a single line of essentially constant width which exhibits only a slight g-factor anisotropy. The a axis signal consists of two lines (FIGURE 41) with a large g-factor anisotropy and an anisotropic line width.

The rotation data for each axis was analyzed[54] using the expression

$$g^2 = \alpha + \beta \cos 2\phi + \gamma \sin 2\phi \qquad (74)$$

which gives the g value at the relative rotation angle ϕ. The coefficients in this expression are given by:

$$\alpha = \frac{g_+^2+g_-^2}{2} \qquad \beta = \frac{g_+^2-g_-^2}{2} \cos 2\phi_+ \qquad \gamma = \frac{g_+^2-g_-^2}{2} \sin 2\phi_+ \qquad (75)$$

where the maximum and minimum g values (g_+ and g_-) occur at the relative angles ϕ_+ and ϕ_- respectively. These parameters are then used to determine a matrix $\overleftrightarrow{W}$ whose components are given[55] by:

$$W_{11} = \alpha_a+\beta_a \qquad W_{22} = \alpha_b+\beta_n \qquad W_{33} = \alpha_c+\beta_c$$

$$W_{22} = \alpha_a-\beta_a \qquad W_{33} = \alpha_b-\beta_b \qquad W_{11} = \alpha_c-\beta_c$$

$$W_{12} = \gamma_a \qquad W_{23} = \gamma_o \qquad W_{13} = \gamma_c$$

$$W_{12} = W_{21} \qquad W_{23} = W_{32} \qquad W_{13} = W_{31}$$

where, for example, α_a is the parameter from the fit to the a axis rotation data. The eigenvalues of this matrix are the squares of the three principal g-values. The eigenvectors indicate the orientation of the principal axes relative to a set of fixed axis, which in this case are the crystallographic axes. Two rotationally inequivalent g tensors have been derived from the b and c axis data and each of the two rotation patterns of the a axis. The principal g values and direction cosines for each of these tensors are given in TABLE VII. The orientation of the derived principal axes relative to the square pyramidal local coordination of the copper atom is shown in FIGURE 60. The two g tensors have their maximum g values in the direction of the "tip" of the pyramid. The pyramids and the g tensors are rotated ±51° from the crystallographic b axis in the ac plane.

The g values along the crystallographic axes are derived from the principal axis g values and are given:

$$g_a = 2.147 \pm .005 \quad g_b = 2.130 \pm .005 \quad g_c = 2.130 \pm .005$$

Finally, if one assumes the anisotropy in the line width is unresolved hyperfine structure due to the copper (I=3/2) nucleus, one can estimate a hyperfine interaction of approximately 0.02 $cm.^{-1}$, which is quite reasonable for copper.

TABLE VII

Principal values and direction cosines of the principal axes of the two g tensors

	Site 1	Site 2
g_1	2.213 ± 0.005	2.213 ± 0.005
g_2	2.042 ± 0.005	2.042 ± 0.005
g_3	2.142 ± 0.005	2.142 ± 0.005
x_1	(0.00, 0.78, -0.63)	(0.00, 0.78, 0.63)
x_2	(0.00, 0.78, 0.63)	(0.00, 0.78, -0.63)
x_3	(1.00, 0.00, 0.00)	(1.00, 0.00, 0.00)

III. Discussion

A. Magnetism of $3d^9$ Electrons in a 4mm Crystal Field

In copper L-Isoleucine, the Cu^{2+} ion has an electronic orbital configuration of $3d^9$ which is equivalent to having a single vacancy or "hole" in one of the d orbitals. This orbital configuration always results in an S=1/2 spin state. The spatial extent of each of the five d orbitals is shown in FIGURE 8 in Chapter I, CRYSTAL FIELD THEORY. In the isolated ion, the energies of these orbitals are all degenerate. To see how the orbital degeneracies are lifted in the crystalline electric field of copper L-Isoleucine, we shall first examine the behavior of the d orbitals in the symmetry of the local coordination of the ligands.

As previously indicated, the copper atom is coordinated with five ligands. The spatial arrangement of the two nitrogen and three oxygen ligands approximates a square pyramid (see FIGURE 34). The point group symmetry of this configuration is 4mm (C_{4v}), which consists of a four fold axis and four mirror planes. The sterographic projection of the point group diagram as well as the spatial location of these operations in the square pyramid are shown in FIGURE 45. The symmetry of the irreducible representations[56] in the point group 4mm are shown in TABLE VIII.

FIGURE 45. Stereographic projection of the point group 4mm (upper) and the location of the four mirror planes and the four-fold rotation axis in the square pyramid (lower).

TABLE VIII

Irreducible representations of the point group 4mm

4mm (C_{4v})	
A_1	Z, X^2+Y^2, Z^2
A_2	I_z
B_1	X^2-Y^2
B_2	XY
E	X, Y, XZ, YZ, I_xI_y

Under the symmetry of this group, d_{xz} and d_{yz} both belong to the same irreducible representation and as such, cannot have their degeneracy lifted by an interaction having the symmetry of 4mm. However, the other three orbitals $d_{x^2-y^2}$, d_{z^2} and d_{xy} may be split by such an interaction. To determine the nature of the splitting, we must consider the details of the interactions of the nine copper electrons with the surrounding atoms in the copper L-Isoleucine crystal.

We can simplify our analysis of the copper system in the manifold of the nine d electronic wave functions by first comparing the relative crystalline electric field energies of each of the orbitals. The lowest energy configuration occurs with the four lowest orbitals doubly

occupied and a "hole" in the highest orbital. Instead of performing the analysis based on the nine electrons, one can invert the order of the energy levels of the orbitals and carry out the analysis using a single positively charged "hole" in the ground state orbital. We shall therefore begin by qualitatively determining the relative energies of the five d-orbitals in the presence of the 4mm crystalline electric field of copper L-Isoleucine.

The $\hat{z}$ axis is placed along the tip of the pyramid and the $\hat{x}$ and $\hat{y}$ axes pass through the corners of the base of the pyramid:

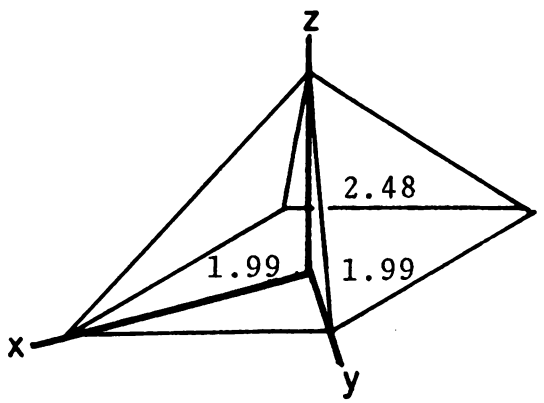

The separation of each ligand atom from the central copper atom is also indicated. By examining FIGURE 8, which shows the spatial orientation of the d-orbitals, we can see that the $d_{x^2-y^2}$ orbital will point towards each of the four ligands in the base of the pyramid. Taking the ligand atoms as point charges this state should have the highest energy due to the repulsion of the copper electrons by the

electronic charge on the ligands. The next lowest energy level is the d_z^2 orbital which points toward the one water oxygen located at the tip of the pyramid. Next is probably d_{xy} which is in the base of the pyramid between the ligands. Finally, the d_{xz} orbitals which fall between ligands and extend above and below the base of the pyramid are related by the four fold rotation axis which passes through the tip and center of the base. These last two levels are degenerate and probably lowest in energy. The resulting energy level diagram and the inverted picture used in the "hole" analysis are:

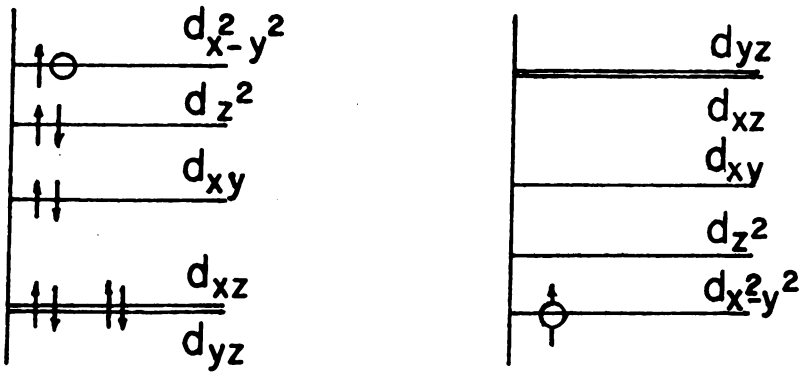

Having deduced the relative position of the energy levels, we may show how this affects the magnetic moment. In particular, we shall show in which direction relative to the square pyramidal coordination, the spectroscopic splitting factor (g-factor) deviates most from 2.

The Zeeman energy of the magnetic moment of an electron including both the spin and orbital contributions is given by

$$H = \vec{\mu}\cdot\vec{H} = -\mu_B\vec{H}_o\cdot(\vec{L} + 2\vec{S}) \tag{76}$$

where μ_B is the Bohr magneton and $\vec{H}_o$ is the applied field One can measure the energy difference between levels with an electron spin resonance experiment. One writes the Hamiltonian using an effective "g" factor:

$$H = -g\mu_B\vec{H}\cdot\vec{S} \tag{77a}$$

$$= -g\mu_B H_o S_z \quad \text{e.g.} \tag{77b}$$

The energy difference between adjacent levels is:

$$\Delta E = -g\mu_B H_o(m_i - m_j) \tag{78}$$

However, magnetic resonance experiments involve magnetic dipole transitions which obey the selection rule

$$\Delta m = \pm 1 \ .$$

Setting the energy difference equal to the energy of the photon:

$$h\nu = \Delta E = g\mu_B H_o \tag{79}$$

This effective g factor differs from the "Lande" g factor which is given by

$$g_{Lande} \equiv \frac{\langle \vec{\mu} \cdot \vec{J} \rangle}{J^2} \frac{h}{\mu_B}$$

$$= -\mu_B \frac{\langle (\vec{L}+2\vec{S}) \cdot (\vec{L}+\vec{S}) \rangle}{J^2} \frac{h}{\mu_B}$$

$$= \frac{-\mu_B \langle \frac{1}{2} \langle L^2 + 3J^2 + S^2 \rangle}{} \frac{h}{\mu_B}$$

$$g_{Lande} = \frac{\ell}{2}(\ell+1) + \frac{3}{2} j(j+1) + \frac{1}{2} S(S+1) \qquad (80)$$

Comparing equations (12) and (13a), with equation (7) we see that the "effective" g factor as well as the Lande g-factor will be different from 2 only when $\vec{L}$ is nonzero. In the magnetic resonance experiment, this orbital effect manifests itself as an additional contribution to the Zeeman energy:

$$E = \langle d_i | -\mu_B \vec{H} \cdot \vec{L} | d_j \rangle \qquad (81)$$

The maximum deviation from g=2 will occur when this term is largest. The d-orbitals can be written[57] as linear combinations of the spherical harmonics Y_2^m:

$$d_{x^2-y^2} = \frac{1}{2}(Y_2^2 + Y_2^{-2}) \qquad d_{z^2} = Y_2^0$$

$$d_{xy} = \frac{1}{\sqrt{2}}(Y_2^2 - Y_2^{-2}) \qquad d_{xz} = \frac{1}{\sqrt{2}}(Y_2^1 + Y_2^{-1})$$

The matrix elements of the components of the operator L are given by:

$$\langle Y_2^m | L_z | Y_2^n \rangle = n \, \delta_{nm}$$

$$\langle Y_2^m | L_x | Y_2^n \rangle = \frac{1}{2} \langle Y_2^m | L_+ + L_- | Y_2^n \rangle$$

$$= \frac{1}{2} \sqrt{(\ell-n)\ (\ell+n+1)}\ \delta_{m,n+1}$$

$$+ \frac{1}{2} \sqrt{(\ell+n)(\ell-n+1)}\ \delta_{m,n-1}$$

$$\langle Y_2^m | L_y | Y_2^n \rangle = \frac{1}{2i} \langle Y_2^m | L_+ - L_- | Y_2^n \rangle$$

$$= \frac{1}{2i} \sqrt{(\ell-n)(\ell-n+1)}\ \delta_{m,n+1}$$

$$- \frac{1}{2i} \sqrt{(\ell+n)(\ell-n+1)}\ \delta_{m,n-1}$$

Returning to our analysis of $3d^9$ copper with the single "hole" in the "ground state" $d_{x^2-y^2}$, we see the zero order matrix element of $\vec{H}\cdot\vec{L}$ is:

$$\langle Y_{x^2-y^2} | \vec{H}\cdot\vec{L} | D_{x^2y^2} \rangle = \frac{1}{L} \langle Y_2^{-2}+Y_2^2 | H_x L_x\, \hat{x} + H_y L_y\, \hat{y}$$

$$+ H_z L_z\, \hat{z}\ | y_2^2+Y_2^{-2} \rangle = 0 \qquad (82)$$

Indeed there are no nonzero diagonal elements for any of the other d-orbitals. In second order, the energy is given by:

$$E^{(2)} = \sum_k \frac{|\langle d_{x^2-y^2}|\vec{H}\cdot\vec{L}|d_k\rangle|^2}{E^\circ_{x^2-y^2} - E^\circ_k} \tag{83}$$

The first excited orbital is d_{z^2}. However, matrix elements of the Hamiltonian between $d_{x^2-y^2}$ and d_{z^2} are zero. There is a matrix element of the z component of the Hamiltonian between $d_{x^2-y^2}$ and the next highest orbital d_{xy}, which is nonzero:

$$M = \langle d_{x^2-y^2}|H_z L_z|d_{xy}\rangle$$

$$= \frac{1}{2}\langle Y_2^2 + Y_2^2|H_z L_z|Y_2^2 - Y_2^{-2}\rangle$$

$$= 2H_z$$

which gives a contribution to the energy:

$$E^{(2)} = \frac{|2H_z|^2}{E^\circ_{x^2-y^2} - E^\circ_{xy}} \tag{84}$$

The matrix elements of the x and y components in the Hamiltonian are zero between these states, therefore the largest deviation from g=2 occurs with the external field parallel to the z axis. There are matrix elements for the

x and y components between other states, but those terms involve higher energy states and therefore are reduced by the larger energy denominator.

Experimentally, the largest g value (2.21) for copper L-Isoleucine was indeed observed with the external magnetic field along the z axis of the pyramid.

B. Magnetic Susceptibility

The copper L-Isoleucine molecules are linked in two dimensions by hydrogen bonds which extend in the a and c directions (see FIGURE 35). The lack of much covalent character of hydrogen bonds should produce only weak super exchange between copper spins. Pauling has indicated[58] that in certain instances the hydrogen actually resonates between equilibrium positions on the opposite ends of the "bond." It may then provide the exchange mechanism for the interactions between the copper spins.

The experimental susceptibility well above the critical temperature fits a Curie Weiss law:

$$\chi = \frac{C}{T-\theta} \tag{85}$$

with a positive (ferromagnetic) Weiss constant of $\theta_W = 0.240k$, and a Curie constant of C = 0.466. Below approximately 1°K, the susceptibility deviates from Curie-Weiss behavior. This is perhaps best shown by

FIGURE 46 which is a plot of $C/\chi T$ versus J/kT. In this type of plot, a Curie Weiss law is a straight line which intercepts the x axis at $\theta=T$(curve a). Curve b is obtained using the first 10 terms of a high temperature expansion (see Appendix A, THE METHOD OF HIGH TEMPERATURE EXPANSION) by Baker and Rushbrooke[59] for a two dimensional square net lattice of spins that interact through an isotropic Heisenberg exchange:

$$H = 2J \sum_{i \neq j} \vec{S}_i \cdot \vec{S}_j$$

where J is the exchange constant between a copper atom and its four nearest neighbors on the same two dimensional "sheet." The parameters which give the best fit to the experimental data are g = 2.18 and J/k = +0.120K (ferromagnetic). This exchange compares favorably with the Curie-Weiss constant which is 2J/k (.244K) for the same number of nearest neighbors. The system is at best only approximated by a square net. A two dimensional exchange is however, consistent with the nature of the crystal lattice. The experimental susceptibility data was also compared with a two dimensional x-y model[60] and a two dimensional Ising[61] model. The agreement between the experimental data and these last two theoretical models was not as good as with the two dimensional Heisenberg model.

FIGURE 46. Reduced inverse susceptibility plotted as a function of reduced inverse temperature. Curve a is a Curie-Weiss law; curve b is a high temperature expansion for a two-dimensional ferromagnetic Heisenberg exchange.

There are three aspects of the data near and below the critical temperature which are interesting and not entirely understood: (1) the peak in the susceptibility measured along all three axes; (2) the anisotropic behavior in applied field below T_c and finally, (3) the rising susceptibility at the lowest experimental temperature. The peak in the susceptibility at $T=T_c$ and the subsequent decrease in susceptibility for slightly lower temperatures is thought to indicate a transition to a three dimensionally ordered antiferromagnetic state. This three dimensional ordering is caused by an antiferromagnetic coupling between sublattices on adjacent "sheets." This coupling may be dipolar or a "real" superexchange. Further evidence for the existence of a three dimensionally ordered state below T_c, is supplied by the susceptibility data in applied field. The anomalous peak in the susceptibility as a function of applied field indicates a discontinuous change in magnetization. This implies the existence of a sublattice magnetization with the associated long range ordering.

The exact nature of the ordered state and the magnetic transition are not at present understood. The fact that the zero field susceptibility is approximately isotropic below the critical temperature contraindicates a uniaxial antiferromagnet as does the observation of a magnetic phase transition with the applied field along two different orthogonal axes. As we have shown in the previous

theoretical discussion of the uniaxial antiferromagnet, a sharp transition is observed only with the field applied along the sublattice magnetization. The observed transitions indicate then, that the system consists of more than two sublattices. However, more experimental evidence such as N.M.R. or neutron diffraction in the ordered state is needed to illuminate the nature of the spin system in the ordered state.

Finally, the third aspect of the magnetic behavior, the rising susceptibility below 0.03K is still not understood. This effect was at first thought to be due to impurities or nonstoichiometric copper. A calculation of the impurity concentration necessary to produce the observed susceptibility can be made by assuming the rising susceptibility is due to a paramagnetic impurity described by:

$$\chi = \frac{C}{T}$$

The slope of the experimental values yields a Curie constant $C \simeq 0.6$. The theoretical expression for the Curie constant is:

$$C = \frac{Ng^2\mu_B^2 S(S+1)}{3k} \qquad (86)$$

where

N = Avogadro's number

g = spectroscopic splitting factor

μ_B = Bohr magneton

k = Boltzmann's constant

S = spin quantum number

The theoretical Curie constant for copper (assuming g=2.18) is 0.44. For an S=1 system such as nickel, C = 1.17 and for an S=5/2 system such as manganese, C=5.13. Comparison of these calculated constants with the experimental Curie constant derived from the ultralow temperature data indicates the sample is composed of: (1) 100% S=1/2 impurity; (2) 50% S=1 impurity or (3) 12% S=5/2 impurity. Neutron activation analysis eliminates the possibility of uncombined copper and the nominal quality of the reagent grade materials rules out other transition metal impurities in such high concentration. The source of this behavior remains unclear and requires further experimental investigation.

CHAPTER 5

CONCLUSIONS AND RECOMMENDATIONS

The two antiferromagnetic insulators discussed in this thesis have been shown to exhibit interesting magnetic behavior at low temperatures. The crystallographic space group of MBTMA was determined using X-ray and optical goniometry to be $P2_1/m$. A plausible model for the crystal structure has been derived from the space group which is consistent with (1) the structure of an associated compound CCTMA, (2) the number of molecules in the unit cell (3) the lattice dimensions (4) the number of zero field proton magnetic resonance line (5) the agreement between the calculated and experimental values for the NMR frequencies of the water proton and (6) the low dimensional behavior above T_N. The local coordination of the manganese (II) ion is apparently octahedral with four bromines and two waters of hydration. Magnetization and nuclear magnetic measurements made in the ordered state indicate that the magnetic state is characterized by a four sublattice canted antiferromagnet with a canting angle of approximately 4°. A field induced magnetic phase transition is observed at H_c = 1200 oersteds applied along the b

axis. This transition is asserted to be metamagnetic and results in a net moment.

The crystal structure of copper L-Isoleucine is characterized by "sheets" of hydrogen bonded copper L-Isoleucine molecules. The local coordination of the copper ion is five-fold and approximately square pyramidal. The two dimensional crystal structure is reflected in the magnetic properties above T_N. The zero field susceptibility is isotropic and is described in the temperature range from 4.2 to 0.5k as a two dimensional square net magnetic lattice which interacts through a ferromagnetic Heisenberg exchange. A transition to a three dimensional antiferromagnetic state occurs at T_c = 0.117K. A field induced magnetic phase transition is observed below T_N with the field applied along the a and c axes. The susceptibility at ultralow temperatures exhibits an anomalous increase with decreasing temperature. The spin state of the $3d^9$ copper ion in a crystal field of 4mm symmetry has been experimentally investigated using ESR in the paramagnetic state. The largest g value was found to occur with H applied along the "tip" of the square pyramidal local coordination. This is consistent with a qualitative theoretical analysis based on the Van Vleck point-charge model for crystal field interactions.

Further work clearly includes determination of the exact crystal structure of MBTMA. Once this is done the spin arrangement can be determined by "orienting" the spins so that the calculated magnetic dipole fields at the proton sites agree with the results of the zero field resonance. The nature of the transition in applied field may be further specified by observing the water proton lines above the transition, and again "orienting" the spins so as to produce calculated fields at the proton sites which agree with the observed resonances. Neutron scattering will probably not yield good results in this material due to the inelastic scattering from the large number of protons in the unit cell.

The specific heat of copper L-Isoleucine should be measured at ultra low temperatures to determine how much entropy is involved in the transition at 0.117K. If the result differs substantially from the expected $S=R\ell n2$, further experiments should be done at ultralow temperatures. The NMR at temperatures below T_c can be used to derive the orientation of the copper spins in the ordered state. At still lower temperatures, the NMR may be able to indicate whether the anomalous increase in susceptibility is due to a rearrangement of the magnetic sublattices. If the nuclear magnetic resonance of the water protons can be followed

through the field induced transition, the nature of the transition and the resulting spin configuration could be determined.

Finally, if a high spin transition metal ion complex of L-Isoleucine can be grown, the effect of the 4mm crystal field symmetry on the exchange and the single ion anisotropy may be investigated for different orbital configurations.

REFERENCES

1. E. Ising, Z. Phys., 31, 253 (1925)

2. D. C. Mattis, The Theory of Magnetism, Harper and Row (1965), p. 256.

3. L. Onsager, Phys. Rev., 65 117 (1944).
   L. Onsager, Nuovo Cimento Suppl., 6, 261 (1949).

4. C. N. Yang, Phys. Rev., 85, 809 (1952).

5. R. B. Griffiths, J. Math Phys., 8, 478 (1967).

6. N. D. Mermin and H. Wagner, Phys. Rev. Lett., 17, 1133 (1966).

7. H. E. Stanley and T. A. Kaplan, Phys. Rev. Lett., 17, 913 (1966); J. Appl. Phys., 48, 975 (1967).

8. Mermin and Wagner, Ibid.

9. R. D. Spence, Private communication (to be published).

10. C. W. Fairall, Ph.D. Thesis, Mich. State Univ., (1970), p. 55.

11. J. Kanamori, in Magnetism, Edited by G. Rado and H. Suhl, Academic Press (1963), Vol. 1, Chap. 4.

12. R. D. Spence, lecture notes from: "Symmetry in Solids," p. 28.

13. L. Pauling, The Nature of the Chemical Bond, Cornell Univ. Press, 1948, p. 82.

14. G. M. Barrow, Physical Chemistry, McGraw Hill, 1961, p. 530.

15. J. Becquerel, Z. Physik, 58, 205 (1929).

16. H. Bethe, Ann. Physik, 3, 135 (1929).

17. J. H. Van Vleck, Theory of Magnetic and Electric Susceptibilities, Oxford Univ. Press (1932).

18. J. H. Van Vleck, J. Chem. Phys. 3, 803 (1935).

19. Kleiner, J. Chem Phys. 20, 1784 (1952).

20. Tanabe and Sugano, J. Appl. Phys. 33, 303 (1962).

21. Tanabe and Sugano, Phys. Rev. Lett. 7, 157 (1961).

22. C. J. Balhausen, Introduction To Ligand Field Theory, McGraw Hill, 1962, p. 65.

23. D. H. Martin, Magnetism In Solids, Illife Books, Ltd., 1967, p. 188.

24. J. A. Osborn, Phys. Rev. 67 351 (1945).

25. A. H. Morrish, The Physical Principles of Magnetism, John Wiley and Sons, 1965, p. 8.

26. T. R. McGuire, Jour. Appl. Phys. 38, 1299 (1967).

27. P. P. Cioffi, Rev. Sci. Instr., 21, 624 (1950).

28. J. D. Jackson, Classical Electrodynamics, John Wiley and Sons, 1963, p. 157.

29. C. W. Fairall, Op. cit., p. 77.

30. C. R. Stirrat, S. Dudzinski, A. H. Owens and J. A. Cowen, Phys. Rev. B9, 2183 (1967).

31. J. N. McElearney, G. E. Shankle, D. B. Lossee, S. Merchant, and R. L. Carlin, A.C.S. Symposium Series Volume on "Extended Interactions Between Metal Ions in Transition Metal Complexes," Edited by L. V. Interante, 1975.

32. R. D. Spence and A. C. Botterman, Phys. Rev. B9, 2993 (1974).

33. D. B. Lossee, J. N. McElearney, G. E. Shankle, R. N. Carlin, P. J. Cresswell and Ward T. Robinson, Phys. Rev. B8, 2185 (1973).

34. D. B. Lossee, J. N. McElearney et al., Ibid.

35. D. B. Lossee, J. N. McElearney et al., Ibid.

36. R. D. Spence and A. C. Botterman, Ibid.

37. J. N. McElearney, G. E. Shankle et al., Ibid.

38. D. B. Lossee, J. N. McElearney et al., Ibid.

39. W. Opechowski and R. Guccione, in Magnetism, edited by G. T. Rado and H. Suhl, Academic Press, 1963, Vol. 2A, Chap. 3.

40. W. J. M. De Jonge, J. G. Resen, C. W. Swuste and R. D. Spence, Physica, 58, 544 (1972).

41. M. N. Sankarshana Murthy, A.P.B. Sinha and K. P. Sinha, Indian Journal of Pure and Applied Physics, 7, 665 (1969).

42. G. C. Allen and N. S. Hush, Inorg. Chem., 6, 4 (1967).

43. P. Day and C. K. Jørgensen, J. Chem. Soc., 6226 (1964).

44. J. Selbin, Coord. Chem. Rev., 1, 293 (1966).

45. John S. Wood, Prog. In Inor. Chem. Vol. 11, p. 227.

46. B. N. Misia, S. D. Sharma and S. K. Gripta, Jour. of Magnetic Resonance, 16, 193 (1974).

47. C. J. Radnell, J. R. Pillbrow, S. Subramanian and Max T. Rogers, Jour. Chem. Phys. 62, 4948 (1975).

48. G. L. Neiheisel, J. L. Imes, and W. P. Pratt, Jr., Phys. Rev. Lett., 35 101 (1975).

49. C. M. Weeks, A.Copper and D. A. Norton, Acta Cryst., B25, 443 (1969).

50. C. W. Fairall, op cit., p. 72.

51. J. L. Imes, G. L. Neiheisel, and W. P. Pratt, Jr., Jour. of Low Temp., Physics, 21, 1 (1975).

52. J. L. Imes, G. L. Neiheisel and W. P. Pratt, Jr., Ibid.

53. G. L. Neiheisel, Ph.D. Thesis, Mich. State Univ. (1975), p. 8.

54. W. G. Waller and M. T. Rogers, Journal of Magnetic Resonance, 9, 92 (1973).

55. W. G. Waller and M. T. Rogers, op.cit.

56. R. D. Spence, lecture notes from "Symmetry in Solids," p. 49.

57. C. J. Balhausen, op.cit., p. 64.

58. L. Pauling, op.cit., p. 289.

59. G. A. Baker, Jr., H. E. Gilbert, J. Eve, and G. S. Rushbrooke, Physics Letters A25, 207 (1967).

60. T. Ishikawa and T. Oguchi, Journal of the Physical Society of Japan, 31, 1021 (1971).

61. T. Ishikawa and T. Oguchi, Ibid.

APPENDICES

APPENDIX A

THE METHOD OF HIGH TEMPERATURE EXPANSION

The exact solutions of a Hamiltonian which describes the spin system in a real crystal is complicated by the presence of 10^{23} interacting "bodies." The quantum-mechanical-thermal average involves evaluating the trace of the Hamiltonian over all possible eigenstates of this 10^{23} many-bodied system. At sufficiently high temperatures such that kT is large compared to the interaction energies, we may approximate a solution to the thermodynamic quantities associated with the Hamiltonian through the use of a "high temperature expansion."

In this analysis, we expand the partition function "Z" as follows:

$$Z \equiv tre^{-\beta H}$$

$$= tr\left(1 - \beta H + \frac{\beta^2 H^2}{2!} - \frac{\beta^3 H^3}{3!} + \ldots\right)$$

$$= n_s - \beta trH + \frac{\beta^2}{2!} trH^2 - \frac{\beta^3}{3!} trH^3 + \ldots$$

where n_s is the number of thermodynamically accessible states. Let us examine this expansion for the Heisenberg Hamiltonian:

$$H = -2\sum_{ij} J_{ij} \vec{S}_i \cdot \vec{S}_j$$

We shall restrict the exchange to nearest-neighbor interactions.

$$J_{ij} = J$$

$$H = 2J\Sigma_{ij} \vec{S}_i \vec{S}_j$$

Then the partition function becomes:

$$Z = n_s - \frac{2J}{kT} \mathrm{tr}\Sigma_{ij} \vec{S}_i \cdot\cdot \vec{S}_j + \frac{2J}{kT}^2 \frac{1}{2!} \mathrm{tr}(\Sigma_{ij} \vec{S}_i \cdot \vec{S}_j)^2$$

$$- \frac{2J}{kT}^3 \frac{1}{3!} \mathrm{tr}(\Sigma_{ij} \vec{S}_i \cdot \vec{S}_j)^3 + \ldots$$

In order to evaluate the sums inside the traces, we must specify the arrangement of the spins. As an example, we shall take a two dimensional square net lattice. Each spin will have four nearest neighbors. The first sum:

$$\Sigma_{ij} \vec{S}_i \cdot \vec{S}_j$$

is the sum of nearest neighbor pairs. Since there are N spins in the crystal, each having four nearest neighbors, there are 4N such terms. This means that the linear term in the partition function is

$$- \frac{2J}{kT} (4N\mathrm{tr}(\vec{S}_i \cdot \vec{S}_j)$$

The quadratic term in the partition function produces three kinds of interactions:

1) two ion interactions $(\vec{S}_i \cdot \vec{S}_j)^2$

2) three ion interactions $(\vec{S}_i \cdot \vec{S}_j)(\vec{S}_j \cdot \vec{S}_k)$

3) four ion interactions $(\vec{S}_i \cdot \vec{S}_j)(\vec{S}_k \cdot \vec{S}_\ell)$

We may examine these various cases through the use of interaction diagrams. In the first case we find:

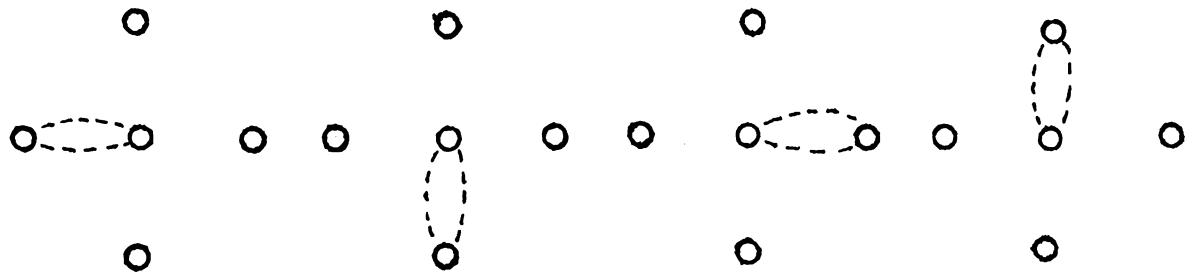

Thus there are 4N terms of the form $(\vec{S}_i \cdot \vec{S}_j)^2$. In the second case:

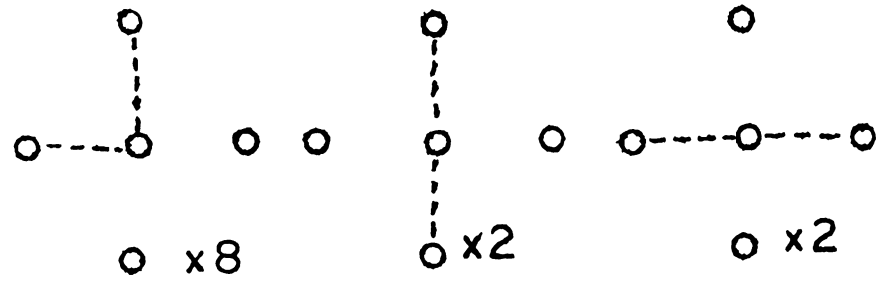

we find 12N terms of the form $(\vec{S}_i \cdot \vec{S}_j)(\vec{S}_j \cdot \vec{S}_k)$. Since there are 4N nearest neighbor pairs in the crystal, the quadratic term in the expansion must contain $(4N)^2$ or a total of $16N^2$ terms in the sum:

$$(\sum_{ij} \vec{S}_i \cdot \vec{S}_j)^2$$

This means the four ion interactions must produce:

$$\begin{aligned} & 16N^2 - 4N - 12N \\ = \; & 16N^2 - 16N \\ = \; & 16N(N-1) \end{aligned}$$

terms of the form:

$$(\vec{S}_i \cdot \vec{S}_j)(\vec{S}_k \cdot \vec{S}_\ell)$$

Thus the quadratic term in the expansion for the partition function is:

$$\frac{1}{2!}\left(\frac{2J}{kT}\right)^2 \left(4N \; \mathrm{tr}(\vec{S}_i \cdot \vec{S}_j)^2 + 12N \; \mathrm{tr}(\vec{S}_i \cdot \vec{S}_j)(\vec{S}_i \cdot \vec{S}_k)\right.$$

$$\left. + (16N(N-1)) \; \mathrm{tr}(\vec{S}_i \cdot \vec{S}_j)(\vec{S}_k \cdot \vec{S}_\ell)\right)$$

We have, at least for these first few terms, reduced the problem to evaluating the traces of pair interactions. However, the counting problem and the associated interaction diagrams become very complex for higher order terms. The counting is usually done by simulating the lattice by a mathematical algorithm on a computer.

APPENDIX B

THE TWO SUBLATTICE CANTED ANTIFERROMAGNET

We assume a Hamiltonian of the following forms:

$$H = -\vec{D}\cdot\vec{S}_1 x \vec{S}_2 - J\,\vec{S}_1\cdot\vec{S}_2 - k(S_{1z}^2+S_{2z}^2)$$

$$\phi_1 = a|1\rangle + b|4\rangle = a\uparrow_2^1 + b\,{}^{\rightarrow 1}_{\rightarrow 2} = \left\langle {}^{1}_{2}\right.$$

$$E_{\phi_1} = -D(ab+ba) + J(a^2-b^2) - k(2a^2)$$

$$= -2Dab + J(a^2-b^2) - 2ka^2$$

recalling the normalization:

$$a^2+b^2 = 1$$

$$E_{\phi_1} = 2Db(1-b^2)^{1/2} + J(1-2b^2) - 2k(1-b^2)$$

$$\frac{\partial E_{\phi_1}}{\partial b} = 0 = -2D(1-b^2)^{1/2} - Db(1-b^2)^{-1/2}(-2b) - 4Jb+4kb$$

$$= -2D(1-b^2)^{1/2} + 2Db^2(1-b^2)^{-1/2} - 4b(J-k)$$

$$= -2D(b^2(1-b^2)^{-1/2} - (1-b^2)^{1/2}) - 2b(J-k)$$

$$= D\,\frac{b^2 - 1+b^2}{(1-b^2)^{1/2}} - 2b(J-k)$$

$$\frac{k-J}{D} = \frac{(1-2b^2)}{2b(1-b^2)^{1/2}}$$

$$2b(1-b^2)^{1/2}\left(\frac{k-J}{D}\right) = (1-2b^2)$$

Square both sides:

$$4b^2(1-b^2)\left(\frac{k-J}{D}\right)^2 = (1-2b^2)^2$$

$$4(b^2-b^4)\left(\frac{k-J}{D}\right)^2 = 1 + 4b^4-4b^2$$

$$4\left[1 + \left(\frac{k-J}{D}\right)^2\right] b^4 - \left[1 + \left(\frac{k-J}{D}\right)^2\right] 4b^2 + 1 = 0$$

let $y = b^2$

$$4\left[1 + \left(\frac{k-J}{D}\right)^2\right] y^2 - 4\left[1 + \left(\frac{k-J}{D}\right)^2\right] y + 1 = 0$$

$$y = \frac{1 + \left(\frac{k-J}{D}\right)^2 \pm \sqrt{\left(1+\left(\frac{k-J}{D}\right)^2\right) - \left(1+\left(\frac{k-J}{D}\right)^2\right)}}{2\left[1+\left(\frac{k-J}{D}\right)^2\right]}$$

$$b = \pm \sqrt{y}$$

Now in the limit D goes to zero, the system must reduce to the uniaxial case which means b must be zero.

$$\lim_{D\to 0} \frac{k-J}{D} = \infty$$

$$\lim_{D\to 0} y \approx \frac{\left(\frac{k-J}{D}\right)^2 \pm \sqrt{\left(\frac{k-J}{D}\right)^4 - \left(\frac{k-J}{D}\right)^2}}{2\left(\frac{k-J}{D}\right)^2}$$

$$\approx \frac{1}{2}(1 \pm 1)$$

Therefore only the - root is correct! Then:

$$b = \pm \left(\frac{(1 + (\frac{k-J}{D})^2) - \sqrt{(1 + (\frac{k-J}{D})^2)^2 - (1 + (\frac{k-J}{D})^2)}}{2(1 + \frac{k-J}{D})^2} \right)^{1/2}$$

$$a = (1 - b^2)^{1/2}$$

The two roots for b correspond to canting along + or -x directions.